



describes a set of studies undertaken to determine the statistical properties of the cosmic microwave background (CMB).

The standard cosmological model is well described by the *Friedmann-Lemaître-Robertson-Walker* (FLRW) solution of the Einstein field equations. This model is characterized by a homogeneous and isotropic metric and an expanding scale factor of the Universe. At very early times it is hypothesized that the universe went through a period of accelerated expansion, the so-called *cosmological inflation*, driven by a hypothetical scalar field, the *inflaton*. During inflation the universe behaves as a de Sitter space, providing the conditions in which some of the present properties of the universe can be realized and specifically relaxing the problem of initial conditions. In particular, the seeds that gave rise to the present large-scale matter distribution via gravitational instability originated as quantum fluctuations of the inflaton about its vacuum state. These fluctuations in the inflaton produce energy perturbations which are distributed as a homogeneous and isotropic Gaussian random field. Linear theory relates those energy fluctuations to the CMB anisotropies, implying a distribution for the anisotropies very close to that of an isotropic Gaussian random field.

The scope of this work is to use *Planck* data to test the Gaussianity and near isotropy of the CMB in intensity as expected in the standard cosmology paradigm. Testing these fundamental properties is crucial for the validation of the standard cosmological scenario, and has profound implications for our understanding of the physical nature of the Universe and the initial conditions of structure formation. Moreover, the confirmation of the isotropic and Gaussian nature of the CMB is essential to justify the corresponding assumptions usually made in the estimation of the CMB power spectra, and other quantities to be obtained from the *Planck* data. Conversely, the detection of significant deviations from these assumptions that are not consistent with known systematic effects or foreground residuals would necessitate major revision of current methodological approaches for the derivation of the mission's many science results.

Significant deviations from Gaussianity are expected from non-linear processes that lead to secondary anisotropies, e.g. the integrated Sachs-Wolfe (ISW) effect and lensing. Indeed, these effects are the subject of two companion *Planck* papers (Planck Collaboration XVII 2013; Planck Collaboration XIX 2013, respectively). However, remarkably, a number of anomalies, by which we mean features of the observed sky that are not statistically consistent with the best-fit  $\Lambda$ CDM model, have been found in the *WMAP* data. Indeed, the *WMAP* team (Spergel et al. 2003) themselves initially proposed some intriguing discrepancies in the form of a lack of power on large angular scales. Further examples include an alignment of the low order multipoles some of which also indicate anomalously low amplitudes (Tegmark et al. 2003; Bielewicz et al. 2005; Land & Magueijo 2005a), a North-South asymmetry in both power spectra (Eriksen et al. 2004a; Hansen et al. 2009) and various measures of non-Gaussianity (Eriksen et al. 2004c, 2005; Räth et al. 2007a), parity asymmetry in the power spectrum corresponding to large angular scales (Kim & Naselsky 2010a) and a region of significant temperature decrement — the so-called *Cold Spot* (Vielva et al. 2004; Cruz et al. 2005).

Whilst *WMAP* have presented refutations of these anomalies, either by criticism of the robustness of the statistical meth-

ods employed (Bennett et al. 2011) or by associating them with systematic artefacts of the data processing that have been corrected in the nine-year data release (Bennett et al. 2012), *Planck* represents a unique opportunity to independently assess their existence. Its higher angular resolution and sensitivity and wider frequency range will allow a better understanding and removal of the Galactic and extragalactic foregrounds thus allowing a larger fraction of the sky to be useful for performing isotropy and Gaussianity analysis and to confirm and interpret those anomalies.

Throughout this paper, we quantify the significance of the test statistic in terms of the p-value. This is the probability of obtaining a test statistic at least as extreme as the observed one, under the assumption that the null hypothesis (i.e., Gaussianity and isotropy of the CMB) is true. In some tests, where it is well motivated to use only a one-tailed probability, the p-value is replaced by the corresponding upper or lower-tail probability. A low p-value is indicative of a tension between the data and the assumed statistical model (the null hypothesis). This can arise either when the assumed cosmological model is incorrect, if unknown or unmodelled aspects of the foreground emission or the measurement process exist, or as a result of a natural statistical fluctuation. The most interesting possibility, of course, is that a low p-value is an indication of new physics.

From the theoretical point of view, there are many variants of inflation that predict high levels of non-Gaussianity and new scenarios motivated by string and M-theory. In addition, there are many physical effects that might give rise to a deviation from isotropy or the presence of non-Gaussianity. Those deviations may be classified according to their physical nature and origin as follows: non-standard inflationary models, geometry and topology of the Universe, and topological defects. The main results from these areas, as well as the detailed descriptions of methodologies and of specific theoretically-motivated model constraints, are provided in the companion papers Planck Collaboration XXIV (2013), Planck Collaboration XXVI (2013), and Planck Collaboration XXV (2013).

This paper covers all relevant aspects related to the phenomenological study of the statistical isotropy and Gaussian nature of the CMB measured by the *Planck* satellite. It is organized as follows. Section 2 describes the *Planck* data used for the analyses. Section 3 explains the main characteristics of the simulations that constitute our reference set of Gaussian sky maps representative of the null hypothesis. In Sect. 4 the null hypothesis is tested with a number of standard tests that probe different aspects of non-Gaussianity. The *WMAP* anomalies are revisited in the light of the *Planck* data in Sect. 5. In Sect. 6 the implications of the found deviations of the null hypothesis on  $C_\ell$  and cosmological parameters estimations are discussed. Finally, Sect. 7 provides the main conclusions of the paper.

## 2. Data description

In this paper, we utilise data from the *Planck*-2013 data release corresponding to the nominal period of the *Planck* mission. In part, this comprises sky maps at nine frequencies, with corresponding ‘half-ring’ maps that are generated by separating the data for a given pointing period into two halves, plus maps generated from data within the first and second survey periods. This set of maps allow a variety of consistency checks to be made, together with estimates of the instrumental noise contributions to analyses and limits on time-varying systematic artefacts. Full details are provided in papers Planck Collaboration II (2013); Planck Collaboration VI (2013).

---

entific consortia funded by ESA member states (in particular the lead countries France and Italy), with contributions from NASA, (USA) and telescope reflectors provided by a collaboration between ESA and a scientific consortium led and funded by Denmark

Our main results are based on the CMB maps resulting from sophisticated component separation algorithms applied to the frequency maps, as detailed in Planck Collaboration XII (2013). The four methods — Commander-Ruler, NILC, SEVEM and SMICA — are used to generate estimates of the CMB sky with an effective angular resolution of around  $7'$  or better, with accompanying symmetrised beam profiles, analysis masks, half-ring and survey maps. In general, the analyses presented here make use of a standardised common mask that merges those associated with the individual methods (this mask is listed in Table 1 as U73). This is a conservative approach and therefore, where appropriate, we manipulate the masks for use at lower resolution. Low resolution maps are required in some analyses and have been produced as follows. For resolutions  $N_{\text{side}}=128$ – $1024$  the full resolution maps have been degraded using the `ud_degrade HEALPix` (Górski et al. 2005) routine. For degrading to even lower resolutions,  $N_{\text{side}}=16$ – $64$ , a different procedure has been followed. Before degrading the maps to the final resolution using the `ud_degrade` routine as in the previous case, the full-resolution map is smoothed with a Gaussian kernel with a FWHM equal to three times the pixel size of the low resolution map that we want to produce.

In Table 1 we list the different masks that have been used in the analyses described in this paper. These masks have been produced at full resolution ( $N_{\text{side}}=2048$ ) and are described in papers Planck Collaboration XII (2013); Planck Collaboration XV (2013). The mask U73 is the most often used in this paper. However, for several applications the masks have been degraded to lower resolutions ( $N_{\text{side}}=1024, 512, 256, 128, 64, 32$  and  $16$ ). The masks with resolutions  $N_{\text{side}}=128$ – $1024$  have been degraded using the following procedure: first, the masks are degraded to their final resolution using the `ud_degrade HEALPix` routine, and then, a conservative approach is followed setting to zero any pixels with a value lower than 0.8. If the masks have to be degraded to even lower resolutions,  $N_{\text{side}}=16$ – $64$ , the procedure that has been used is different. First, the full-resolution mask is smoothed with a Gaussian kernel with a FWHM equal to three times the pixel size of the low resolution mask that we want to produce. Then the mask is degraded using `ud_degrade` to their final resolution. Finally, those pixels with a value lower or equal than 0.5 have been set to zero and the rest have been set to 1. This criterion, less conservative than the one used for the higher resolution masks, is a compromise between minimizing the amount of sky that is being masked and the level of contamination left unmasked (we remark that in some cases the more conservative criterion of a 0.8 threshold has been also used for the lower resolutions, as stated in the corresponding analyses).

### 3. Simulations

The derivation of results to be presented in this paper requires extensive simulations, essential aspects of which include: 1) modeling the *Planck* instrumental effects that affect the quality of the data, including instrumental noise and identified systematic effects, 2) replicating the foreground removal approach and estimating the extent of foreground residuals, and 3) modeling the intrinsic statistical properties, Gaussian or otherwise, of the CMB signals expected from specific models of the Universe.

The full focal plane (FFP6) simulations described in Planck Collaboration ES (2013) provide a complete realisation of the *Planck* mission capturing all characteristics of the scanning strategy, telescope, detector responses, and data reduction pipeline over the nominal mission period of 15.5 months. The Planck Sky Model (PSM) is used as input, encompassing the best current es-

**Table 1.** List of the masks that have been used for the analyses described in this paper. All of them have been generated at  $N_{\text{side}} = 2048$ , and when needed, they have been degraded to a lower resolution as explained in the text. The CL masks have been constructed following the procedure described in Planck Collaboration XV (2013) but for different sky coverages.

Mask name	Sky coverage [% of unmasked pixels]
CS-SMICA89 <sup>1</sup> ..	89.0
U73 <sup>1</sup> .....	73.0
CG90 <sup>1</sup> .....	90.0
CG80 <sup>1</sup> .....	80.0
CG70 <sup>1</sup> .....	70.0
CG60 <sup>1</sup> .....	60.0
CL65 <sup>2</sup> .....	65.1
CL58 <sup>2</sup> .....	57.8
CL48 <sup>2</sup> .....	48.0
CL37 <sup>2</sup> .....	37.3
CL25 <sup>2</sup> .....	24.7

<sup>1</sup> Planck Collaboration XII (2013)

<sup>2</sup> Planck Collaboration XV (2013)

timate of the microwave sky at *Planck* wavelengths including Galactic and extragalactic astrophysical foreground emission. The outputs include a complete set of maps for all detectors with accompanying half-ring and survey splits generated for a reference CMB sky. These have been used to test and validate various analysis tools, employed in turn to evaluate the CMB component separation algorithms as applied to the data set. This also allows an FFP6-based estimate of the foreground residuals remaining in the CMB sky after component separation to be evaluated, and their impact on various statistical estimators quantified.

An accompanying set of Monte Carlo simulations provides us with the reference set of Gaussian sky maps used for the null tests we employ. These simulations include FEBeCoP (Mitra et al. 2011) beam convolution at each of the *Planck* frequencies, which are then propagated through the various component separation pipelines using the same weights as derived from the *Planck* nominal mission data analysis. A fiducial CMB power spectrum has been adopted based on an analysis of the *Planck* data at an advanced, but not final stage of processing. Only small changes relative to the final *Planck* power spectrum presented in Planck Collaboration XV (2013); Planck Collaboration XVI (2013) are observed.

### 4. Are the primordial fluctuations Gaussian?

As has been previously established, it is of major interest to determine whether the statistical properties of the primordial CMB anisotropies correspond to an isotropic Gaussian random field. Recent attempts to test this hypothesis have mainly relied on the *WMAP* data that have less sensitivity and cover a narrower frequency interval. *Planck* represents a unique opportunity to probe fundamental statistical properties of the Universe with cosmic variance limited sensitivity up to  $\ell \approx 2000$  and minimum foreground contamination.

There is no unique signature of non-Gaussianity, however, different tests can allow us to probe different types of non-Gaussianity. As a consequence, it is important to subject the data to a variety of tests, and we do so in this section using a number of non-parametric tools. Specific signatures of non-Gaussianity are sought in three companion papers — Planck

Collaboration XXIV (2013); Planck Collaboration XXV (2013); Planck Collaboration XXVI (2013).

Any isotropic and continuous random field,  $T(\mathbf{x})$  on the sphere can be written in terms of the following spectral representation:

$$T(\mathbf{x}) = \sum_{\ell=0}^{\infty} \sum_{m=-\ell}^{\ell} a_{\ell m} Y_{\ell m}(\mathbf{x}), \quad (1)$$

where  $\mathbf{x}$  is a unit direction vector,  $Y_{\ell m}(\cdot)$  the spherical harmonics and

$$a_{\ell m} = \int d\mathbf{x} T(\mathbf{x}) Y_{\ell m}^*(\mathbf{x}), \quad (2)$$

$m = 0, \pm 1, \dots, \pm \ell$ ,  $\ell = 1, 2, \dots$

For a Gaussian field with uncorrelated phases, each  $a_{\ell m}$  coefficient will be independent with a zero mean Gaussian distribution:

$$\langle a_{\ell m} a_{\ell' m'}^* \rangle = \delta_{\ell \ell'} \delta_{m m'}^m C_{\ell} \quad (3)$$

where  $\delta$  is the Kronecker delta and  $C_{\ell}$  is the angular power spectrum. Note that for a Gaussian and isotropic random field, the angular power spectrum provides a complete characterization of its statistical distribution.

In this paper, we examine the goodness-of-fit of the data to the *Planck* best-fit fiducial CMB model, which constitutes our null hypothesis. The methods adopted constitute a broad range of statistical tools that allow the study of complementary statistical properties of the null hypothesis in both the real and harmonic space data representations. Claims of either consistency with the fiducial *Planck* cosmological model or of evidence for non-Gaussianity must be demonstrably robust to data selection and specifics of the data analysis. Residuals from the diffuse Galactic foreground are likely to be non-Gaussian in nature, and point-sources can be a source of non-Gaussianity on small angular scales. In addition, the analysis of multifrequency data must be considered in order to confirm that any claimed non-Gaussianity has a thermal (cosmological) spectrum. Moreover, the combined ISW-lensing effect produces secondary anisotropies that significantly deviate from Gaussianity and whose effect has been detected in the *Planck* data (Planck Collaboration XIX 2013). This non-Gaussian effect has to be considered when testing the null hypothesis.

We address these issues by analysing the cosmologically interesting subset of *Planck* frequency channels. Specifically, we analyse the uncorrected sky maps at 70, 100, 143 and 217 GHz as a function of Galactic mask to assess the likely contamination due to Galactic foregrounds. These tests have direct relevance for the *Planck* likelihood approach described in Planck Collaboration XV (2013) and the parameter estimation results presented in Planck Collaboration XVI (2013). We then consider the foreground cleaned versions of these maps generated by the SEVEM algorithm (see Planck Collaboration XII 2013). Such a comparison also allows a semi-independent cross-check of the cosmological signal seen by *Planck* LFI (70 GHz) and HFI (100, 143, 217 GHz). Although the cosmological content of the cleaned LFI and HFI data sets are independent, the cleaning makes use of difference maps generated from the remaining *Planck* frequency bands. Nevertheless, since the calibration and beam responses of the data are well understood over the full range of frequencies, there will be no leakage of cosmological signal between the instrument specific frequencies.

We then continue with analyses of the CMB sky estimates provided by four component separation approaches

**Table 2.** Lower tail probability for the variance, skewness and kurtosis estimators at  $N_{\text{side}} = 2048$ , using the U73 mask and four different component separation methods.

Method	Variance	Skewness	Kurtosis
C-R . . . . .	0.021	0.189	0.416
NILC . . . . .	0.020	0.191	0.392
SEVEM . . . . .	0.014	0.206	0.419
SMICA . . . . .	0.017	0.189	0.419

(Commander-Ruler, NILC, SEVEM, and SMICA) described in Planck Collaboration XII (2013), together with the corresponding mask appropriate for these methods. The largest sky area possible should be used for definitive statements about Gaussianity since, in the absence of foreground residuals or systematic artefacts, it represents a superior sample of the Universe. Conversely, overly conservative sky cuts suffer from a loss of information.

#### 4.1. One dimensional moments

In this section we perform some of the simplest Gaussianity tests, such as comparing the sample skewness and kurtosis of the data with simulations. The skewness,  $\gamma$ , and kurtosis,  $\kappa$ , of a random variable,  $X$ , are defined as follows:

$$\gamma(X) = \frac{\langle X - \langle X \rangle \rangle^3}{(\text{Var}(X))^{3/2}} \quad (4)$$

$$\kappa(X) = \frac{\langle X - \langle X \rangle \rangle^4}{(\text{Var}(X))^2} - 3 \quad (5)$$

The skewness is a measure of the asymmetry of the probability distribution of a real-valued random variable. Qualitatively, a positive (negative) skew indicates that the tail on the right (left) side of the probability density function is longer than the left (right) side. A zero value indicates that the values are relatively evenly distributed on both sides of the mean, typically but not necessarily implying a symmetric distribution. The kurtosis is a measure of the peakedness of the distribution and the heaviness of its tail. A distribution with positive (negative) excess kurtosis indicates that the distribution has a more acute (wider) peak around the mean and fatter (thinner) tails. Normal random variables have zero skewness and kurtosis.

The sample variance is also considered in this section as a further consistency test, although it is not a normality test statistic.

We begin by analysing the full resolution combined maps, applying the U73 mask for the four different component separation methods. The results for the variance, skewness and kurtosis estimators are shown in Table 2. All four methods show similar results. The data are consistent with simulations for the skewness and kurtosis estimators, whereas the variance is anomalously low. This inconsistency was already reported for the *WMAP* data in Monteserín et al. (2008) and Cruz et al. (2011) at resolution  $N_{\text{side}} = 256$  for a mask allowing slightly less sky coverage.

The mask dependence of our results is studied by recalculating the estimators using the CL58 and CL37 masks which allow sky fractions of  $f_{\text{sky}} = 58\%$  and  $f_{\text{sky}} = 37\%$  respectively. The SMICA cleaned maps at full resolution are considered. The most significant lower tail probability is obtained for the CL58 mask as can be seen in Table 3. The lower tail probabilities show a small dependence on the mask used, which could indicate either the presence of Galactic foreground residuals with larger



**Table 3.** Lower tail probability for the variance, skewness and kurtosis estimators at  $N_{\text{side}} = 2048$ , for the SMICA method, using different masks.

Mask	Variance	Skewness	Kurtosis
U73, $f_{\text{sky}} = 73\%$ . . . . .	0.017	0.189	0.419
CL58, $f_{\text{sky}} = 58\%$ . . . . .	0.003	0.170	0.363
CL37, $f_{\text{sky}} = 37\%$ . . . . .	0.030	0.314	0.266
Ecliptic North, $f_{\text{sky}} = 36\%$ . . . .	0.001	0.553	0.413
Ecliptic South, $f_{\text{sky}} = 37\%$ . . . .	0.483	0.077	0.556
Galactic North, $f_{\text{sky}} = 37\%$ . . . .	0.001	0.788	0.177
Galactic South, $f_{\text{sky}} = 36\%$ . . . .	0.592	0.145	0.428

**Table 4.** Lower tail probability for the variance, skewness and kurtosis estimators at  $N_{\text{side}} = 2048$ , for the SEVEM cleaned maps at different frequencies.

Map	Variance	Skewness	Kurtosis
100 GHz . . . . .	0.023	0.195	0.488
143 GHz . . . . .	0.014	0.221	0.460
217 GHz . . . . .	0.025	0.196	0.481

sky coverage, or the increase of the sampling variance, and consequently a less significant probability, when a smaller fraction of the sky is considered.

In order to identify any foreground contamination, the frequency dependence of our estimators is analysed. We use the SEVEM cleaned maps and the U73 mask. Note that as the 70 GHz full resolution noise is high we do not consider 70 GHz in this comparison. As the 100 GHz noise is not negligible we estimate the variance taking into account the noise dispersion as described in Cruz et al. (2011). The results are similar to those found for the combined map, as can be seen in Table 4. There is a small frequency dependence since the 100 GHz and 217 GHz maps show slightly higher variance and kurtosis than the 143 GHz map. However the 143 GHz map has a dominant contribution to the combined map, hence the foreground residuals in the combined map are likely to be small. The lower tail probabilities for the variance at 100 GHz, 143 GHz, and 217 GHz are respectively 0.021, 0.014, 0.025, whereas the skewness and kurtosis are compatible with simulations.

We also reanalyse the SMICA data and simulations considering independently the northern and southern ecliptic hemispheres outside the U73 mask. A clear asymmetry is found in the variance, with an anomalously low value found in the northern hemisphere, as seen in Table 3.

The results for different resolutions using the U73 mask are shown in Table 5. Note that the  $N_{\text{side}} = 2048$  and 512 U73 masks have  $f_{\text{sky}} = 73\%$ , while the low resolution masks at  $N_{\text{side}} = 64$ , 32, and 16 have  $f_{\text{sky}} = 78\%$ . The variance is anomalously low at all the considered resolutions, whereas at low resolutions, the skewness is anomalously low and the kurtosis anomalously high. These results will be further analysed in Sect. 5.2. However, it is clear that, except on the largest angular scales, there is no evidence for non-Gaussian behaviour in the data using these simple statistical measures.

**Table 5.** Lower tail probability for the variance, skewness and kurtosis estimators at different resolutions, for the four component separation methods, using the U73 mask.

Method	Variance	Skewness	Kurtosis
$N_{\text{side}} = 2048$			
C-R . . . . .	0.021	0.189	0.416
NILC . . . . .	0.020	0.191	0.392
SEVEM . . . . .	0.014	0.206	0.419
SMICA . . . . .	0.017	0.189	0.419
$N_{\text{side}} = 512$			
C-R . . . . .	0.017	0.207	0.368
NILC . . . . .	0.017	0.198	0.390
SEVEM . . . . .	0.013	0.218	0.408
SMICA . . . . .	0.014	0.196	0.390
$N_{\text{side}} = 64$			
C-R . . . . .	0.011	0.041	0.935
NILC . . . . .	0.011	0.041	0.935
SEVEM . . . . .	0.008	0.058	0.900
SMICA . . . . .	0.011	0.041	0.943
$N_{\text{side}} = 32$			
C-R . . . . .	0.020	0.015	0.968
NILC . . . . .	0.019	0.016	0.960
SEVEM . . . . .	0.012	0.026	0.932
SMICA . . . . .	0.019	0.016	0.967
$N_{\text{side}} = 16$			
C-R . . . . .	0.023	0.013	0.974
NILC . . . . .	0.022	0.022	0.972
SEVEM . . . . .	0.019	0.022	0.964
SMICA . . . . .	0.027	0.021	0.982

#### 4.2. $N$ -pdf analysis

Under the assumption of Gaussianity, the  $N$ -probability density function ( $N$ -pdf) is given by a multivariate Gaussian function:

$$f(\mathbf{T}) = \frac{1}{(2\pi)^{N_{\text{pix}}/2} \det \mathbf{C}^{1/2}} \exp - \frac{1}{2} (\mathbf{T} \mathbf{C}^{-1} \mathbf{T}^T), \quad (6)$$

where  $\mathbf{T}$  is a vector formed from the measured temperatures  $T(\mathbf{x})$  over all positions allowed by the applied mask,  $N_{\text{pix}}$  is the number of pixels in the vector,  $\mathbf{C}$  is the covariance of the Gaussian field (of size  $N_{\text{pix}} \times N_{\text{pix}}$ ).

Unfortunately, the calculation of  $\mathbf{T} \mathbf{C}^{-1} \mathbf{T}^T$  is computationally unfeasible for the full *Planck* resolution at HEALPix  $N_{\text{side}} = 2048$ . At a lower resolution, the problem is tractable, and the noise level can also be considered negligible compared to the CMB signal. That implies that under the assumption of isotropy the covariance matrix  $\mathbf{C}$  is fully defined by the *Planck* angular power spectrum ( $C_\ell$ ):

$$C_{ij} = \sum_{\ell=0}^{\ell_{\text{max}}} \frac{2\ell+1}{4\pi} C_\ell b_\ell^2 P_\ell(\cos \theta_{ij}), \quad (7)$$

where  $C_{ij}$  is the covariance between pixels  $i$  and  $j$ , and  $\theta_{ij}$  is angle between them,  $P_\ell$  are the Legendre polynomials,  $b_\ell$  is an effective window function associated with the  $N_{\text{side}}$  resolution, and  $\ell_{\text{max}}$  is the maximum multipole probed.

Under the multivariate Gaussian hypothesis, the argument on the exponential in equation 6 should follow a  $\chi^2$  distribution with  $N_{\text{pix}}$  degrees of freedom, or, equivalently (for  $N_{\text{pix}} \gg 1$ ) a normal distribution  $\mathcal{N}(N_{\text{pix}}, \sqrt{N_{\text{pix}}})$ .

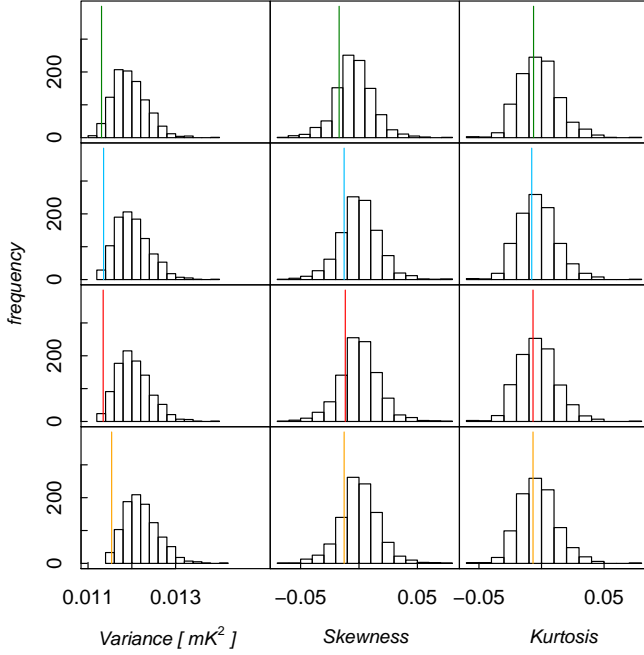


**Fig. 1.** Variance, skewness and kurtosis for the combined map of the four different component separation methods. From top row to bottom row C-R, NILC, SEVEM, SMICA.

**Table 6.** Lower tail probability for the  $N$ -pdf, using different masks.

Mask	C-R	NILC	SEVEM	SMICA
U73, $f_{\text{sky}} = 78\%$	0.027	0.028	0.019	0.030
CL58, $f_{\text{sky}} = 58\%$	0.137	0.137	0.147	0.146
CL37, $f_{\text{sky}} = 37\%$	0.409	0.415	0.420	0.436
Ecliptic North, $f_{\text{sky}} = 39\%$	0.024	0.022	0.021	0.021
Ecliptic South, $f_{\text{sky}} = 39\%$	0.170	0.196	0.183	0.193

We begin by analysing the  $\chi^2$  quantity for low resolution maps at  $N_{\text{side}} = 32$  and filtering with a  $5^\circ$  FWHM Gaussian.  $1 \mu\text{K}$  uncorrelated regularization noise is added to the covariance matrix before inverting it. Regularization noise realizations are added to the data and simulations for consistency (see Eriksen et al. 2007b, for more details).

We analyse the four cleaned data maps, applying the common, CL58 and CL37 masks. The admitted fraction of the sky is respectively 78%, 58% and 37%. The northern and southern ecliptic hemispheres outside the U73 mask are also considered. The results are shown in Fig. 2 and Table 6. In the U73 mask case, the lower tail probabilities are low. Applying the two CL58 and CL37 masks that permit less sky coverage, the data are consistent with simulations. The low  $\chi^2$  value appears to be localised in the northern ecliptic hemisphere. These results are directly comparable to the anomalous variance mentioned in Sect. 4.1. Note that the four maps show similar values, but the differences are larger when using the U73 mask. This could indicate the presence of some residual foreground contamination near the Galactic plane. Therefore, the frequency dependence of our estimator is analysed in order to identify any possible foreground contamination. The results are shown in Fig. 3 and Table 7. A moderate frequency dependence is found when using the U73 mask, which could indicate the presence of some foreground

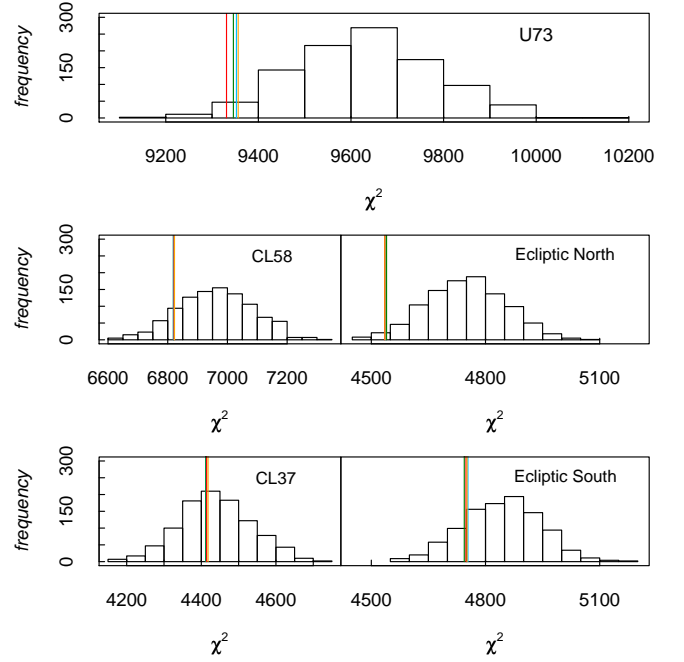


**Fig. 2.**  $N$ -pdf  $\chi^2$  for the U73 mask, CL58, CL37, ecliptic North and ecliptic South. The different colours represent the four component separation methods, namely C-R (green), NILC (blue), SEVEM (red), and SMICA (orange).

**Table 7.** Frequency dependence of the lower tail probability for the  $N$ -pdf, using different masks.

Mask	70 GHz	100 GHz	143 GHz	217 GHz
U73, $f_{\text{sky}} = 78\%$	0.037	0.058	0.013	0.124
CL58, $f_{\text{sky}} = 58\%$	0.169	0.123	0.111	0.169
CL37, $f_{\text{sky}} = 37\%$	0.422	0.366	0.376	0.386
Ecliptic North, $f_{\text{sky}} = 39\%$	0.028	0.050	0.015	0.083
Ecliptic South, $f_{\text{sky}} = 39\%$	0.225	0.233	0.166	0.330

residuals near the Galactic plane. The frequency dependence of the results vanishes when using the CL58 and CL37 masks that exclude more of the sky from analysis.

#### 4.3. $N$ -point correlation functions

In this section we present tests of the non-Gaussianity of the *Planck* CMB maps using real-space  $N$ -point correlation functions. While harmonic-space methods are often preferred over real-space methods for studying primordial fluctuations, real-space methods may have an advantage with respect to systematics and foregrounds, since such effects are usually localized in real space. It is therefore important to analyse the data in both spaces in order to highlight different features.

An  $N$ -point correlation function is by definition the average product of  $N$  temperatures, measured in a fixed relative orientation on the sky,

$$C_N(\theta_1, \dots, \theta_{2N-3}) = \left\langle \Delta T(\hat{\mathbf{n}}_1) \cdots \Delta T(\hat{\mathbf{n}}_N) \right\rangle, \quad (8)$$

where the unit vectors  $\hat{\mathbf{n}}_1, \dots, \hat{\mathbf{n}}_N$  span an  $N$ -point polygon on the sky. By assuming statistical isotropy, the  $N$ -point functions are only functions of the shape and size of the  $N$ -point poly-

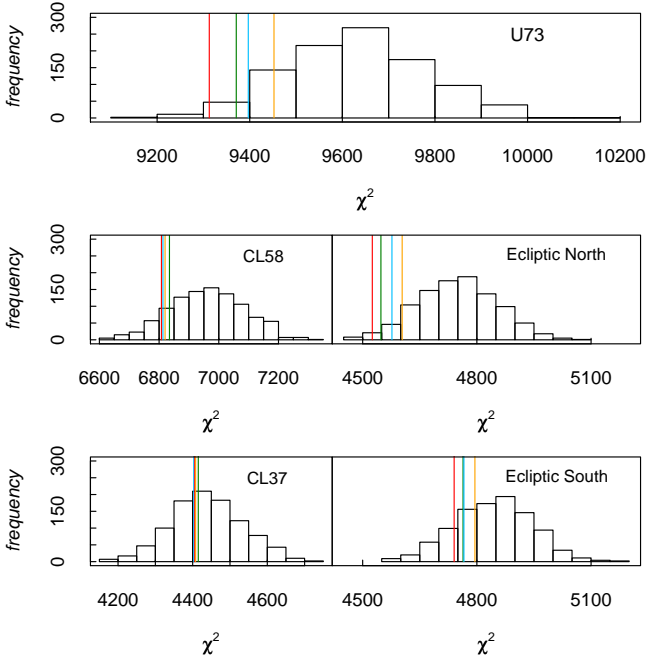


**Fig. 3.** Frequency dependence for 70 GHz (green), 100 GHz (blue), 143 GHz (red) and 217 GHz (orange), and different masks.

gon, and not on its particular position or orientation on the sky. Hence, the smallest number of parameters that uniquely determines the shape and size of the  $N$ -point polygon is  $2N - 3$ . In practice, the functions are estimated by simple product averages over all sets of  $N$  pixels fulfilling the geometric requirements set by  $\theta_1, \dots, \theta_{2N-3}$  characterising the shape and size of the polygon

$$C_N(\theta_1, \dots, \theta_{2N-3}) = \frac{\sum_i (w_1^i \cdots w_N^i) (\Delta T_1^i \cdots \Delta T_N^i)}{\sum_i w_1^i \cdots w_N^i}. \quad (9)$$

Pixel weights  $w_1^i, \dots, w_N^i$  can be introduced in order to reduce noise or mask boundary effects. Here they represent masking by being set to 1 for included pixels and to 0 for excluded pixels.

The main difficulty with computing  $N$ -point functions is their computational scaling. The number of independent pixel combinations scales as  $O(N_{\text{pix}}^N)$ , and for each combination of  $N$  pixels,  $2N - 3$  angular distances must be computed to uniquely determine the properties of the corresponding polygon. Computing the full  $N$ -point function for  $N > 2$  and  $N_{\text{pix}} \gtrsim 10^5$  is therefore computationally challenging. However, it is not necessary to include all possible  $N$ -point configurations in order to produce interesting results. For instance, one may focus only on small angular scales, or on configurations with some special symmetry properties. By using the methods described by Eriksen et al. (2004b), the computational expense then becomes tractable, since no CPU time is spent on excluded configurations. In this paper several such subsets are computed, covering three distinct ranges of scales, namely small (up to  $3^\circ$ ), intermediate (up to  $10^\circ$ ) and large angular scales (the full range between  $0^\circ$  and  $180^\circ$ ). The shapes of considered polygons selected for the analysis are the pseudo-collapsed and equilateral configurations for the 3-point function, and the rhombic configuration composed of two equilateral triangles for the 4-point function. In the following, all results refer to the reduced 4-point function, i.e., corrected for the Gaussian contribution due to the Wick's theorem. The size of the polygons is parametrised by the length of

the longer side of the triangle in the case of the pseudo-collapsed configuration, and the length of the side for the equilateral triangle and rhombus.

We analyse the CMB estimates downgraded to  $N_{\text{side}} = 64$  and  $N_{\text{side}} = 512$  as well as at the original resolution of  $N_{\text{side}} = 2048$ . In the case of the analysis at  $N_{\text{side}} = 64$  the maps were additionally smoothed with FWHM of  $165'$  (three times the pixel size for the downgraded map). Due to computational limitations, an analysis is possible on the full sky only in the case of resolution  $N_{\text{side}} = 64$ . For the higher resolution maps, we perform the analysis on a set of non-overlapping discs. For  $N_{\text{side}} = 512$  we uniformly retain, after masking, part of the sky with approximately 100 discs of radius  $10^\circ$ . Analogously to the analysis by Eriksen et al. (2005), we consider two disc sets A and B with a relative offset between their grids such that the centres of the discs of set B are located in parts of the sky not covered by disc set A (see Fig. 4). For studies at the original resolution  $N_{\text{side}} = 2048$ , we restrict the analysis to 20 discs with a radius of  $3^\circ$  located randomly on an unmasked part of the sky (Fig. 4).

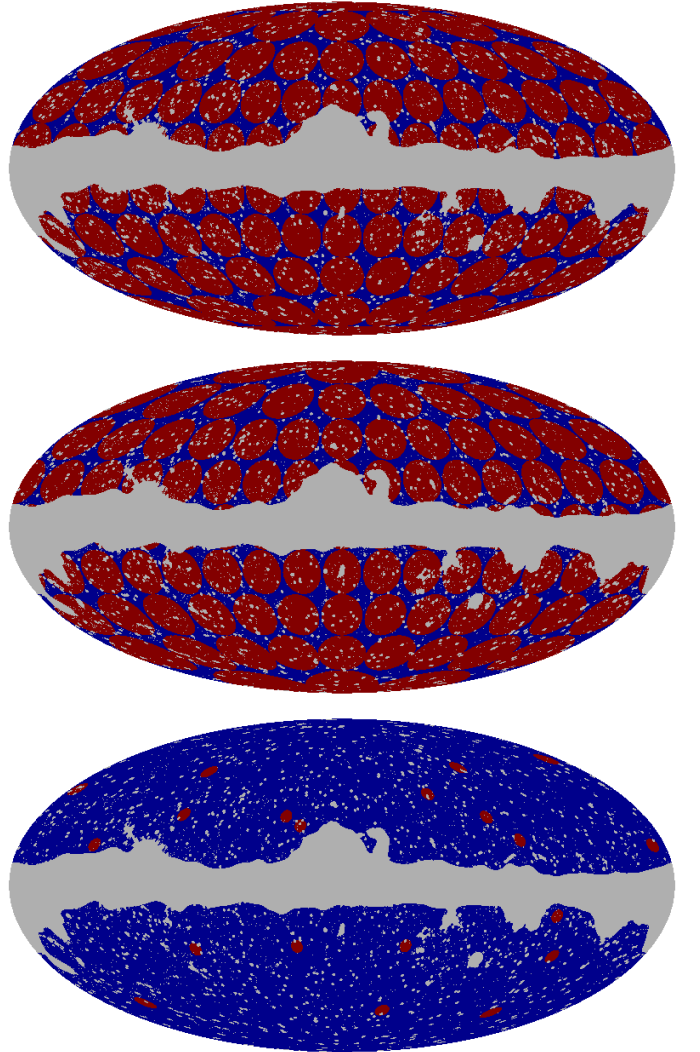


**Fig. 4.** Two sets of discs, A and B, each of radius  $10^\circ$  for the  $N_{\text{side}} = 512$  CMB estimates (upper and middle figure, respectively) and a set of 20 randomly placed discs of radius  $3^\circ$  superimposed on the U73 mask (blue region) for the CMB estimates at  $N_{\text{side}} = 2048$  (lower figure).

As in Eriksen et al. (2005), we consider the  $N$ -point correlation functions averaged over the disc sets. In order to minimize correlations between the discs, we subtract from the maps at resolutions  $N_{\text{side}} = 512$  and  $N_{\text{side}} = 2048$  the best-fit multipoles computed for the ranges  $\ell \leq 18$  and  $\ell \leq 60$ , respectively. This procedure corresponds in practice to a high-pass filtering of the maps.

The low resolution versions of the U73 mask described earlier were used as required. Residual monopole and dipole contributions were then removed from the maps.

A simple  $\chi^2$  test is chosen to quantify the degree of agreement between the simulations and the observations, where  $\chi^2$  as usual is defined by

$$\chi^2 = \sum_{i,j=1}^{N_{\text{bin}}} (C_N(\theta_i) - \langle C_N(\theta_i) \rangle) M_{ij}^{-1} (C_N(\theta_j) - \langle C_N(\theta_j) \rangle). \quad (10)$$

Here  $C_N(\theta_i)$  is the  $N$ -point correlation function for  $i$ -th bin of separation angle,  $\theta_i$ ,  $\langle C_N(\theta_i) \rangle$  is the corresponding average from the Monte Carlo (MC) ensemble, and

$$M_{ij} = \frac{1}{N_{\text{sim}}} \sum_{k=1}^{N_{\text{sim}}} (C_N^{(k)}(\theta_i) - \langle C_N(\theta_i) \rangle) (C_N^{(k)}(\theta_j) - \langle C_N(\theta_j) \rangle) \quad (11)$$

is the covariance matrix. Although the inverse of the covariance matrix constructed from MC simulations can be biased, it is relatively small for 1000 simulations and has a negligible impact on the significance levels estimated from the simulations, as described below.

This statistic is optimized for studying Gaussian distributed data. However, usually it also works quite well for mildly non-Gaussian distributions, and in particular symmetric ones. Nevertheless, as for any statistic constructed from MC simulations, it can also be used for non-Gaussian and asymmetrically distributed data. Below, we quote the significance level in terms of the fraction of simulations with a larger  $\chi^2$  value than the observed map.

We analyse the mask dependence of the non-Gaussianity of the maps using the pseudo-collapsed 3-point correlation function. The function averaged over disc set A is shown in Fig. 5. The corresponding probabilities of obtaining values of the  $\chi^2$  statistic for the concordance  $\Lambda$ CDM model at least as large as the observed values are given in Table 8.

**Table 8.** Probabilities of obtaining values of the  $\chi^2$  statistic for the concordance  $\Lambda$ CDM model at least as large as the observed values of the statistic for the raw 143 GHz (first row) and foreground corrected 143 GHz SEVEM CMB maps (second row).

$f_{\text{sky}}$	0.6	0.7	0.8	0.9
Raw	0.907	0.889	0.563	0.000
SEVEM	0.959	0.959	0.905	0.940

In summary, the pseudo-collapsed 3-point function does not show any significant deviation from Gaussianity for the raw 143 GHz map masked with the CG60 ( $f_{\text{sky}} = 0.6$ ) and CG70 ( $f_{\text{sky}} = 0.7$ ) masks. To a lesser extent, this is true also for the CG80 ( $f_{\text{sky}} = 0.8$ ) mask. We do not see any significant deviation for any of the analysed masks after cleaning the 143 GHz map using the SEVEM method.

The correlation functions for the four component separation methods and resolution parameters  $N_{\text{side}} = 64$ ,  $N_{\text{side}} = 512$  and

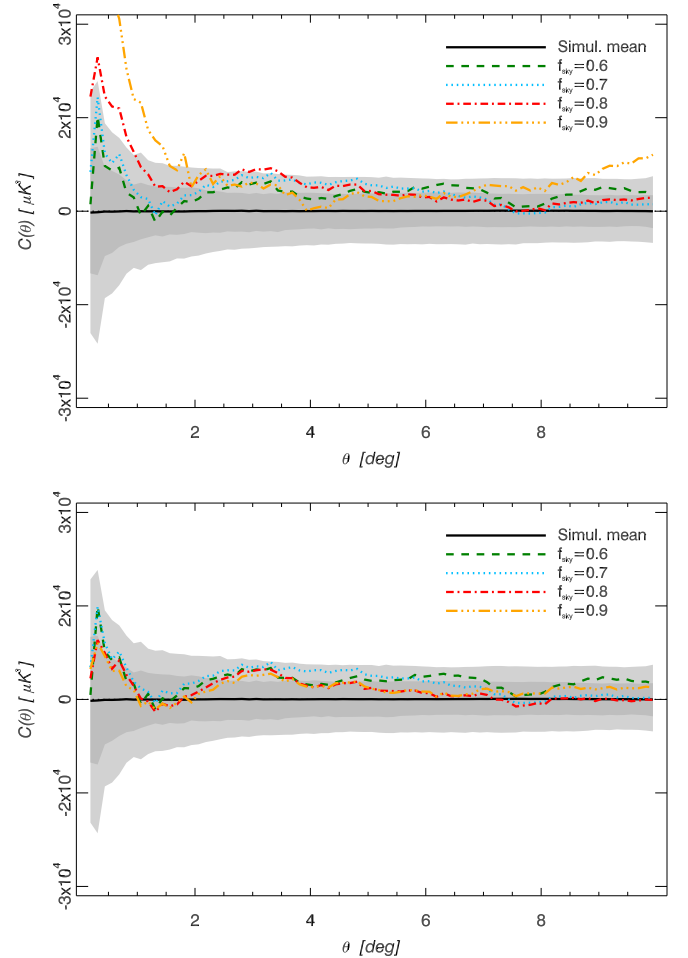


**Fig. 5.** The pseudo-collapsed 3-point function averaged over disc set A for the raw (upper figure) and SEVEM foreground corrected (lower figure) 143 GHz map at  $N_{\text{side}} = 512$ . Estimates of the multipoles for  $\ell \leq 18$  are removed from the sky maps. The black solid line indicates the mean for 1000 MC simulations and the shaded dark and light grey regions indicate the 68% and 95% confidence regions, respectively, for the CG90 ( $f_{\text{sky}} = 0.9$ ) mask.

**Table 9.** Probabilities of obtaining values for the  $\chi^2$  statistic of the  $N$ -point functions shown in Fig. 6 for the *Planck* fiducial  $\Lambda$ CDM model at least as large as the observed values of the statistic for the *Planck* CMB maps with resolution parameter  $N_{\text{side}} = 64$  estimated using the C-R, NILC, SEVEM and SMICA methods.

	C-R	NILC	SEVEM	SMICA
2-pt. ....	0.883	0.859	0.884	0.855
pseudo-coll. 3-pt. ....	0.922	0.918	0.945	0.908
equil. 3-pt. ....	0.962	0.966	0.978	0.968
4-pt. ....	0.975	0.977	0.979	0.977

$N_{\text{side}} = 2048$  are shown in Fig. 6, Fig. 7 (disc set A), Fig. 8 (disc set B) and Fig. 9, respectively. The probabilities of obtaining values of the  $\chi^2$  statistic for the *Planck* fiducial  $\Lambda$ CDM model at least as large as the observed values are given in the Tables 9, 10 and 11, respectively.

The results show consistency between the CMB maps estimated using the different component separation methods. We did not find statistically significant deviations of the CMB maps

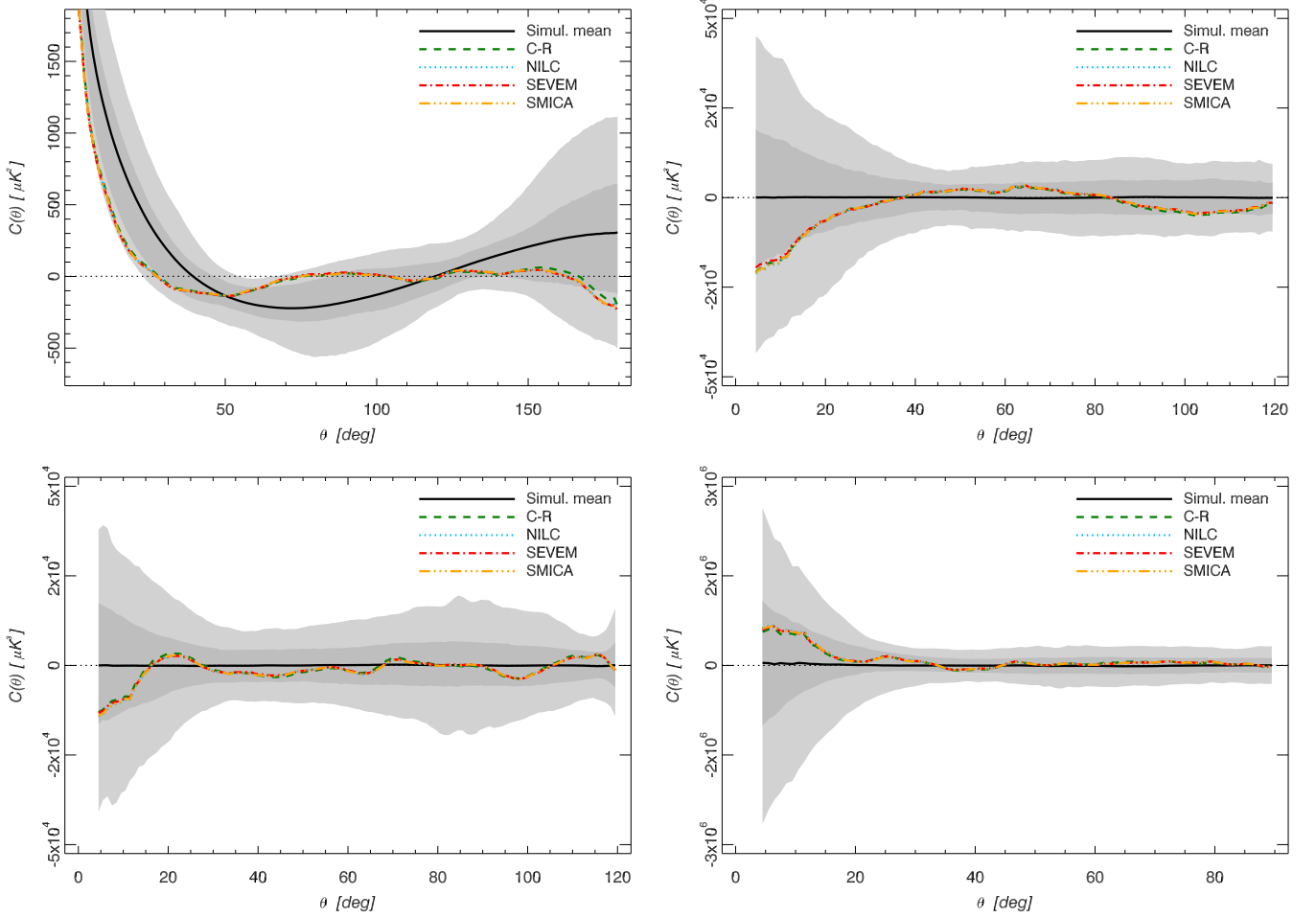


**Fig. 6.** The 2-point (upper left), pseudo-collapsed (upper right), equilateral (lower left) 3-point and reduced rhombic 4-point (lower right) functions for the  $N_{\text{side}} = 64$  CMB estimates. The black solid line indicates the mean for 1000 MC simulations and the shaded dark and light grey regions indicate the 68% and 95% confidence regions, respectively.

**Table 10.** Probabilities of obtaining values of the  $\chi^2$  statistic of the  $N$ -point functions shown in Figs. 7 and 8 for the *Planck* fiducial  $\Lambda$ CDM model at least as large as the observed values of the statistic for *Planck* CMB maps with resolution parameter  $N_{\text{side}} = 512$  estimated using the C-R, NILC, SEVEM and SMICA methods.

	C-R	NILC	SEVEM	SMICA
Two-point function				
A set	0.858	0.902	0.886	0.904
B set	0.351	0.370	0.404	0.376
Pseudo-collapsed three-point function				
A set	0.568	0.565	0.651	0.603
B set	0.483	0.526	0.550	0.540
Equilateral three-point function				
A set	0.004	0.032	0.045	0.043
B set	0.452	0.485	0.443	0.479
Rhombic four-point function				
A set	0.104	0.102	0.102	0.107
B set	0.521	0.569	0.537	0.579

**Table 11.** Probabilities of obtaining values of the  $\chi^2$  statistic of the  $N$ -point functions shown in Fig. 9 for the *Planck* fiducial  $\Lambda$ CDM model at least as large as the observed values of the statistic for *Planck* CMB maps with resolution parameter  $N_{\text{side}} = 2048$  estimated using the C-R, NILC, SEVEM, and SMICA methods.

	C-R	NILC	SEVEM	SMICA
2-pt.	0.335	0.474	0.573	0.497
pseudo-coll. 3-pt.	0.522	0.463	0.469	0.448
equil. 3-pt.	0.853	0.789	0.819	0.796
4-pt.	0.532	0.534	0.579	0.526

from Gaussianity for any of the analysed scales. However, it is clear that the CMB maps smoothed and downgraded to  $N_{\text{side}} = 64$  show the largest deviation, especially for the 4-point correlation function, in comparison to the intermediate and small angular scale analyses.

#### 4.4. Minkowski functionals

Minkowski functionals (Minkowski 1903, hereafter MFs) describe the morphology of fields in any dimension and have long



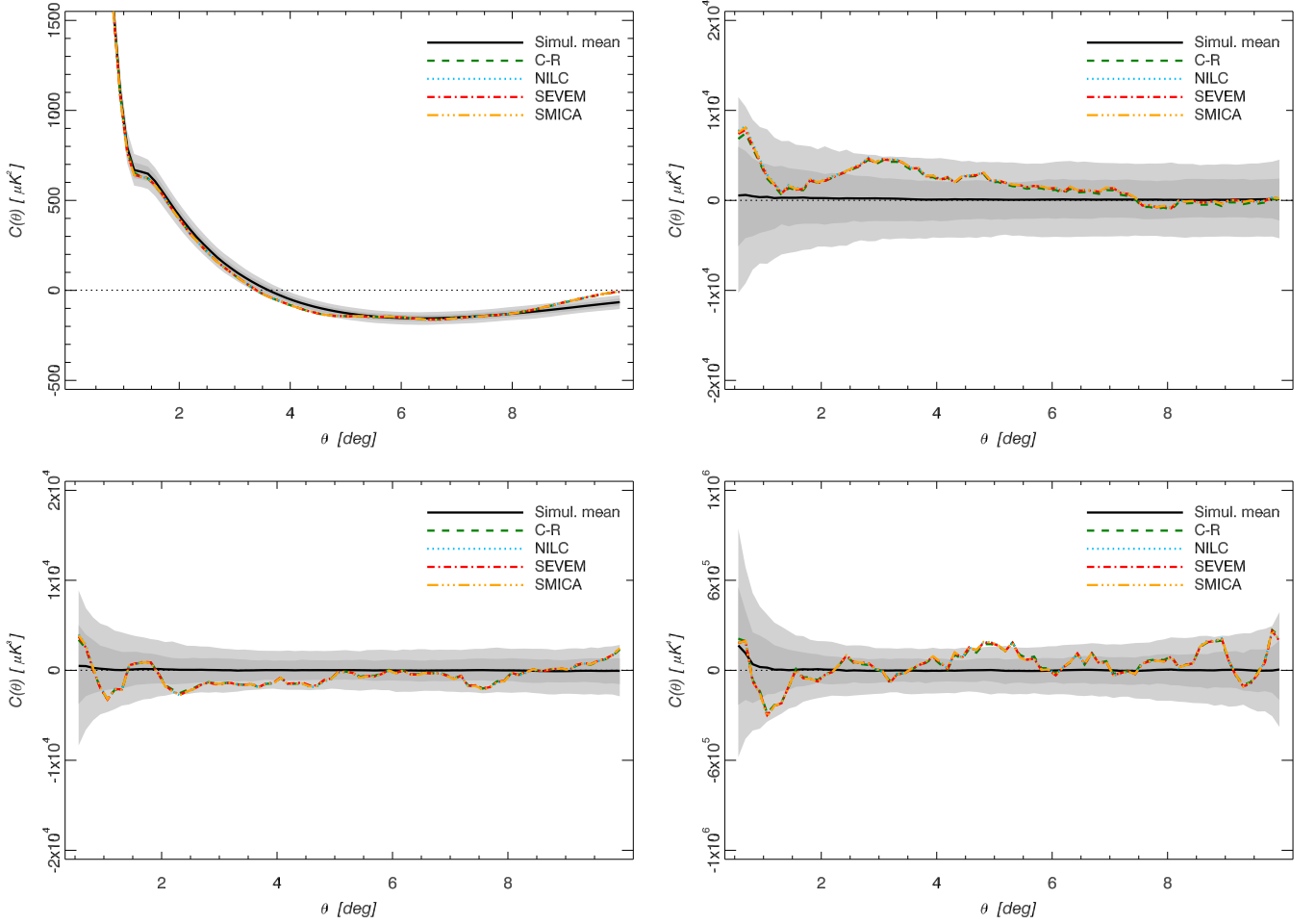


**Fig. 7.** The 2-point (upper left), pseudo-collapsed (upper right), equilateral (lower left) 3-point and reduced rhombic 4-point (lower right) functions averaged over disc set A for the  $N_{\text{side}} = 512$  CMB estimates. Estimates of the multipoles for  $\ell \leq 18$  are removed from the sky maps. The black solid line indicates the mean for 1000 MC simulations and the shaded dark and light grey regions indicate the 68% and 95% confidence regions, respectively.

been used as estimators of non-Gaussianity and anisotropy in the CMB (see e.g., Gott et al. 1990; Mecke et al. 1994; Schmalzing & Gorski 1998; Komatsu et al. 2003; Eriksen et al. 2004c; Curto et al. 2007; De Troia et al. 2007; Spergel et al. 2007; Curto et al. 2008; Hikage et al. 2008; Komatsu et al. 2009). They are additive for disjoint regions of the sky and invariant under rotations and translations. Traditionally in the literature, the contours are defined by a threshold  $\nu$ , usually given in units of the sky standard deviation ( $\sigma_0$ ). We compute MFs for the regions colder and hotter than a given threshold  $\nu$ . Thus, the three MFs, the area  $V_0(\nu) = A(\nu)$ , the perimeter  $V_1(\nu) = C(\nu)$  and the genus  $V_2(\nu) = G(\nu)$ , are defined respectively as:

$$V_0(\nu) = A(\nu) = \frac{N_\nu}{N_{\text{pix}}}, \quad (12)$$

$$V_1(\nu) = C(\nu) = \frac{1}{4A_{\text{tot}}} \sum_i S_i, \quad (13)$$

$$V_2(\nu) = G(\nu) = \frac{1}{2\pi A_{\text{tot}}} (N_{\text{hot}} - N_{\text{cold}}), \quad (14)$$

where  $N_\nu$  is the number of pixels where  $\Delta T/\sigma_0 > \nu$ ,  $N_{\text{pix}}$  is the total number of available pixels,  $A_{\text{tot}}$  is the total area of the

available sky,  $N_{\text{hot}}$  is the number of compact hot spots,  $N_{\text{cold}}$  is the number of compact cold spots and  $S_i$  is the contour length of each hot spot. We construct a fourth functional  $V_3(\nu) = N_{\text{cluster}}(\nu)$  which corresponds to  $N_{\text{cold}}$  for negative  $\nu$  and  $N_{\text{hot}}$  for positive  $\nu$  (Ducout et al. 2012). Analytical expressions for a Gaussian random field can be derived in terms of  $\nu$  (see e.g. Vanmarcke 1983; Matsubara 2010) and give the following,

$$V_k(\nu) = A_k v_k(\nu), \quad (15)$$

with

$$v_k(\nu) = \exp(-\nu^2/2) H_{k-1}(\nu), \quad k \leq 2 \quad (16)$$

$$v_3(\nu) = \frac{e^{-\nu^2}}{\text{erfc}(\nu/\sqrt{2})}, \quad (17)$$

and

$$H_n(\nu) = e^{\nu^2/2} \left( -\frac{d}{d\nu} \right)^n e^{-\nu^2/2}. \quad (18)$$

The amplitude  $A_k$  depends only on the shape of the power spectrum  $C_\ell$ :

$$A_k = \frac{1}{(2\pi)^{(k+1)/2}} \frac{\omega_2}{\omega_{2-k}\omega_k} \left( \frac{\sigma_1}{\sqrt{2}\sigma_0} \right)^k, \quad k \leq 2 \quad (19)$$

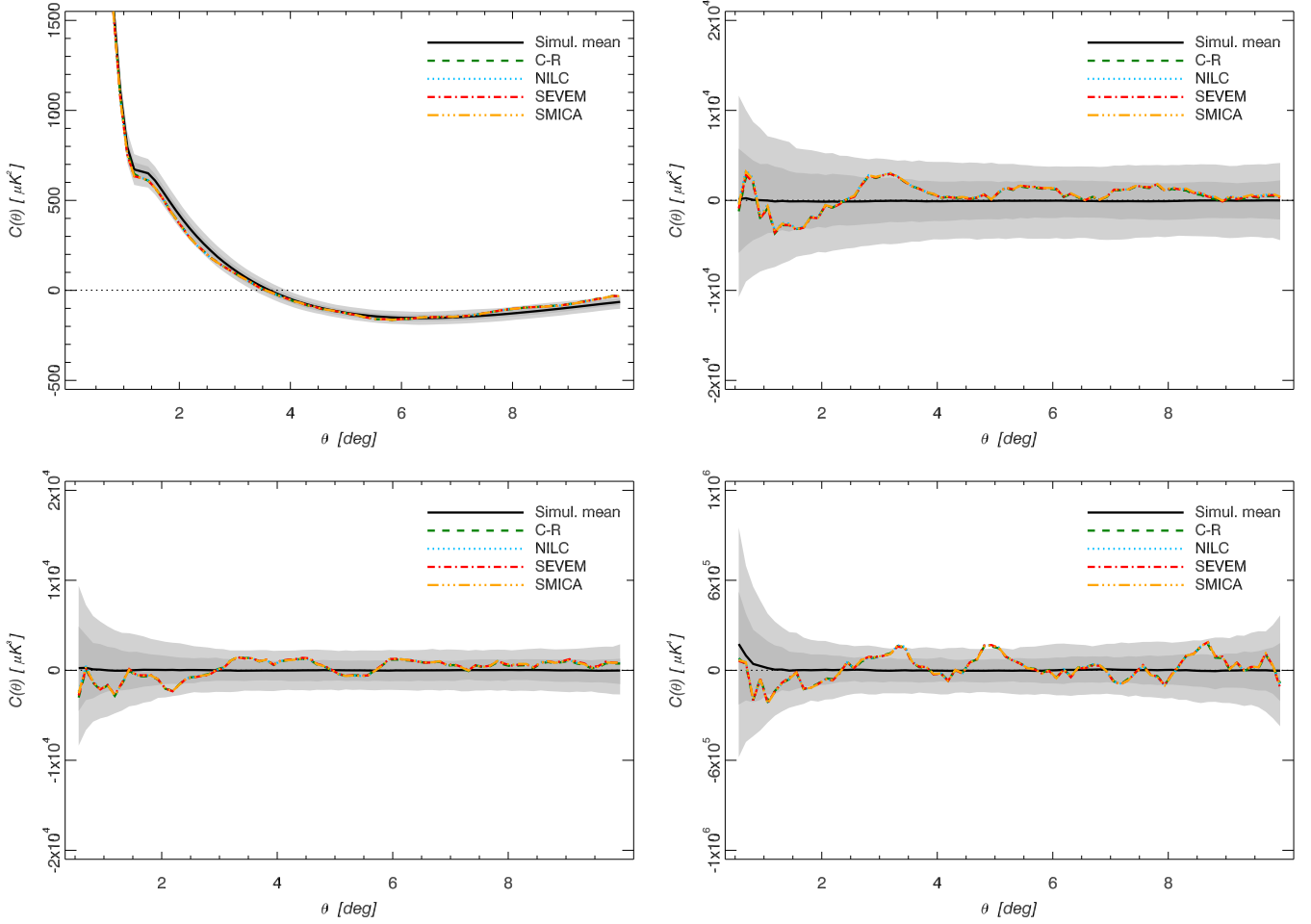


**Fig. 8.** As Fig. 7 for disc set B.

$$A_3 = \frac{2}{\pi} \left( \frac{\sigma_1}{\sqrt{2}\sigma_0} \right)^2 \quad (20)$$

where  $\omega_k \equiv \pi^{k/2}/\Gamma(k/2 + 1)$ , which gives  $\omega_0 = 1$ ,  $\omega_1 = 2$ ,  $\omega_2 = \pi$  and  $\sigma_0$  and  $\sigma_1$  are respectively the rms of the field and its first derivatives. These analytical expressions represent useful descriptions of the MFs which, for the case of a Gaussian random field, can be factorized as a function of the threshold and another of the shape and amplitude of the  $C_\ell$ . We will use both the unnormalized ( $V_k$ ) and unnormalized ( $v_k$ ) MFs in the Gaussianity tests performed in this section. The unnormalized functionals are computed with a code that was used for the analysis of Archeops data (Curto et al. 2007) and has been thoroughly validated with *Planck* simulations, while for the normalized ones a code adapted to the high resolution *Planck* data and described in Ducout et al. (2012) is used.

By combining the MFs curves into a vector  $\mathbf{y}$  of size  $n = n_{\text{thresholds}} \times n_{\text{functionals}}$ , a null hypothesis test can be performed using a  $\chi^2$  statistic given by:

$$\chi^2(\mathbf{y}) = (\mathbf{y} - \langle \mathbf{y}_G \rangle)^T \mathbf{C}^{-1} (\mathbf{y} - \langle \mathbf{y}_G \rangle) \quad (21)$$

where  $\mathbf{y}$  represents the MFs of the data,  $\mathbf{y}_G$  those of the simulations and  $\mathbf{C}$  is the covariance matrix. In order to assure convergence, in the case of the four normalized MFs  $\mathbf{C}$  is estimated from  $10^4$  Gaussian simulations, drawn from the *Planck* fiducial power spectrum, having the same instrumental properties of effective beam and noise as the data, the same applied mask and

which have been processed in the same way to reach the corresponding resolution. For the three unnormalized MFs,  $\mathbf{C}$  was estimated from only  $10^3$  FFP6 simulations that proved to be sufficient for convergence. We compare the  $\chi^2_{\text{Planck}}$  obtained from the data to the  $\chi^2$  obtained from those simulations, and report the probability of having a value of  $\chi^2$  larger than the measured one,  $P(\chi^2 > \chi^2_{\text{Planck}})$ . We explore different resolutions represented by the parameter  $N_{\text{side}}$ , different methods of component separation (Commander-Ruler, NILC, SEVEM, and SMICA) and different sky coverages.

First, the three unnormalized MFs ( $V_k$  as a function of  $\nu$ ,  $k = 0, 1, 2$ ) are used to construct a test of the null hypothesis. The test assesses not only the primordial Gaussian hypothesis, but also whether the data is correctly represented by the simulations in terms of power spectrum, systematics and the lensing effect. A set of 17 thresholds between  $-4$  and  $+4$  in steps of  $0.5$  are considered. The comparison between the MFs of the data provided by the four component separation methods and those corresponding to each of the four sets of  $10^3$  FFP6 simulations representing each method, for the standard U73 mask, are shown in Fig. 10. From that figure, a deviation at a level of  $\approx 2\sigma$  can be seen for the contour and genus curves at a resolution  $N_{\text{side}} = 512$ . The situation is very similar for the analyses performed at other resolutions,  $N_{\text{side}} = 1024, 256$  and  $128$ . Although the deviation is not particularly compelling because of the correlations among neighbouring thresholds, it is worth

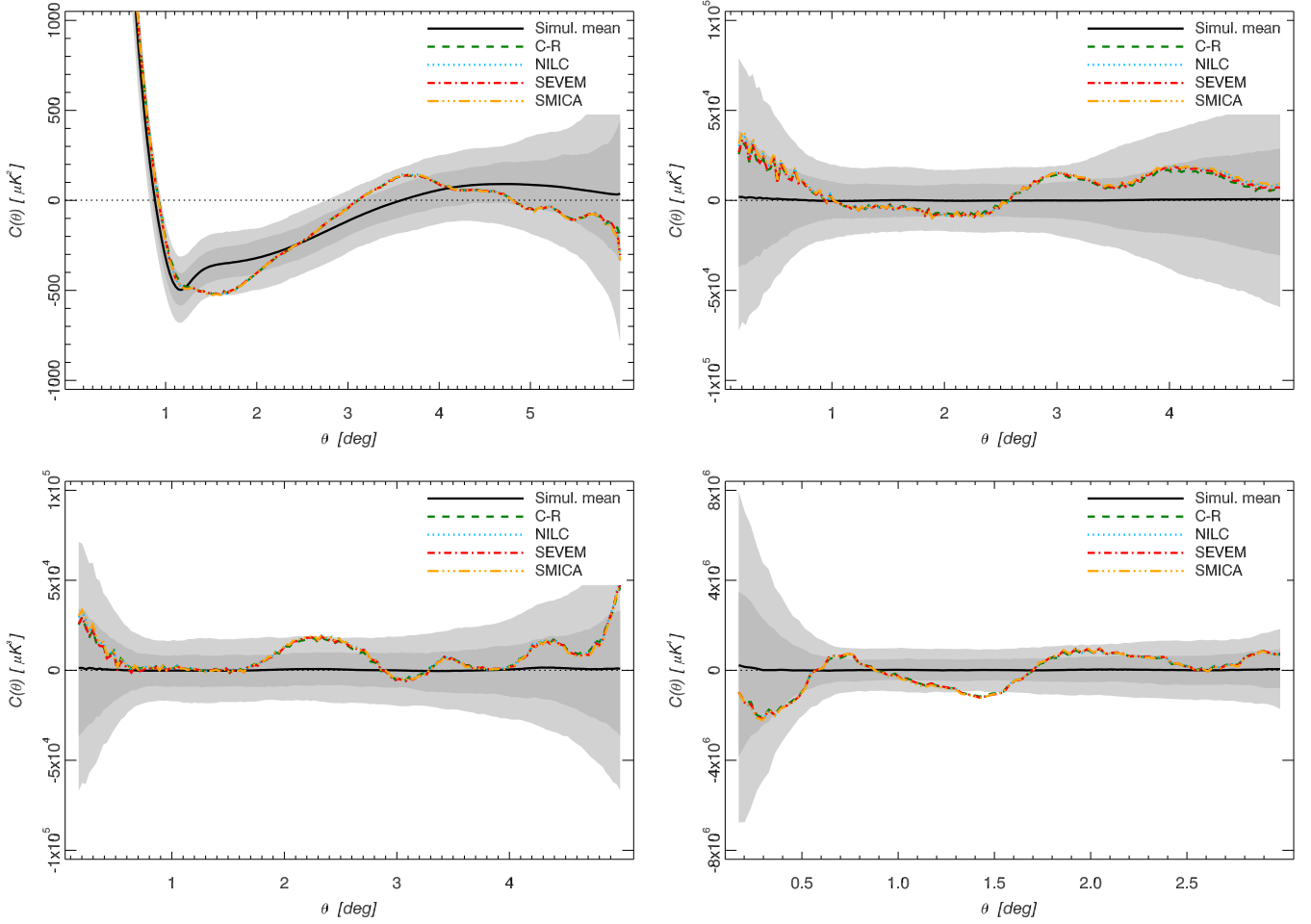


**Fig. 9.** The 2-point (upper left), pseudo-collapsed (upper right), equilateral (lower left) 3-point and reduced rhombic 4-point (lower right) functions averaged over the disc set for the  $N_{\text{side}} = 2048$  CMB estimates. Estimates of the multipoles for  $\ell \leq 60$  are removed from the sky maps. The black solid line indicates the mean for 1000 MC simulations and the shaded dark and light grey regions indicate the 68% and 95% confidence regions, respectively.

mentioning that a possible explanation is the background of unresolved sources that has been detected in *Planck* data with the bispectrum estimators (see Planck Collaboration XXIV (2013)). In order to understand the effect of unresolved sources on the MFs, we added the point source residuals derived from the FFP6 simulations as processed by the SEVEM algorithm to 100 realisations which were then analysed. We conclude that the background of unresolved sources may be responsible for at least part of the excess signal that is detected. The corresponding probabilities  $P(\chi^2 > \chi^2_{\text{Planck}})$  derived from the MF values for each of the four component separation methods and resolutions are given in Table 12. The full resolution maps have been degraded to the lower resolution ones following the procedure described in section 2. All the cases considered are compatible with the null hypothesis.

In the second case, the four normalized MFs  $v_k = V_k/A_k$  ( $k = 0, 1, 2, 3$ ) are used for the null hypothesis test. A set of 26 thresholds equally spaced between  $-3.5$  and  $+3.5$  are considered. The normalization factor  $A_k$  is estimated directly from the maps, having computed previously the moments  $\sigma_0$  and  $\sigma_1$ . This normalization minimizes the dependence of the MFs on the power spectrum, thereby decreasing the cosmic variance and improving their sensitivity to deviations from Gaussianity. The res-

**Table 12.** Non-directional Gaussianity tests using unnormalized MFs:  $P(\chi^2 > \chi^2_{\text{Planck}})$  as a function of sky resolution for different component separation methods.

$N_{\text{side}}$	1024	512	256	128
C-R	0.812	0.299	0.482	0.357
NILC	0.993	0.567	0.354	0.234
SEVEM	0.925	0.911	0.738	0.094
SMICA	0.874	0.675	0.426	0.213

olutions considered in this case are  $N_{\text{side}} = 2048, 1024, 512, 256$  and 128. For the highest resolution  $N_{\text{side}} = 2048$ , the map is smoothed with a Gaussian smoothing kernel with a width  $\theta_{\text{FWHM}} = 5'$ , in order to decrease the noise level. We use the standard U73 mask, inpainting the smallest point sources. The maps at lower resolution are constructed by the standard simple degrading process applied to the original map at  $N_{\text{side}} = 2048$ , and the corresponding masks are degraded following a conservative procedure such that any degraded pixel with a value  $< 0.8$  is set to zero (as explained in section 2). The results of the analysis



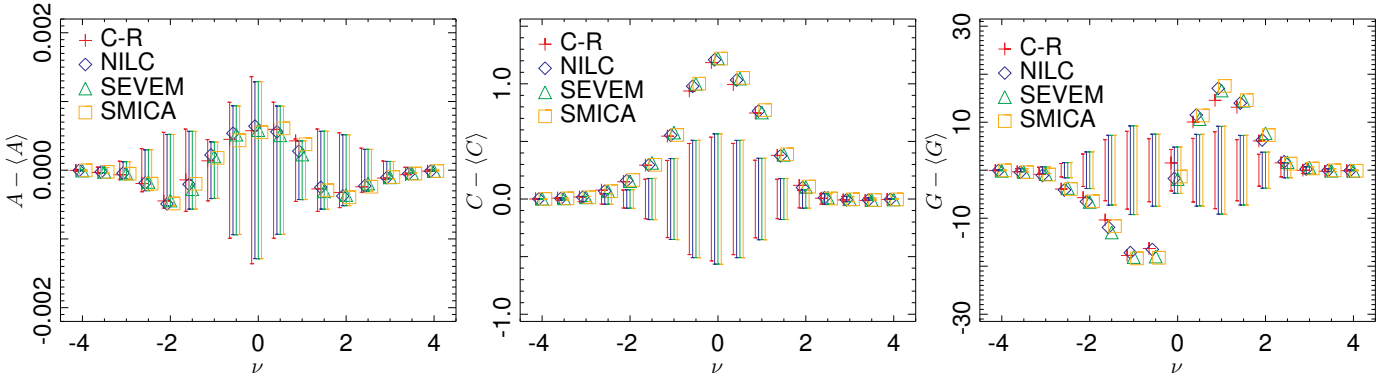


**Fig. 10.** Difference of the data MFs (unnormalized) with respect to the average of the curves obtained with realistic *Planck* simulations for several cleaned maps. From left to right: Area, Contour, Genus. The error-bars represent the  $1\sigma$  (68%CL) dispersions around the mean obtained with simulations.

performed on the SMICA map at different resolutions are presented in Table 13. The results of the analysis performed on the

**Table 13.** Non-directional Gaussianity tests using normalized Minkowski Functionals: dependence of  $P(\chi^2 > \chi^2_{\text{Planck}})$  on Sky resolution.

$N_{\text{side}}$	2048	1024	512	256	128
Normalized MFs	0.358	0.356	0.245	0.225	0.223

different component separation methods at the highest resolution ( $N_{\text{side}} = 2048$ ) are presented in Table 14. The difference of the normalized MFs with respect to the expected values of the null hypothesis as a function of the threshold  $\nu$  are shown in Fig. 11. A slight deviation in  $N_{\text{cluster}}(\nu)$  is noticeable at thresholds  $\nu \approx 0$ , however it is not very compelling since the values at neighboring thresholds are very correlated and this correlation is taken into account in the  $\chi^2$  statistics. Finally, we analyse the depen-

**Table 14.** Non directional Gaussianity tests using normalized Minkowski Functionals: Dependence on component separation methods.

Method	C-R	NILC	SEVEM	SMICA
$P(\chi^2 > \chi^2_{\text{Planck}})$	0.288	0.303	0.415	0.358

dence of the normalized MFs on the sky coverage. We use the standard U73 mask and then decrease the sky coverage by using CL65, CL48 and CL25 masks in combination with a special point source mask that is based on the U73 mask. The fraction of sky left unmasked in the combined masks is 62%, 46% and 23%, respectively. The point source mask is inpainted previously to the analysis. The curves obtained for the different sky coverages are presented in Fig. 12, for the SMICA method. Results of the  $\chi^2$  analysis of the data as a function of sky coverage are compiled in Table 15. All the cases considered are compatible with the null hypothesis.

In summary, we find that the data are globally consistent with the primordial Gaussian hypothesis, and no strong deviation is

found between the data and realistic simulations for both the unnormalized and normalized MFs. We would like to remark that a certain level of non-Gaussianity is expected from lensing and, in particular, from the ISW-lensing signal, thus it is important to compare the data to realistic *lensed* simulations.

**Table 15.** Non directional Gaussianity tests using normalized Minkowski Functionals : Sky coverage.

$f_{\text{sky}}$	0.73	0.62	0.46	0.23
$P(\chi^2 > \chi^2_{\text{Planck}})$	0.358	0.042	0.670	0.780

#### 4.5. Wavelet statistics

A broad range of wavelets have been used in the analysis of CMB data, but in this paper we consider the Spherical Mexican Hat wavelet (SMHW, Martínez-González et al. 2002).

The SMHW is an example of a continuous, non-orthogonal wavelet. Given a signal on the sky,  $T(p)$ , where  $p$  represents a given position/pixel which is a function of the co-latitude  $\theta$  and longitude  $\phi$  (also defined by the unit direction vector  $\mathbf{x}$ ), the SMHW coefficients at a given scale  $R$ ,  $\omega_T(R, p)$ , are obtained by convolution:

$$\omega_T(R, p) = \sum_{\ell=0}^{\ell_{\text{max}}} \sum_{m=-\ell}^{m=\ell} t_{\ell m} W_{\ell}^{\text{SMHW}}(R) Y_{\ell m}(p), \quad (22)$$

where  $W_{\ell}^{\text{SMHW}}(R)$  is the window function associated with the SMHW,  $\ell_{\text{max}}$  is the maximum multipole allowed by the corresponding HEALPix pixelization,  $Y_{\ell m}(p)$  is the spherical harmonic basis, and  $t_{\ell m}$  are the spherical harmonic coefficients of the analysed map:

$$t_{\ell m} = \int d\Omega Y_{\ell m}^*(p) T(p), \quad (23)$$

where  $d\Omega = d\theta \sin \theta d\phi$  and  $*$  denotes complex conjugation.

Several statistics can be computed from the wavelet coefficients map, in particular, the first moments: the dispersion  $\sigma_R$ , the skewness  $S_R$ , and the kurtosis  $K_R$  (as a function of scale  $R$ ).

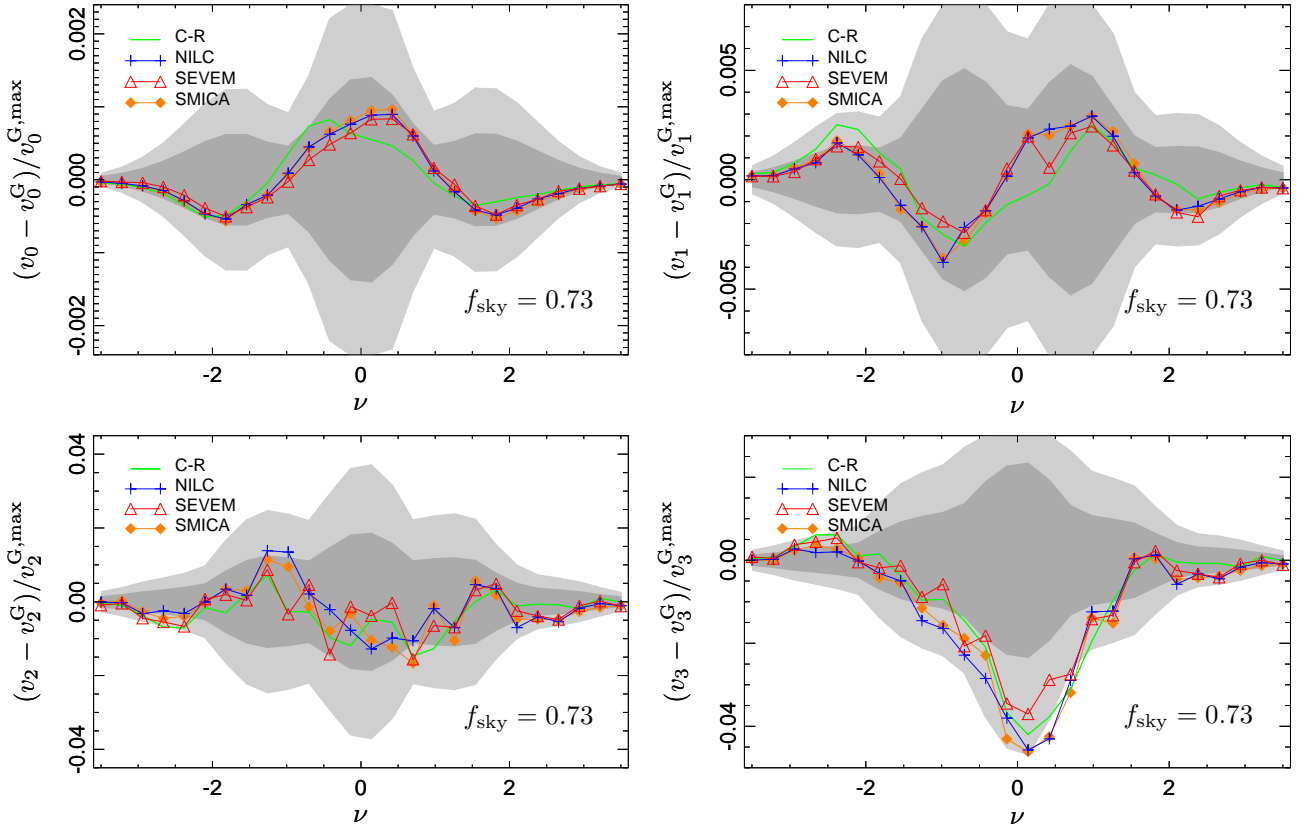


**Fig. 11.** Difference of the normalized MFs obtained from the data with respect to the expected values of the null hypothesis, for the different component separation methods. From left to right and top to bottom: Area, Contour, Genus and  $N_{\text{cluster}}$ . The grey bands represent the 1 and  $2\sigma$  dispersions around zero, based on realistic *Planck* simulations including lensing, for C-R method.

It is interesting to notice that in the case of Gaussian temperature fluctuations the linear transformation involved in the determination of the wavelet coefficients (eqs. 22,23) guarantees that Gaussianity is preserved.

The study of the moments of the distribution of the CMB temperature fluctuations, as a function of the scale, is a standard approach to test the null hypothesis. We have performed a full resolution multi-scale analysis of the four CMB clean maps and computed the quantities  $\sigma_R$ ,  $S_R$  and  $K_R$  from the SMHW wavelet coefficients at 18 scales,  $R = \{2, 4, 7, 14, 25, 50, 75, 100, 150, 200, 250, 300, 400, 500, 600, 750, 900, 1050\}$ , in arc-minutes. These are compared to the standard *Planck* simulations.

As explained in Vielva et al. (2004), when computing the SMHW coefficients of a masked data set, artefacts are introduced close to the mask that degrade the performance of any null hypothesis tests. We therefore define a set of *exclusion masks* such that, at each scale, an extra region of the sky is excluded when performing any statistical test. The exclusion mask for a given scale  $R$  is defined as follows: we build an auxiliary mask by removing from the U73 mask all the features associated with compact objects, and degrade this auxiliary mask to  $N_{\text{side}} = 1024$  (imposing a restrictive cut); a first temporary mask is obtained by extending the borders of this auxiliary mask by a distance of twice  $R$ ; a second temporary mask is obtained, first, by convolving the auxiliary mask with the SMHW at that particular scale  $R$  and, second, by imposing that any pixel of that second temporary mask with an absolute value lower than 0.1 is masked, whereas the remaining ones are set to 1; the two temporary masks are multiplied to yield a single mask that is upgraded

to  $N_{\text{side}} = 2048$ ; finally, the final exclusion mask is obtained by multiplying this mask by the parent U73 mask.

The comparison of the four CMB maps with the corresponding simulations is summarized in Fig. 13. The three panels show (from left to right) the statistical significance of the standard deviation, the skewness and the kurtosis (as a function of the SMHW scale). The points represent the upper tail probability associated to a given statistic, i.e., the fraction of the simulations that present a value of a given statistic equal to or greater than the one obtained for the data. In fact, we define a modified upper tail probability: if an upper tail probability is larger than 0.5, then a new quantity is defined as 1 minus that upper tail probability. Hence, this modified definition of the upper tail probability is constrained between  $10^{-3}$  (the minimum value that can be imposed with 1000 simulations) and 0.5. Overall, the agreement between the four CMB maps is quite good, showing that all of them provide a consistent estimation of the true CMB. However, several aspects need to be discussed. Let us clarify that the differences among the CMB methods for small modified upper tail probabilities are expected to be larger than for large modified upper tail probabilities. This is because a small modified upper tail probability is determined by a small number of simulations and, therefore, has a relatively large error bar. In other words, the tails of the distributions of the different statistics are quite sparsely sampled.

We will distinguish between the small ( $R \lesssim 10'$ ), intermediate ( $10' \lesssim R \lesssim 500'$ ) and the large ( $R \gtrsim 500'$ ) scale regimes. Let us focus on the three statistics independently. We will highlight

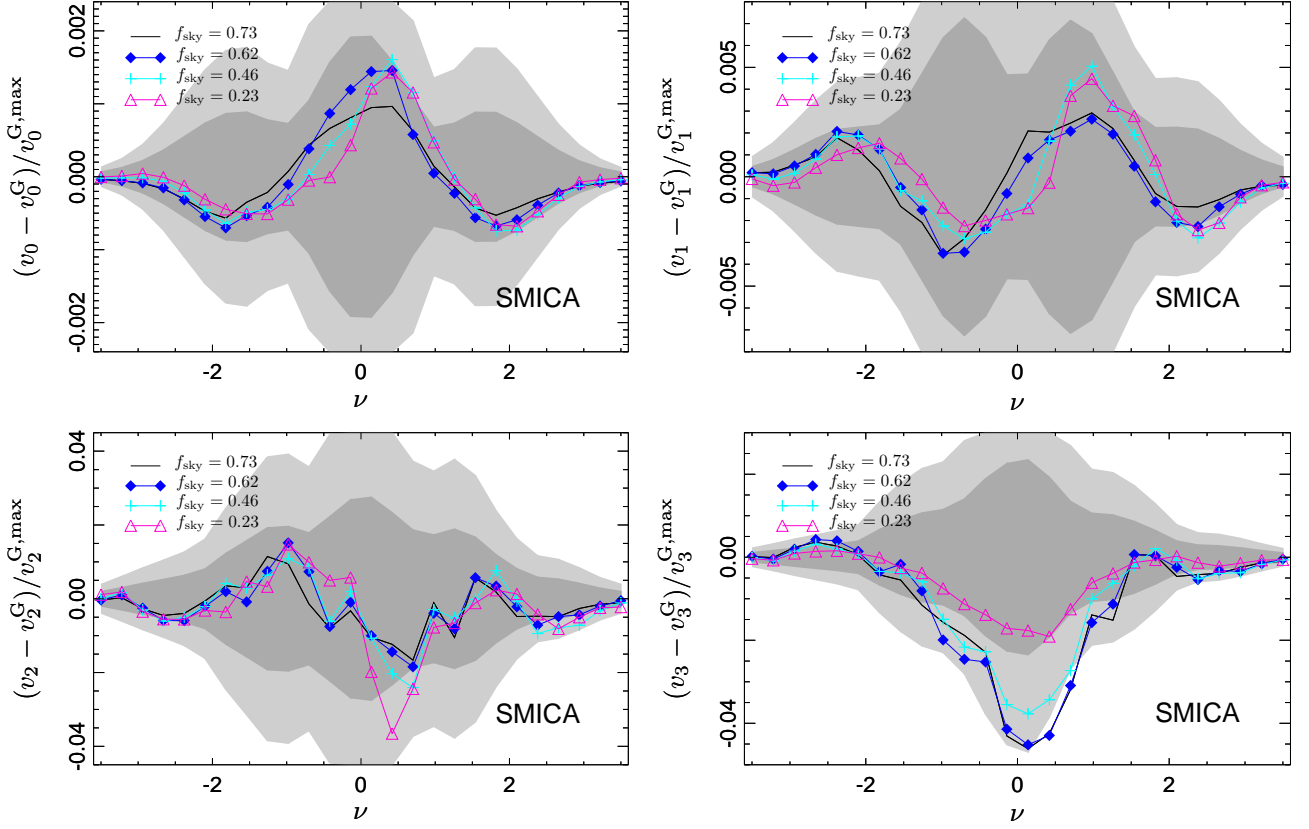


**Fig. 12.** Difference of the normalized MFs obtained from the data with respect to the expected value of the null hypothesis for several sky coverages. The SMICA map is considered. From left to right and top to bottom: Area, Contour, Genus and  $N_{\text{cluster}}$ . The grey bands represent the 1 and  $2\sigma$  dispersions around zero, based on realistic *Planck* simulations including lensing, for  $f_{\text{sky}} = 0.23$ .

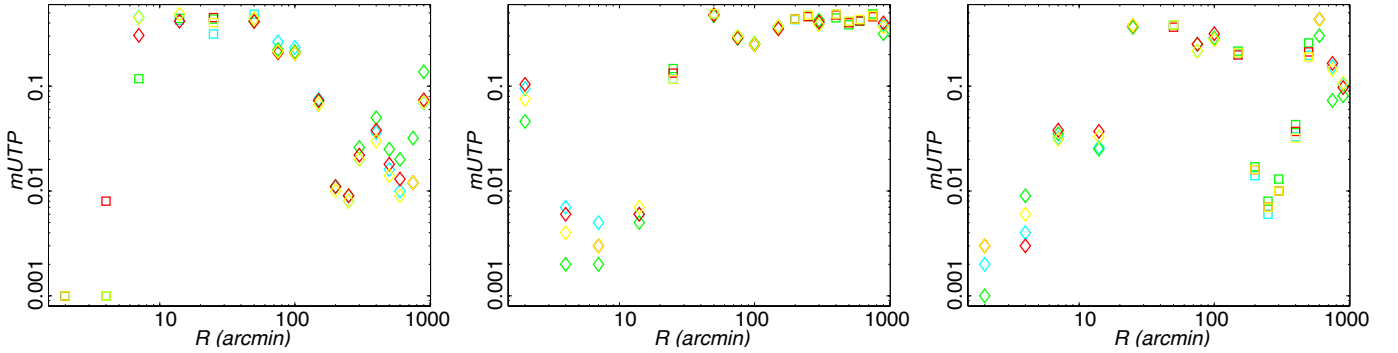


**Fig. 13.** Standard deviation (left), skewness (centre) and kurtosis (right) of the SMHW coefficients as a function of the wavelet scale  $R$ . Results are given for the four *Planck* CMB maps (green: Commander-Ruler, light-blue: NILC; red: SEVEM; yellow: SMICA). Modified upper tail probabilities ( $mUTP$ , see text for details) are obtained by comparing with 1000 simulations processed through the component separation pipelines. Squares represent modified upper tail probabilities that correspond to an actual upper tail probability above 0.5; diamonds represent upper tail probabilities below 0.5.

the most important features and, afterwards, we will try to find an explanation for them:

- On the smallest scales, the four CMB maps show a dispersion in SMHW coefficients significantly larger than seen in the simulations. However on larger scales, the dispersion is systematically below the median of the simulations and, on scales of  $R \approx 5^\circ$ , the modified upper tail probability is approximately 0.015.
- Regarding the skewness, all four maps yield a value that is significantly lower (with a modified upper tail probability of around 0.004) than expected from the simulations in the small scale regime (except for the smallest one, where the deviation is around 0.07). The rest of the scales are fairly compatible with the null hypothesis.
- The kurtosis is also smaller than expected in the small scale regime. Overall, the modified upper tail probability is about 0.03. At scales of around  $300'$ , an anomalously large value

(modified upper tail probability of approximately 0.01) is found.

These results are compatible with the values reported for *WMAP* data (Vielva et al. 2004; Cruz et al. 2005), over the scales common to both experiments (i.e.,  $R > 10'$ ). In particular, the large value of the kurtosis has been associated with the Cold Spot (Vielva et al. 2004). We will return to this topic specifically in Sect. 5.8. The low variance of the wavelet coefficients was previously seen in Vielva et al. (2004); Wiaux et al. (2008). In addition, the low dispersion at scales above a few degrees is likely to be related to the low variance anomaly detected in *WMAP* (Monteserín et al. 2008; Cruz et al. 2011), that is also seen in the *Planck* data (see Sect. 4.1).

We have also studied the robustness of the results for different masking scenarios. In particular, we have investigated variations in the results when we adopt, as auxiliary masks to define the exclusion masks, the two CG70 and CG60 masks removing 30% and 40% of the sky, respectively. Note that the auxiliary masks obtained from the U73 mask already cut around 20% of the sky. The corresponding results for the SMICA map are presented in Fig. 14. The conclusions are similar for the other CMB maps. For the dispersion of the wavelet coefficients, we do not notice any significant change in the anomalously high value obtained for the SMICA map at the smallest scales. However, some changes are observed at larger scales. In this regime, it seems that the most significant deviation occurs for the CG70 mask (modified upper tail probability of around 0.005), whereas similar (and slightly less significant) modified upper tail probabilities are obtained for both the U73 (modified upper tail probability of approximately 0.015) and the CG60 (modified upper tail probability of about 0.01) masks. A possible explanation for this behaviour would be that a less restrictive mask admits some residual contamination from Galactic foregrounds, thus increasing the dispersion of the wavelet coefficients, and artificially increasing their inconsistency with the null hypothesis. In principle, the larger the Galactic cut, the lower would be the dispersion of the wavelet coefficients (assuming that some residual contamination of the Galactic foregrounds is left) and, therefore, the smaller the upper tail probability. However, as we already said, the modified upper tail probability for the dispersion is higher for the CG60 mask than for the CG70 mask. This apparent contradiction could be resolved by accounting for the larger sampling variance for smaller areas, that would result in a lower significance for the anomaly.

The anomalous kurtosis at scales of  $R \approx 300'$  shows an overall stable modified upper tail probability of around 0.01 – 0.03. In the small scale regime, the differences are better defined: the smaller the mask, the more significant the deviation (characterized by the low value of the kurtosis). In particular, the modified upper tail probability associated with the CG60 mask is 0.001, around 0.009 for CG70, and approximately 0.03 for the U73 mask. A similar pattern is also observed for the skewness on these scales, although the three masks results in more similar upper tail probabilities, between around 0.001 and 0.007 (except for the smallest scale).

It is therefore clear that there is some inconsistency between the CMB data and the corresponding simulations. On intermediate scales, both the low dispersion and the high kurtosis could be related to previously known anomalies: the low variance and the Cold Spot. On the smallest scales, the three statistics report a low upper tail probability independently of the mask coverage — it is important to determine what this inconsistency is due to. Besides the possibility that it is an intrinsic cosmological sig-

nal, the non-Gaussianity could be caused either by instrumental systematics or residual foreground contamination.

In the former case, we have considered whether the origin of the signal could be related to properties of the noise that are inadequately modelled by the simulations. In particular, we have studied the statistical properties of the half-ring half-difference maps generated by the four component separation algorithms as proxies for the noise present in the CMB maps. Although in detail there are some discrepancies between these noise estimates and the simulated ones, they are not compatible with the inconsistencies observed between the CMB map and simulations. Therefore, a systematic effect associated with the instrumental noise does not provide a satisfactory explanation for the small-scale deviations.

In the latter case, an obvious candidate is due to the contribution from residual unresolved point sources in the clean CMB maps. Although the brightest point sources are masked, and the component separation process itself can suppress the amplitude of the unresolved background of point sources, some signal will remain. Indeed, in Planck Collaboration XXIV (2013) it has been determined that the bispectrum of this contribution is clearly detected in the four CMB *Planck* maps, at a significance in excess of  $4\sigma$ . In addition, the dispersion of the wavelet coefficients is higher than expected, which is also compatible with the presence of an additional signal. We therefore consider this as the most likely non-CMB explanation for the observed signal.

#### 4.6. Bispectrum

The CMB bispectrum is the three point correlator of the  $a_{\ell m}$  coefficients,

$$B_{m_1 m_2 m_3}^{\ell_1 \ell_2 \ell_3} = a_{\ell_1 m_1} a_{\ell_2 m_2} a_{\ell_3 m_3}. \quad (24)$$

In this paper, we focus on the bispectrum reconstruction as a blind test of non-Gaussianity. Therefore, we assume we are seeking a non-trivial bispectrum that has arisen through a physical process which is statistically isotropic, that is, we can employ the angle-averaged bispectrum  $B_{\ell_1 \ell_2 \ell_3}$ ,

$$B_{\ell_1 \ell_2 \ell_3} = \sum_{m_i} h_{\ell_1 \ell_2 \ell_3}^{-1} \mathcal{G}_{m_1 m_2 m_3}^{\ell_1 \ell_2 \ell_3} B_{m_1 m_2 m_3}^{\ell_1 \ell_2 \ell_3}, \quad (25)$$

where  $h_{\ell_1 \ell_2 \ell_3}$  is a geometrical factor,

$$h_{\ell_1 \ell_2 \ell_3} = \sqrt{\frac{(2\ell_1 + 1)(2\ell_2 + 1)(2\ell_3 + 1)}{4\pi}} \begin{pmatrix} \ell_1 & \ell_2 & \ell_3 \\ 0 & 0 & 0 \end{pmatrix}, \quad (26)$$

and  $\mathcal{G}_{m_1 m_2 m_3}^{\ell_1 \ell_2 \ell_3}$  is the Gaunt integral,

$$\begin{aligned} \mathcal{G}_{m_1 m_2 m_3}^{\ell_1 \ell_2 \ell_3} &\equiv \int d\Omega Y_{\ell_1 m_1}(\mathbf{n}) Y_{\ell_2 m_2}(\mathbf{n}) Y_{\ell_3 m_3}(\mathbf{n}) \\ &= h_{\ell_1 \ell_2 \ell_3} \begin{pmatrix} \ell_1 & \ell_2 & \ell_3 \\ m_1 & m_2 & m_3 \end{pmatrix}, \end{aligned} \quad (27)$$

with the usual Wigner-3j symbol  $\begin{pmatrix} \ell_1 & \ell_2 & \ell_3 \\ m_1 & m_2 & m_3 \end{pmatrix}$ . It is more convenient to eliminate the geometrical factors entirely and to work with the reduced bispectrum which is defined as

$$b_{\ell_1 \ell_2 \ell_3} = h_{\ell_1 \ell_2 \ell_3}^{-1} B_{\ell_1 \ell_2 \ell_3}. \quad (28)$$

Note that the CMB bispectrum  $b_{\ell_1 \ell_2 \ell_3}$  is defined on a tetrahedral domain of multipole triples  $\{\ell_1 \ell_2 \ell_3\}$  satisfying both a triangle condition and a limit given by the maximum resolution  $\ell_{\max}$  of the experiment. A much more extensive introduction to the bispectrum can be found in Planck Collaboration XXIV (2013).

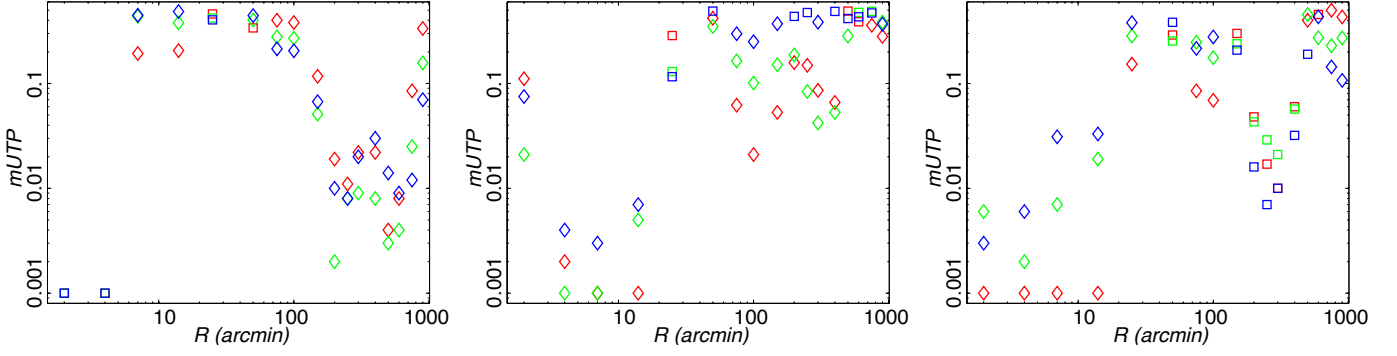


**Fig. 14.** Standard deviation (left), skewness (centre) and kurtosis (right) of the SMHW coefficients as a function of the wavelet scale  $R$ . Results are given for the SMICA CMB map. Several masking scenarios are compared: red: CG60 mask (cutting out 40% of the sky); green: CG70 mask (cutting out 30% of the sky); blue: U73 mask. The modified upper tail probabilities ( $mUTP$ ) are defined in the text.

Modal, wavelet and binned bispectrum estimators filter the CMB map with separable basis functions

$$Q_{ijk}(\ell_1, \ell_2, \ell_3) = q_i(\ell_1) q_j(\ell_2) q_k(\ell_3) + \text{perms}, \quad (29)$$

to find the corresponding modal coefficients  $\beta_{ijk}$  (or  $\beta_n$  because it is convenient to order the  $ijk$  with label  $n$ ). For appropriately orthonormalised basis functions  $Q_{ijk}(\ell_1, \ell_2, \ell_3)$ , these coefficients can be used to reconstruct the CMB bispectrum through the signal-to-noise weighted expansion

$$\frac{b_{\ell_1 \ell_2 \ell_3}}{\sqrt{C_{\ell_1} C_{\ell_2} C_{\ell_3}}} = \sum_n \beta_{ijk} Q_{ijk}(\ell_1, \ell_2, \ell_3). \quad (30)$$

This reconstruction method has been extensively validated, showing the accurate recovery of CMB bispectra from non-Gaussian simulated maps, and it has been applied to the *WMAP* seven year data to reconstruct the full 3D CMB bispectrum (Fergusson et al. 2010b). To quantify whether or not there is a model-independent deviation from Gaussianity, we can consider the total integrated bispectrum. By summing over all multipoles, we can define an integrated nonlinearity parameter  $\bar{F}_{\text{NL}}$  which, with the orthonormal modal decomposition (30), becomes (Fergusson et al. 2010b)

$$\bar{F}_{\text{NL}}^2 = \frac{1}{N_{\text{loc}}^2} \sum_{\ell_i} \frac{h_{\ell_1 \ell_2 \ell_3}^2 b_{\ell_1 \ell_2 \ell_3}^2}{C_{\ell_1} C_{\ell_2} C_{\ell_3}} = \frac{\sum_{ijk} \beta_{ijk}^2}{\sum_{ijk} \alpha_{ijk}^{\text{loc}2}}. \quad (31)$$

where  $N_{\text{loc}}$  is the normalisation for the local  $f_{\text{NL}} = 1$  model (with coefficients  $\alpha_{ink}^{\text{loc}}$ ). For ideal Gaussian CMB maps, the quantity  $\bar{F}_{\text{NL}}^2$  should obey a  $\chi^2$ -distribution with a mean given by the number of degrees of freedom (the modes)  $\mu = n_{\text{max}}$  and with a variance  $\sigma^2 = 2n_{\text{max}}$ . Assuming that the three-point correlator is the leading non-Gaussian contribution, then  $\bar{F}_{\text{NL}}$  provides a blind test for the presence of any integrated CMB bispectrum (once the expected two-point term is subtracted). We note that this is less sensitive than targeted searches for particular bispectrum shapes.

First, we discuss reconstructions from the modal estimator which has passed successfully through the full suite of non-Gaussian bispectrum validation tests (for further details about bispectrum estimators, see Planck Collaboration XXIV 2013). We have applied this to the *Planck* temperature maps for the foreground-separation techniques NILC, SEVEM and SMICA, using two alternative sets of hybrid basis functions in order to cross-check results and identify particular signals. These are

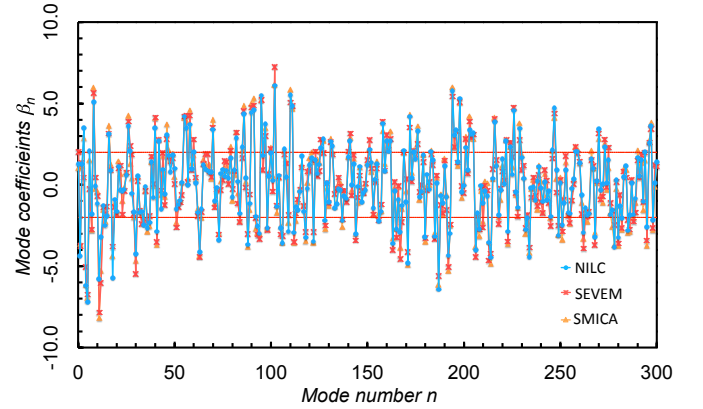


**Fig. 15.** *Planck* recovered bispectrum coefficients  $\beta_n^R$  for the mode expansion (30) using hybrid Fourier modes (augmented with local and ISW modes). There is remarkable consistency between results from the different component separation methods, NILC, SEVEM, and SMICA. The variance from simulated noise maps is nearly constant for each of the 300 modes, with the average  $\pm 1\sigma$  variation shown in red.

Fourier modes ( $n_{\text{max}} = 300$ ) augmented a local SW mode and the separable ISW modes and a hybrid polynomial/local basis with  $n_{\text{max}} = 600$ , previously described in Fergusson et al. (2010a). These basis function sets ensured excellent correlation with primordial modes and the ISW signal. As with all the other bispectrum analyses based on spherical harmonic coefficients, we used the U73 mask to which we applied inpainting. Together with the foreground separated maps, noise simulations were provided which were used to calibrate the estimator's linear correction term and to determine the variance.

The modal coefficients  $\beta_n^R$  extracted from the *Planck* NILC, SEVEM, and SMICA maps are shown in Fig. 15 for the hybrid Fourier basis. These amplitudes show remarkable consistency between the different maps, with shape cross-correlations better than 96% and the overall amplitudes to within 7% agreement. This demonstrates that the independent foreground separation techniques do not appear to be introducing spurious non-Gaussianity. The  $\beta_n^R$  coefficients have a roughly constant variance, so anomalously large modes can be easily identified. For



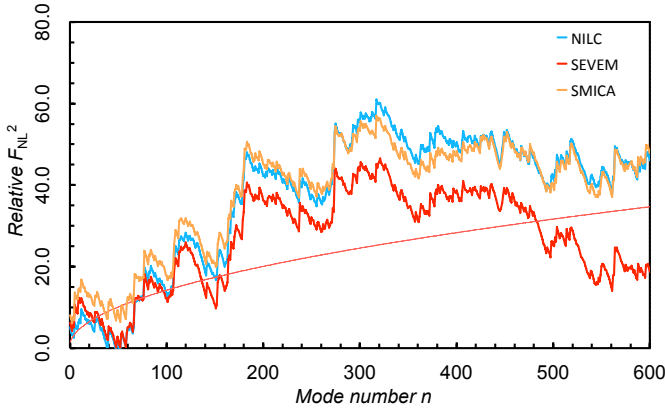


**Fig. 16.** Cumulative sum of orthonormal mode contributions  $\beta_n^{R2}$  to the total integrated bispectrum  $\bar{F}_{NL}^2$  defined in (31). The relative quantity  $\bar{F}_{NL}^2 = F_{NL}^2 - F_{NL}^{G2}$  is plotted, where  $F_{NL}^{G2}$  is the mean obtained from 200 CMB Gaussian maps and the standard deviation is the red line. A hybrid polynomial basis  $n_{\max} = 600$  is employed in the signal-dominated region  $\ell < 1500$ . This  $\chi^2$ -test for the independent modes is cumulatively consistent with Gaussianity.

example, we have subtracted the expected ISW signal and the estimated point source contributions, explaining the large signal at low  $n$ . The corresponding quantity  $\bar{F}_{NL}^2$  defined in (31), that can be seen in Fig. 16, shows consistency with the null hypothesis. Using the modal expansion (30), we have reconstructed the full 3D *Planck* bispectrum which is illustrated in Fig. 17 for SMICA (large) but also NILC and SEVEM; the reconstructions are visually indistinguishable. There are some striking features evident, notably the presence of a significant ISW modal contribution in the squeezed limit along the edges of the tetrapyd which has an oscillatory and flattened appearance. At large multipoles  $\ell$  approaching  $\ell_{\max} = 2000$ , there is increased randomness in the reconstruction due to the rise in experimental noise and some evidence for a residual point source contribution. For the present *Planck* estimator configurations, the modal bispectrum estimator is more democratic, that is, it is capable of resolving the large- $\ell$  contributions near  $\ell_{\max}$  seen in Fig. 15, and not only the multipoles associated with primordial models.

In Fig. 18, we show a comparison of the  $\ell < 500$  *Planck* bispectrum signal and that reconstructed from the *WMAP* seven-year data (Fergusson et al. 2010b). Here for consistency we show the *Planck* signal from the second polynomial basis, since polynomials were used in the original *WMAP7* analysis. The *Planck* signal pattern correlates well with the *WMAP* bispectrum obtained previously, despite the different domains used for the modal analysis of the two different experiments.

Similarly to the modal bispectrum, a wavelet decomposition can be used to reconstruct the bispectrum. Here we use the continuous, non-orthogonal Spherical Mexican Hat Wavelet (SMHW, Martínez-González et al. 2002). Cubic moments  $q_{ijk}$  are defined in terms of the SMHW coefficients for three different angular scales  $R_i, R_j, R_k$  (Curto et al. 2009b,a, 2010, 2011a,b)

$$q_{ijk} = \frac{1}{4\pi} \frac{1}{\sigma_i \sigma_j \sigma_k} \int d\mathbf{n} w(R_i, \mathbf{n}) w(R_j, \mathbf{n}) w(R_k, \mathbf{n}) \quad (32)$$

where  $\sigma_i$  is the dispersion of the wavelet coefficient map  $w(R_i, \mathbf{n})$ . Considering the covariance matrix of the  $q_{ijk}$  moments,

**Table 16.**  $\chi^2$  statistics based on the wavelet bispectrum reconstruction  $y_i$  statistics for the foreground cleaned data map. Considered data map: combined map cleaned with C-R, NILC, SEVEM, and SMICA.

Method	$\chi^2_{\text{data}}$	DOF	$\langle \chi^2 \rangle$	$\sigma$	$P(\chi^2 \geq \chi^2_{\text{data}})$
C-R	874	690	740	87	0.074
NILC	883	682	731	83	0.045
SEVEM	858	682	731	83	0.070
SMICA	878	682	732	83	0.058

$\mathbf{C} \equiv \langle \mathbf{q}\mathbf{q}^T \rangle$ , and its eigenvector decomposition,  $\mathbf{C} = \mathbf{R}\mathbf{D}\mathbf{R}^T$ , with  $\mathbf{R}$  the eigenvector matrix and  $\mathbf{D}$  the eigenvalue matrix, a new set of quantities  $\mathbf{y} \equiv \mathbf{D}^{1/2}\mathbf{R}^T\mathbf{q}$  is defined. Considering the decorrelation produced by the convolution of the SMHW on the temperature anisotropies and applying the central limit theorem to the averages defined in Eq. 32, then the  $q_{ijk}$  quantities are expected to have a nearly Gaussian distribution. Therefore, the  $\mathbf{y}$  quantities are nearly multinormal and satisfy  $\langle \mathbf{y}\mathbf{y}^T \rangle = \mathbf{I}$  and  $\langle \mathbf{y} \rangle = \mathbf{0}$  (Curto et al. 2011a).

We have computed this reconstruction using the *Planck* data and compared with the null hypothesis (Gaussian *Planck* simulations). The considered data map is the resulting map after foreground cleaning based on different cleaning procedures: Commander-Ruler, NILC, SEVEM, and SMICA. The mask used is the U73 one (contrary to the modal reconstruction, no inpainting of the point sources is made in this case). In Fig. 19 the  $\mathbf{y}$  statistics corresponding to the *Planck* data are plotted and compared with the  $3\sigma$  error-bars obtained with *Planck* Gaussian simulations. From the list of different  $q_{ijk}$  statistics corresponding to the 16 angular scales described in Planck Collaboration XXIV (2013), there are 11, 4, 3, 3 statistics with  $|y_i| \geq 3$  (corresponding to Commander-Ruler, NILC, SEVEM, and SMICA respectively). The error-bars are obtained with *Planck* simulations for each type of component separation cleaned map. The error-bars of the  $y_i$  statistics for low indices  $i$  are associated to large scales where the  $\mathbf{q}$  statistics have a less Gaussian-like shape. The  $\mathbf{y}$  statistics are combined into a  $\chi^2$  test after a principal component analysis with a threshold of  $10^{12}$  (Curto et al. 2011a) and compared with the  $\chi^2$  statistics obtained from *Planck* Gaussian simulations for each type of component separation method (see Table 16). The  $\chi^2$  statistic corresponding to the data is compatible with the values obtained from Gaussian simulations according to the cumulative probability  $P(\chi^2 \geq \chi^2_{\text{data}})$ , as can be seen in Table 16. Therefore the wavelet bispectrum reconstruction does not detect a significant amplitude of bispectrum in the considered data maps. Details on the constraints on the amplitude of different bispectrum shapes are presented in Planck Collaboration XXIV (2013).

## 5. Intriguing inconsistencies – *WMAP* anomalies revisited.

In the previous section, we have established that the *Planck* data shows little evidence for non-Gaussianity beyond that expected due to the ISW-lensing effect (which is accounted for directly by simulations), and contributions from residual unresolved point sources. The exceptions are on large-angular scales where features consistent with various anomalies previously seen in the *WMAP* data have been observed. In this section, we explicitly consider several of the most important anomalies detected

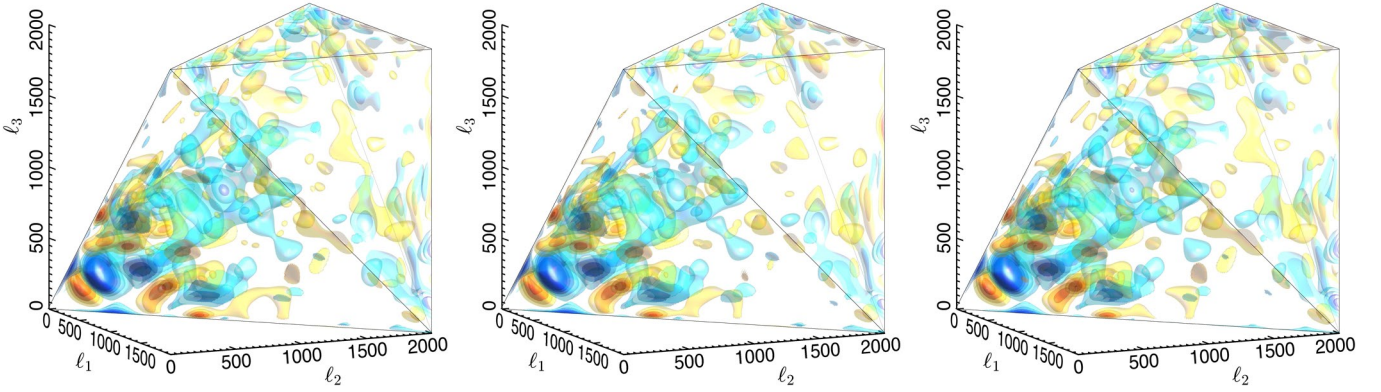


**Fig. 17.** Full 3D CMB bispectrum recovered from the Planck foreground-separated maps (modes illustrated in fig. 15, including SMICA (left), NILC (centre) and SEVEM (right)). These are plotted in three-dimensions with multipole coordinates  $\{\ell_1, \ell_2, \ell_3\}$ ; the triangle condition restricts the bispectrum to a tetrahedral domain out to the experimental resolution limit  $\ell < \ell_{\max} = 2000$ . Several density contours are plotted with red positive and blue negative. The bispectra from different component-separation methods are almost indistinguishable with the same features also appearing in Fourier and polynomial expansions. Note the central and flattened features for  $\ell < 1200$  and also the oscillating CMB ISW lensing signal in the squeezed limit along the edges of the tetrapyd.

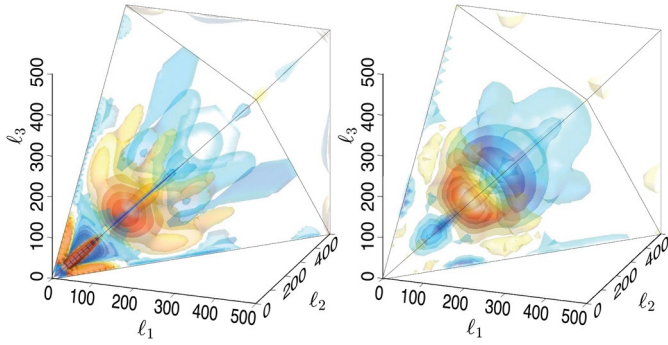


**Fig. 18.** Comparison between the *WMAP* seven-year bispectrum signal (left) (Fergusson et al. (2010b)) and the low- $\ell$  signal of *Planck* (right) reconstructed from the SMICA foreground-separated map (in both cases using polynomial modes). The same basic patterns are observed in both bispectra, including an apparent central ‘oscillatory’ feature.

in the *WMAP* data, namely the quadrupole-octopole alignment (Sect. 5.1), the low variance (Sect. 5.2), hemispherical asymmetry (Sect. 5.3), phase correlations (Sect. 5.4), dipolar power modulation (Sect. 5.5), generalized power modulation (Sect. 5.6), parity asymmetry (Sect. 5.7) and the Cold Spot (Sect. 5.8). Each of these anomalies may represent different violations of the fundamental properties of isotropy and/or Gaussianity of the CMB data which are assumed in the estimation of the CMB power spectrum.

There is an ongoing debate about the significance of these anomalies in the literature. A critical issue relates to the role of a posteriori choices — whether interesting features in the data bias the choice of statistical test or if arbitrary choices in the subsequent data analysis enhance the significance of the features. Indeed, the *WMAP* team (Bennett et al. 2011) contends that the anomalies are significantly over-interpreted due to such selections, whilst other authors claim highly significant and robust detections. Therefore, care must be taken to address the issue, since our analyses necessarily follow up tests of the previous *WMAP* investigations. However a careful and fair statistical treatment can allow us to study possible links among the anomalies and to search for a physical interpretation.

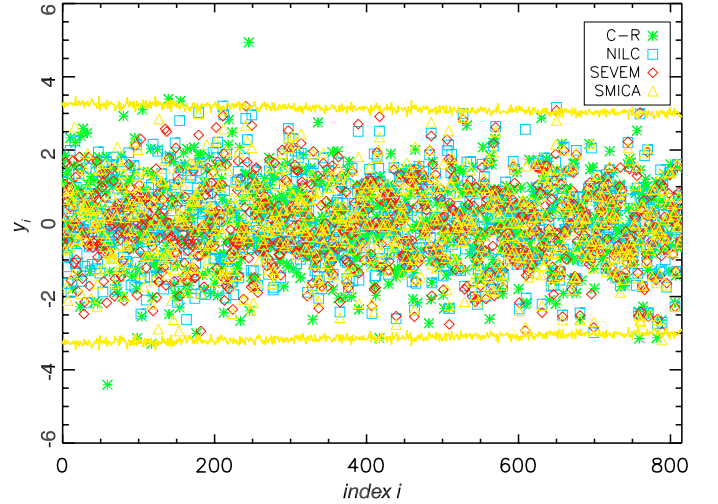


**Fig. 19.** The wavelet bispectrum reconstruction  $y_i$  statistics for the foreground cleaned *Planck* data map. Considered data map: combined map cleaned with C-R, NILC, SEVEM and SMICA. The solid yellow lines represent the  $3\sigma$  error-bars for SMICA (similar error-bars are obtained for C-R, NILC, and SEVEM maps).

### 5.1. Mode alignment

Tegmark et al. (2003) first reported a significant alignment between the orientation of the quadrupole and the octopole in the *WMAP* first year temperature data. We study this quadrupole-octopole alignment in the *Planck* data using the maximization of the angular momentum dispersion as described in de Oliveira-Costa et al. (2004). Specifically, we determine the orientation of the multipoles by finding the axis  $\mathbf{n}$  around which the angular momentum dispersion

$$\sum_m m^2 |a_{\ell m}(\mathbf{n})|^2 \quad (33)$$

is maximized. Here,  $a_{\ell m}(\mathbf{n})$  denotes the spherical harmonics coefficients of the CMB map in a rotated coordinate system with its z-axis in the  $\mathbf{n}$ -direction. This definition of the multipole-orientation has been devised for planar multipoles and is sim-



ply the direction perpendicular to the plane in which most of the power of the multipole lies. It is thus intuitive and easy to use. Note that the value of the statistic in Eq. (33) is the same for  $-\mathbf{n}$  as for  $\mathbf{n}$ , i.e. the multipole orientation is defined only up to a sign.

An alternative method, based on the multipole vector decomposition (Copi et al. 2004; Schwarz et al. 2004; Bielewicz et al. 2005; Bielewicz & Riazuelo 2009) of the data has also been used to verify the robustness of the results presented here, and excellent consistency is found.

Residual foregrounds (mostly on the Galactic plane) present in the four *Planck* CMB estimates could influence the reconstruction of the low-order multipoles. However, when a mask applied, the resulting mode-coupling can also affect the reconstruction of the low- $\ell$  multipoles. We therefore utilise Wiener filtered maps computed from the data to which the U73 mask is applied. Specifically, we utilise the same implementation of the Wiener filter as used in Planck Collaboration P09A (2013) i.e., a messenger method as described by Elsner & Wandelt (2013). A direct inversion method for masked data (Efstathiou 2004; Bielewicz et al. 2004, 2013) is a possible alternative, but the Wiener filtered maps result in a significantly smaller uncertainty in the reconstructed orientation of the multipoles.

We then search for the preferred orientation by explicitly rotating the CMB map such that the z-axis pierces the centre of all the low resolution pixels defined at  $N_{\text{side}} = 16$ , and then subsequently refine the search by using an  $N_{\text{side}} = 2048$  map. The angular resolution for the orientation of the multipoles is thus given by the distance between the pixel centers of the  $N_{\text{side}} = 2048$  map, which is of order  $1.94'$ . Figure 20 shows the Wiener filtered SMICA CMB sky, with the corresponding reconstruction of the quadrupole and octopole moments. The reconstructed orientations are quite robust with respect to the component separation method used for reconstructing the CMB. The significance of the alignment between the quadrupole and the octopole is assessed from the scalar product of their orientations, compared to values derived from the standard set of 1000 MC simulations. The orientation, the angular distance the scalar-product between quadrupole and octopole, and the probability of at least such an alignment to occur in an isotropic universe are summarised in Table 17 for each CMB map.

We find that, depending on the component separation method, the quadrupole and octopole orientations are misaligned by an amount between  $9^\circ$  and  $13^\circ$ . This is larger than the  $3^\circ$  reported recently by Bennett et al. (2012) for the 9-year *WMAP* ILC map. In consequence, our significance of the quadrupole-octopole alignment is substantially smaller than for the *WMAP* data, falling to almost 98% confidence level for the Commander-Ruler and SEVEM maps and 96.7% confidence level for the NILC map.

## 5.2. Variance, skewness and kurtosis anomalies

A low value for the variance on the CMB sky was previously observed in the *WMAP* data by Monteserín et al. (2008) and Cruz et al. (2011), and confirmed for *Planck* in Sect. 4.1. Furthermore, the effect has also been seen in the wavelet analysis of Sect. 4.5 where the variance of the SMHW coefficients is low at scales between 400 and 600 arcmin (Fig. 13). In addition, anomalous behaviour was also observed for the skewness and kurtosis in low resolution maps at  $N_{\text{side}} = 16$ . Here, we reassess these results and determine their robustness to masking and data selection. The former will allow us to determine whether a particular

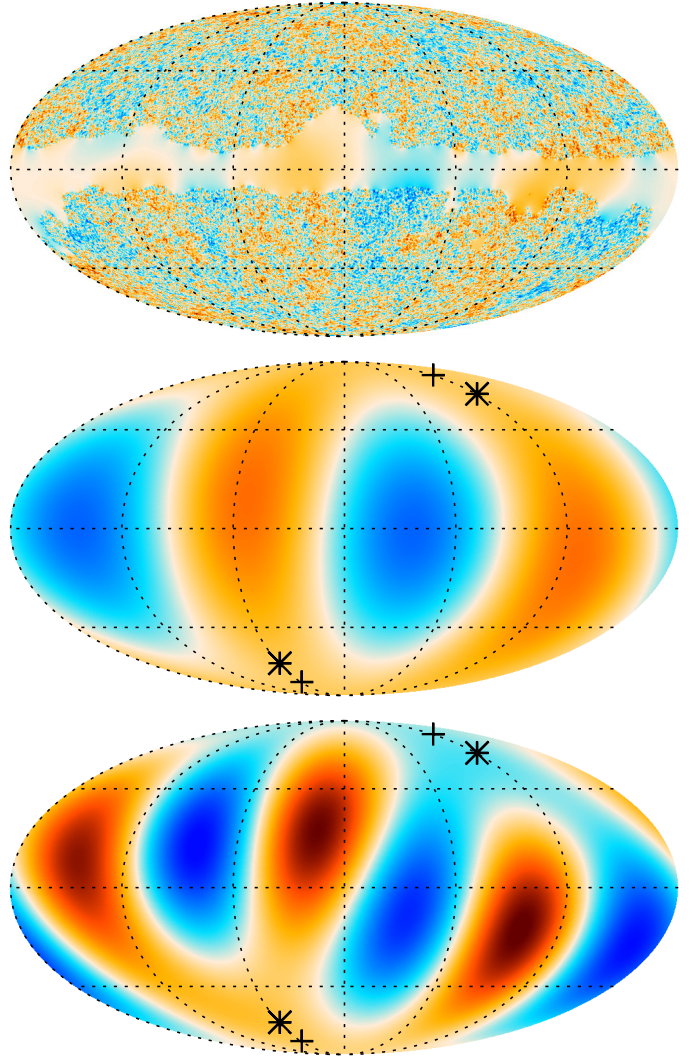


**Fig. 20.** Upper: The Wiener filtered SMICA CMB sky (temperature range  $\pm 400 \mu\text{K}$ ). Middle: the derived quadrupole (temperature range  $\pm 35 \mu\text{K}$ ). Lower: the derived octopole (temperature range  $\pm 35 \mu\text{K}$ ). Cross and star signs indicate axes of the quadrupole and octopole, respectively, around which the angular momentum dispersion is maximized.

region is causing the anomalous behaviour, whilst the latter can establish whether foreground residuals could be responsible.

Table 18 and Fig. 21 present the results for the variance, skewness and kurtosis determined from the four CMB maps with the U73, CL58 and CL37 masks applied. Results are also computed for data within the ecliptic hemispheres surviving the U73 mask. The variance is low in all cases, with only small differences in significance observed for the different maps. Interestingly, the low variance seems to be localised in the northern ecliptic hemisphere. Conversely, anomalous values for the skewness and kurtosis are only apparent for the southern ecliptic hemisphere.

Since these results might be indicative of the presence of Galactic foreground residuals near the Galactic plane, we analyse the frequency dependence of the statistics as summarised in Table 19 and Fig. 22. The variance shows little frequency dependence for the considered masks and regions, whereas the skewness and kurtosis show a moderate frequency dependence when the U73 mask is applied, as also seen for the  $N$ -pdf in Sect. 4.2.



**Table 17.** Orientation of the low multipoles extracted from the different component separated CMB maps, obtained from maximizing the angular momentum dispersion. The second last column gives the absolute value of the scalar-product between the orientation vectors of the quadrupole and the octopole. In an isotropic universe, the latter is uniformly distributed on the interval  $[0, 1]$ . The last column gives the probability of such an alignment (or stronger than that) to occur.

Method	$(l, b)$ quadrupole $^\circ$	$(l, b)$ octopole $^\circ$	ang. distance $^\circ$	scalar-product	probability
C-R	(228.2, 60.3)	(246.1, 66.0)	9.80	0.985	0.019
NILC	(241.3, 77.3)	(241.7, 64.2)	13.1	0.974	0.033
SEVEM	(242.4, 73.8)	(245.6, 64.8)	9.08	0.988	0.016
SMICA	(238.5, 76.6)	(239.0, 64.3)	12.3	0.977	0.032

Cruz et al. (2011) found that a small region of the sky localised to both the ecliptic and Galactic south and near to the Galactic plane (their so-called gp10 region) exhibited particularly high variance. Thus, since the skewness is negative, we consider a prominent cold spot at  $(b = -8^\circ, l = 32^\circ)$ , partially masked by the Galactic plane. However, when masking the seven coldest pixels of the spot, the significance of the skewness and kurtosis drops only slightly, with lower tail probabilities of approximately 0.03 and 0.93 respectively. If the whole gp10 region ( $f_{\text{sky}} = 7\%$ ) is masked, the skewness and kurtosis drop drastically and have lower tail probabilities of approximately 0.30 and 0.50 respectively, whereas the variance is highly significant since none of the 1000 simulations has a variance below the data. In order to check the possible leakage of Galactic contamination due to the Gaussian smoothing applied to the low resolution data, we repeated our calculations for the Wiener filtered maps used in Sect. 5.1, but found little variation to the existing results. Therefore, it is unlikely that any leakage impacts the estimators.

The incompatibility of the observed variance with simulations based on a cosmological model that has been determined from the same data set might appear puzzling at first, but can be understood as follows. The map-based variance is dominated by contributions from large angular scales on the sky, whilst the cosmological parameter fits are relatively insensitive to these low-order  $\ell$ -modes, and are instead largely dominated by scales corresponding to  $\ell > 50$ . Thus, the best-fit spectrum in the context of a 6-parameter  $\Lambda$ CDM model can have a mismatch with the data on these scales, so that the corresponding simulations will not adequately capture the dearth of power at low- $\ell$ . The results presented here do indeed imply that the large-angular scale power is low relative to the fiducial sky model. In fact, when subtracting the quadrupole and octopole from both the data and simulations outside the U73 mask, the results are more consistent. In this case, the lower tail probabilities for the variance, skewness and kurtosis are 0.192, 0.637 and 0.792 respectively. This result was already found in Cruz et al. (2011). It is then plausible that the low multipole alignment could have the same cause as the anomalies considered here. However, when subtracting the quadrupole and octopole outside the CL58 mask, the lower tail probability for the low variance is 0.036, which remains rather low. The connection with the very low power in the ecliptic northern hemisphere also remains to be explored.

### 5.3. Hemispherical Asymmetry

In Eriksen et al. (2004a) and Hansen et al. (2004) it was discovered that the angular power spectrum of the first year *WMAP* data, when estimated locally at different positions on the sphere, appears not to be isotropic. In particular, the power spectrum calculated for a hemisphere centered at  $(\theta, \phi) = (110^\circ, 237^\circ)$  (in Galactic co-latitude and longitude) was larger than when

**Table 18.** Lower tail probability for the variance, skewness and kurtosis at  $N_{\text{side}} = 16$ , using different masks.

Mask	C-R	NILC	SEVEM	SMICA
Variance				
U73, $f_{\text{sky}} = 78\%$	0.019	0.017	0.014	0.019
CL58, $f_{\text{sky}} = 58\%$	0.004	0.003	0.003	0.003
CL37, $f_{\text{sky}} = 37\%$	0.028	0.017	0.018	0.016
Ecliptic North, $f_{\text{sky}} = 39\%$	0.001	0.001	0.001	0.002
Ecliptic South, $f_{\text{sky}} = 39\%$	0.464	0.479	0.454	0.490
Skewness				
U73, $f_{\text{sky}} = 78\%$	0.016	0.015	0.023	0.012
CL58, $f_{\text{sky}} = 58\%$	0.208	0.139	0.162	0.147
CL37, $f_{\text{sky}} = 37\%$	0.517	0.467	0.503	0.469
Ecliptic North, $f_{\text{sky}} = 39\%$	0.502	0.526	0.526	0.521
Ecliptic South, $f_{\text{sky}} = 39\%$	0.004	0.006	0.008	0.004
Kurtosis				
U73, $f_{\text{sky}} = 78\%$	0.972	0.973	0.966	0.982
CL58, $f_{\text{sky}} = 58\%$	0.630	0.726	0.711	0.711
CL37, $f_{\text{sky}} = 37\%$	0.069	0.135	0.130	0.124
Ecliptic North, $f_{\text{sky}} = 39\%$	0.094	0.229	0.196	0.245
Ecliptic South, $f_{\text{sky}} = 39\%$	0.933	0.916	0.886	0.948

calculated in the opposite hemisphere over the multipole range  $\ell = 2 - 40$ . Simultaneously, Park (2004) also presented evidence for the existence of such hemispherical asymmetry — in which a particular statistical measure is considered to change discontinuously between two hemispheres on the sky — with the application of Minkowski functionals to the *WMAP* data. Since the preferred direction of Eriksen et al. (2004a) lies close to the ecliptic plane, it was also demonstrated that the large-angular scale N-point correlation functions showed a difference in behaviour when computed on ecliptic hemispheres. Many studies have subsequently been undertaken focusing on hemispheres in the ecliptic coordinate system, with Schwarz et al. (2004) particularly emphasizing the connection. Hemispherical asymmetry has also been seen with other measures of non-Gaussianity (Eriksen et al. 2004c, 2005; Räth et al. 2007a).

Here we repeat the analysis of Eriksen et al. (2005) on the *Planck* component separated data, smoothed and then downgraded to  $N_{\text{side}} = 64$  as described in Sect. 2. As already noted in Sect. 4.3, the results for the low resolution maps are the most deviant relative to the MC simulations based on the *Planck* fiducial model.

The N-point correlation functions computed on the northern and southern hemispheres determined in the ecliptic coordinate frame and using the U73 mask are shown in Fig. 23. The correlation functions for the four *Planck* maps are very consistent, and the observed behaviour is in agreement with that seen in

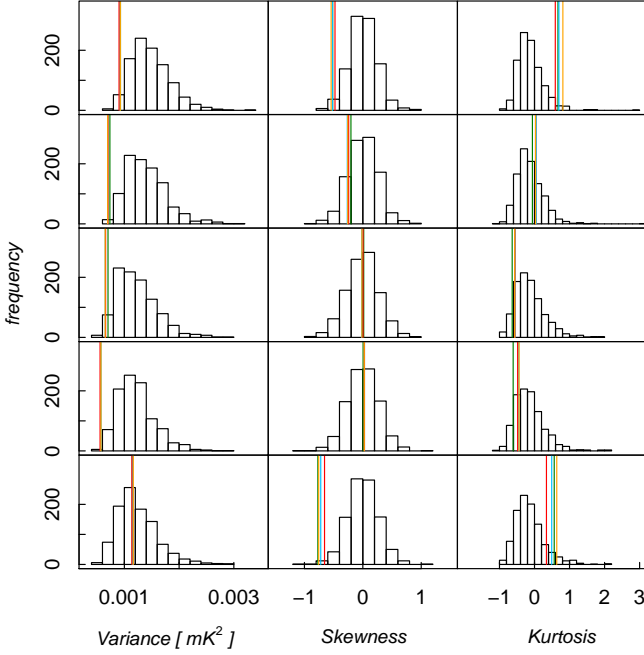


**Fig. 21.** Variance, skewness and kurtosis at  $N_{\text{side}} = 16$ , for the U73 mask, CL58, CL37, ecliptic North and ecliptic South (from top to bottom). The different lines represent the four component separation methods C-R (green), NILC (blue), SEVEM (red), and SMICA (orange).

**Table 19.** Frequency dependence of the lower tail probability for the variance skewness and kurtosis at  $N_{\text{side}} = 16$ , using different masks.

Mask	70 GHz	100 GHz	143 GHz	217 GHz
Variance				
U73, $f_{\text{sky}} = 78\%$	0.019	0.013	0.014	0.016
CL58, $f_{\text{sky}} = 58\%$	0.003	0.003	0.003	0.003
CL37, $f_{\text{sky}} = 37\%$	0.024	0.020	0.018	0.020
Ecliptic North, $f_{\text{sky}} = 39\%$	0.001	0.002	0.001	0.001
Ecliptic South, $f_{\text{sky}} = 39\%$	0.446	0.436	0.455	0.455
Skewness				
U73, $f_{\text{sky}} = 78\%$	0.045	0.016	0.024	0.015
CL58, $f_{\text{sky}} = 58\%$	0.254	0.205	0.162	0.157
CL37, $f_{\text{sky}} = 37\%$	0.503	0.471	0.468	0.515
Ecliptic North, $f_{\text{sky}} = 39\%$	0.505	0.447	0.541	0.352
Ecliptic South, $f_{\text{sky}} = 39\%$	0.015	0.006	0.009	0.006
Kurtosis				
U73, $f_{\text{sky}} = 78\%$	0.962	0.981	0.965	0.974
CL58, $f_{\text{sky}} = 58\%$	0.619	0.684	0.710	0.725
CL37, $f_{\text{sky}} = 37\%$	0.114	0.091	0.130	0.121
Ecliptic North, $f_{\text{sky}} = 39\%$	0.180	0.096	0.203	0.180
Ecliptic South, $f_{\text{sky}} = 39\%$	0.902	0.920	0.882	0.909

the *WMAP* data (Eriksen et al. 2004a). Specifically, the northern hemisphere correlation functions are featureless (both the three- and four-point functions lie very close to zero), whereas the southern hemisphere functions exhibit a level of structure that is in good agreement with the confidence regions computed from the Gaussian simulations.

The probabilities of obtaining a value for the  $\chi^2$  statistic for the *Planck* fiducial  $\Lambda$ CDM model at least as large as the ob-

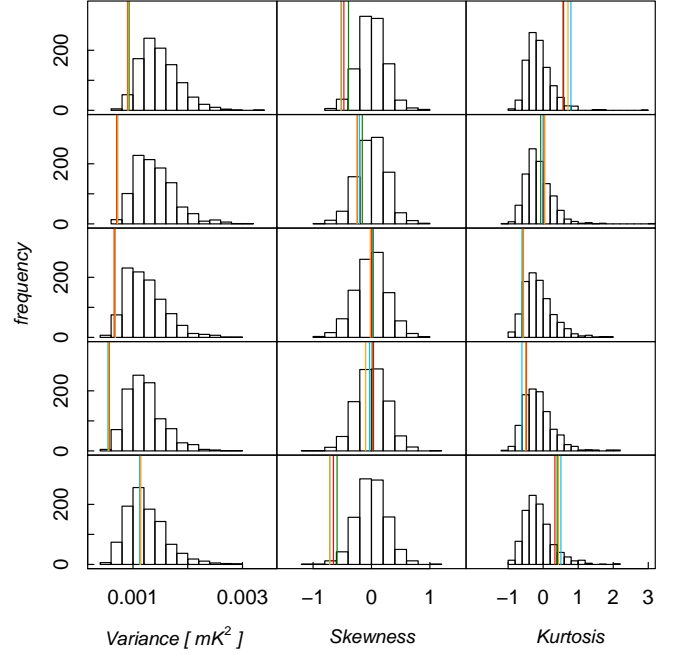


**Fig. 22.** Variance, skewness and kurtosis at  $N_{\text{side}} = 16$ , for the U73 mask, CL58, CL37, ecliptic North and ecliptic South (from top to bottom). The different lines represent the four considered frequencies, namely 70 GHz (green), 100 GHz (blue), 143 GHz (red), and 217 GHz (orange).

served values are presented in Table 20. The probabilities for the 3-point and 4-point functions in the northern Ecliptic hemisphere are especially large, and in the case of the pseudo-collapsed configuration all simulations yielded a larger than observed value of the  $\chi^2$ . Nominally, this value is even more remarkable than found with the *WMAP* data (Eriksen et al. 2004a), although to interpret it correctly one has to keep in mind that the analysis presented here is an example of *a posteriori* statistic. Specific choices have been made about the smoothing scale used for downgrading the data, and, in particular, for the reference direction that defines the hemispheres. This will tend to overestimate the significance of the results. Nevertheless, the observed properties of the *Planck* data are consistent with a remarkable lack of power in a direction towards the north ecliptic pole, consistent with the simpler one-point statistics presented in Sect. 5.2.

#### 5.4. Phase correlations

Previous studies using the methods of scaling indices and surrogates and based on the *WMAP* three-, five- and seven-year data (Räth et al. 2009, 2011; Rossmanith et al. 2012; Modest et al. 2013) showed significant evidence for intrinsic phase correlations at low  $\ell$  values in the CMB. The signal was demonstrated to be robust with respect to the *WMAP* data release, to the component separation methods and to the selected test statistics. In this section we apply these methods to the *Planck* component separated data sets.

The scaling index method represents one way to estimate the local scaling properties of a point set in an arbitrary  $d$ -dimensional embedding space. The technique provides the possibility to reveal local structural characteristics of a given point distribution. A number of analyses have used scaling indices to test the Gaussian nature and statistical isotropy of the CMB

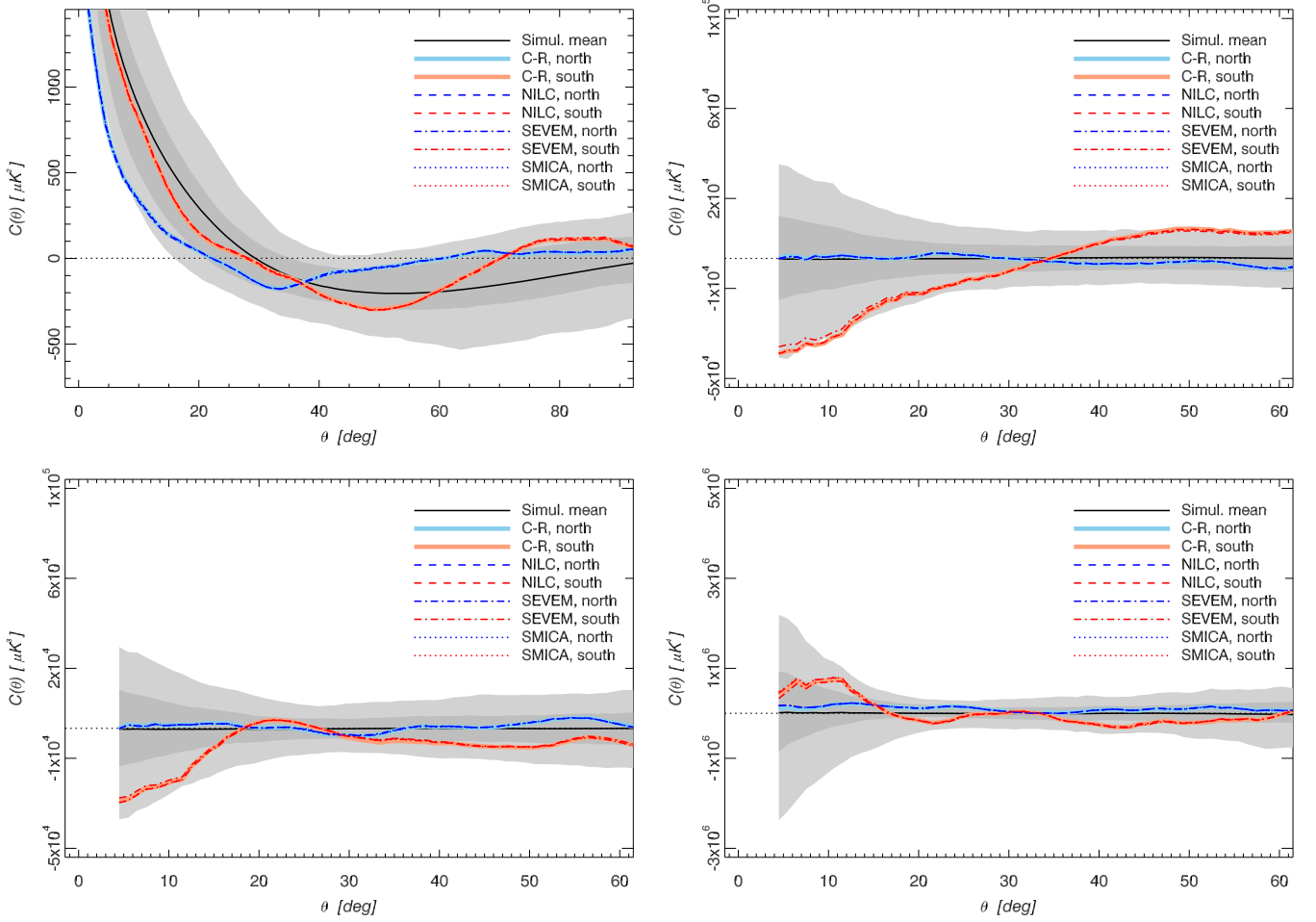


**Fig. 23.** The 2-point (upper left), pseudo-collapsed (upper right), equilateral 3-point (lower left) and rhombic 4-point (lower right) correlation functions ( $N_{\text{side}} = 64$ ). Correlation functions are shown for the analysis performed on northern (blue) and southern (red) hemispheres determined in the Ecliptic coordinate frame. The shaded dark and light grey bands indicate the 68% and 95% confidence regions, respectively.

as represented by the *WMAP* data (Räth et al. 2007a, 2009; Rossmanith et al. 2009a; Räth et al. 2011).

In general, the method is a mapping that calculates, for each member  $p_i, i = 1, \dots, N_{\text{pix}}$  of a point set  $P$ , a single value that depends on the spatial position of  $p_i$  relative to the group of other points in its neighborhood, in which the point under consideration is embedded. A three-dimensional point set  $P$  is generated for two-dimensional spherical CMB-data by transforming the temperature values  $T(\theta_i, \phi_i)$  of each pixel to a radial jitter around a sphere of radius  $R$  at the position of the pixel centre  $(\theta_i, \phi_i)$ . For obtaining scaling indices the local weighted cumulative point distribution which is defined as

$$\rho(\mathbf{p}_i, r) = \sum_{j=1}^{N_{\text{pix}}} s_r(d(\mathbf{p}_i, \mathbf{p}_j)) \quad (34)$$

with  $r$  describing the scaling range, while  $s_r$  and  $d$  denote a shaping function and a distance measure, respectively, is calculated first. The scaling index  $\alpha(\mathbf{p}_i, r)$  is then defined as the logarithmic derivative of  $\rho(\mathbf{p}_i, r)$  with respect to  $r$ :

$$\alpha(\mathbf{p}_i, r) = \frac{\partial \log \rho(\mathbf{p}_i, r)}{\partial \log r}. \quad (35)$$

Using a quadratic gaussian shaping function  $s_r(x) = e^{-\left(\frac{x}{r}\right)^2}$  and an isotropic euclidian norm  $d(\mathbf{p}_i, \mathbf{p}_j) = \|\mathbf{p}_i - \mathbf{p}_j\|$  as distance measure, one obtains the following analytic formula for the scaling indices

$$\alpha(\mathbf{p}_i, r) = \frac{\sum_{j=1}^{N_{\text{rmpix}}} 2\left(\frac{d_{ij}}{r}\right) e^{-\left(\frac{d_{ij}}{r}\right)^2}}{\sum_{j=1}^{N_{\text{rmpix}}} e^{-\left(\frac{d_{ij}}{r}\right)^2}}, \quad (36)$$

where we use the abbreviation  $d_{ij} \equiv d(\mathbf{p}_i, \mathbf{p}_j)$ . As should be clear from equation (36), the calculation of scaling indices depends on the scale parameter  $r$ . Ten scaling range parameters  $r_k = 0.05, 0.1, \dots, 0.5, k = 1, 2, \dots, 10$  in the notation of Räth et al. (2007a) are used in this analysis. In order to calculate scaling indices on large scales as in previous studies, we couple the  $r$ -jitter  $a$  to  $r_k$  via  $a = 0.5r_k$ . The mean  $\langle \alpha(r_k) \rangle$  and the standard deviation  $\sigma_{\alpha(r_k)}$  derived from the full sky and from a set of 768 rotated hemispheres are used to test for non-Gaussianity and deviations from statistical isotropy.

In order to quantify the significance of the scaling index results, and focus the study on the phase properties of the observed CMB sky, we utilize the method of surrogate maps (Räth et al. 2009). Such a technique offers the unique possibility to

**Table 20.** Probabilities of obtaining values of the  $\chi^2$  statistic for the *Planck* fiducial model at least as large as the observed values of the statistic for the *Planck* maps with resolution parameter  $N_{\text{side}} = 64$  estimated using the C-R, NILC, SEVEM and SMICA methods.

	C-R	NILC	SEVEM	SMICA
Two-point function				
Northern Ecliptic . . . . .	0.935	0.924	0.927	0.932
Southern Ecliptic . . . . .	0.633	0.599	0.639	0.592
Pseudo-collapsed three-point function				
Northern Ecliptic . . . . .	1.000	1.000	1.000	1.000
Southern Ecliptic . . . . .	0.349	0.310	0.381	0.301
Equilateral three-point function				
Northern Ecliptic . . . . .	0.996	0.999	0.999	0.999
Southern Ecliptic . . . . .	0.627	0.644	0.678	0.656
Rhombic four-point function				
Northern Ecliptic . . . . .	0.999	0.999	0.999	0.999
Southern Ecliptic . . . . .	0.559	0.548	0.574	0.553

test for scale-dependent non-Gaussianity and deviations from isotropy in a completely model-independent (“blind”) way. This self-consistency of the surrogate approach suppresses the sensitivity of the null tests to the assumed fiducial power spectrum. This is particularly pertinent given the potential mismatch of the *Planck* data to the fiducial spectrum on large-angular scales (Planck Collaboration XV 2013). The statistical properties of a Gaussian random field on the sphere can be fully described by its two-point correlation function (or power spectrum) and exhibit Fourier phases that are independent and identically distributed (i.i.d.) and follow a uniform distribution in the interval  $[-\pi, \pi]$ . Thus, demonstrating the existence of Fourier phase correlations in CMB maps could indicate the presence of non-Gaussianities in the primordial density fluctuations. The possible presence of phase correlations is tested using the method of surrogates.

However, the Gaussianity of the temperature distribution and the randomness of the set of Fourier phases of the map to be studied are a necessary pre-requisite for the application of the surrogate-generating algorithm. Therefore the following pre-processing steps are applied to generate a zero order surrogate map. First, the maps are remapped on to a Gaussian distribution in a rank-ordered way. Then we ensure the randomness of the set of Fourier phases by making a rank-ordered remapping of the phases on to a set of uniformly distributed ones. These two preprocessing steps only have marginal influence on the maps. Now, the set of surrogates to be used for assessing the statistical properties of the data sets can be generated by shuffling the phases in the space of the spherical harmonics while exactly preserving the modulus of the  $a_{\ell m}$ . Moreover, by introducing a two-step shuffling scheme for previously specified  $\ell$ -ranges, a scale-dependent analysis is made possible. It is worth noticing that while in all surrogate maps the modulus of the  $a_{\ell m}$  is exactly preserved, null tests involving a comparison to an assumed fiducial power spectrum only preserve the  $C_\ell$  values, which are average values of the  $|a_{\ell m}|$  when summed over  $m$ . Thus, the linear properties of the surrogate maps are more tightly constrained, and specifically kept constant, than in tests involving simulated maps generated on the basis of the  $C_\ell$ s.

So-called first and second order surrogate maps are then obtained as follows. We initially generate a first order surrogate

map, in which any phase correlations for the scales that are not of interest are randomized by shuffling its phases  $\phi_{\ell m}$  for  $\ell \notin \Delta\ell = [\ell_{\min}, \ell_{\max}]$ ,  $0 < m \leq \ell$ . In a second step,  $N$  ( $N = 1000$  throughout these investigations) realizations of second order surrogate maps are generated from the first order surrogate map, in which the remaining phases  $\phi_{\ell m}$  with  $\ell \in \Delta\ell$ ,  $0 < m \leq \ell$  are shuffled, while the previously randomized phases for the other scales are preserved. The generation of surrogates is always performed using the maps with the highest resolution, i.e.,  $N_{\text{side}} = 2048$ . Given the evidence for anomalies on the largest angular scales, and to ensure consistency with the previous *WMAP* analyses, we perform dedicated scale-dependent tests for the scales defined by  $\Delta\ell = [2, 20]$ .

Since the methodology in its simplest form requires the orthonormality of the set of basis functions  $Y_{\ell m}$ , we apply the method to the full sky foreground-cleaned maps as obtained after component separation with Commander-Ruler, NILC, SEVEM and SMICA. For the selected  $\ell$ -interval  $\Delta\ell = [2, 20]$ , the generation of the first order surrogate map removes the phase signature of the small scale residuals in the data and can be interpreted as a form of inpainting procedure for small masked patches in the Galactic plane. The differences between the first and second order surrogates are quantified by the  $\sigma$ -normalized deviation  $S$

$$S(Y) = \frac{Y_{\text{surro1}} - \langle Y_{\text{surro2}} \rangle}{\sigma_{Y_{\text{surro2}}}} \quad (37)$$

with,  $Y = \langle \alpha(r_k) \rangle, \sigma_{\alpha(r_k)}, \chi^2$ . Here,  $\chi^2$  represents either a diagonal combination of the the mean  $\langle \alpha(r_k) \rangle$  and standard deviation  $\sigma_{\alpha(r_k)}$  at a certain scale  $r_k$  or for the full scale-independent  $\chi^2$  statistics

$$\chi^2 = (\mathbf{M} - \langle \mathbf{M} \rangle)^T \mathbf{C}^{-1} (\mathbf{M} - \langle \mathbf{M} \rangle), \quad (38)$$

where the test statistics to be combined are comprised in the vector  $\mathbf{M}$  and  $\mathbf{C}$  is obtained by cross correlating the elements of  $\mathbf{M}$ . With the mean and the standard deviation as input for  $\mathbf{M}$  we obtain  $\chi^2_{\langle \alpha \rangle}$  and  $\chi^2_{\sigma_\alpha}$  statistics with  $\mathbf{M}^T = (\langle \alpha(r_1) \rangle, \dots, \langle \alpha(r_{10}) \rangle)$  and  $\mathbf{M}^T = (\sigma_{\alpha(r_1)}, \dots, \sigma_{\alpha(r_{10})})$  respectively.

Fig. 24 shows the  $S(\chi^2)$  values for the set of rotated hemispheres for the SMICA map. Each pixel of the full sky map with a HEALPix resolution of  $N_{\text{side}} = 8$  specifies one of the 768 S-values for a rotated hemisphere, where the pixel position indicates the orientation of the z-axis of the rotated coordinate system. We detect pronounced signatures for both non-Gaussianities and anisotropies. The results are consistent for Commander-Ruler, NILC, SEVEM and SMICA.

In Fig. 25, the deviations  $S(Y)$  are displayed for the mean and standard deviation. We only show the results for the SMICA map. The other three maps yield very similar results. For all four maps the values for  $S(\langle \alpha \rangle)$  extend far beyond 3 for  $r = 0.2 - -0.25$  when rotated hemispheres are considered separately. Since the effect in the separate hemispheres goes in opposing directions, no signal is observed for the full sky. The results for the scale-independent  $\chi^2$  statistics are summarized in Table 21. The results suggest a highly significant detection of both non-Gaussianities and anisotropies in the *Planck* data, consistent with those obtained previously with *WMAP* data (for comparison see Modest et al. 2013).

We have also investigated whether the significance of the results depends on the choice of  $\ell_{\min}$  and  $\ell_{\max}$ . In particular, we have extended the range of interest to  $\ell_{\max} = 30$ , and then considered three sub-intervals,  $\Delta\ell = [2, 10]$ ,  $\Delta\ell = [11, 20]$  and

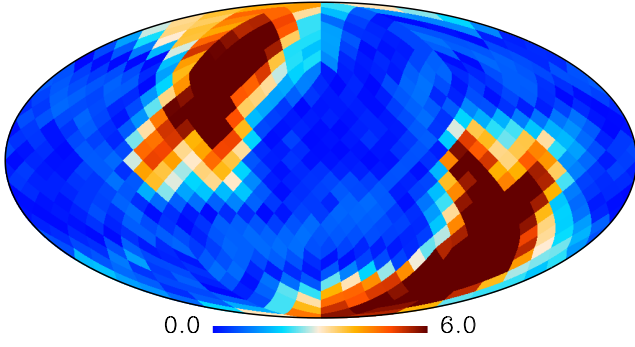


**Fig. 24.** Deviations  $S(\chi^2)$  of the rotated hemispheres derived from a combination of the mean and the standard deviation of the scaling indices for the scale  $r_5$  determined from the SMICA map.

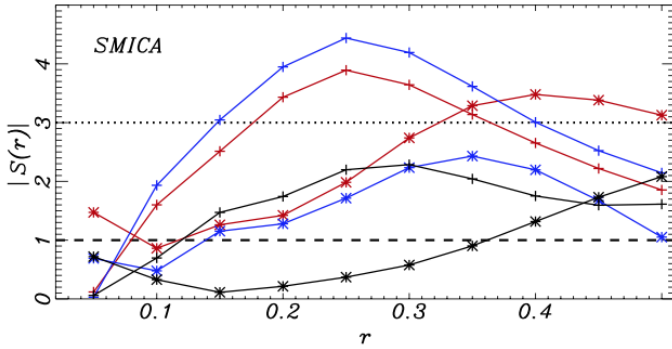


**Fig. 25.** Deviations  $|S(r)|$  for the SMICA map as a function of the scale parameter  $r$  for the full sky (black) and upper (red) and lower (blue) rotated hemispheres. The plus signs denote the results for the mean  $\langle\alpha(r_k)\rangle$ , the star-signs represent the standard deviation  $\sigma_{\alpha(r_k)}$ . The dashed (dotted) line indicates the 1 (3)  $\sigma$  significance interval.

**Table 21.** Deviations  $S$  and empirical probabilities  $p$  for the scale-independent  $\chi^2$ -statistics derived from the C-R, NILC, SEVEM and SMICA maps.

	Full Sky ( $S/\%$ )	Upper Hemisphere ( $S/\%$ )	Lower Hemisphere ( $S/\%$ )
C-R, $\chi^2_{(\alpha)}$ . . . . .	0.86 / 82.6	4.21 / 99.7	3.18 / 99.0
C-R, $\chi^2_{\sigma_\alpha}$ . . . . .	0.88 / 85.2	3.94 / 99.5	3.10 / 99.2
NILC, $\chi^2_{(\alpha)}$ . . . . .	0.86 / 81.8	3.74 / 99.6	4.41 / >99.9
NILC, $\chi^2_{\sigma_\alpha}$ . . . . .	0.79 / 78.8	3.69 / 99.6	4.49 / >99.9
SEVEM, $\chi^2_{(\alpha)}$ . . . . .	0.00 / 58.0	3.22 / 99.3	5.02 / >99.9
SEVEM, $\chi^2_{\sigma_\alpha}$ . . . . .	0.05 / 60.8	3.20 / 99.0	5.11 / 99.9
SMICA, $\chi^2_{(\alpha)}$ . . . . .	0.75 / 80.1	3.80 / 99.8	4.70 / 99.8
SMICA, $\chi^2_{\sigma_\alpha}$ . . . . .	0.01 / 54.4	3.64 / 99.3	4.81 / >99.9

$\Delta\ell = [21, 30]$ . Over the full range, similar results are found to those from  $\Delta\ell = [2, 20]$ , but at lower significance. This suggests that the inclusion of the phases in the interval  $\Delta\ell = [21, 30]$  dilutes the signal, because there are no phase correlations in this  $\ell$ -range. This is corroborated by the fact that the first and sec-

ond order surrogates generated specifically for this sub-interval cannot be distinguished. The results for the interval  $\Delta\ell = [2, 10]$  are quite consistent with those over  $\Delta\ell = [2, 20]$ , whereas for  $\Delta\ell = [11, 20]$  we find that the signature in the northern ecliptic hemisphere nearly vanishes. Conversely, in the southern ecliptic hemisphere, on the other hand, the  $S$ -signal persists – especially for regions covering the Cold Spot. It thus appears that the lowest  $\ell$ -range is predominantly responsible for the detected hemispherical asymmetries detected in the spectrum of scaling indices, whilst the intermediate interval considered may have an association with the Cold Spot. It is certainly the case that scale-dependence is seen in the nature of the phase correlations present in the data.

Since both, the modulus of the  $a_{\ell m}$ s for all  $\ell$ s and the phases  $\phi_{\ell m}$  for  $\ell \notin \Delta\ell$  are exactly the same in the first and second order surrogates, one must infer that the pattern of hemispherical asymmetry in the  $S$ -maps can solely be attributed to phase correlations in the interval  $\Delta\ell$ . Thus, the analysis involving surrogate maps reveals that there *are* phase correlations at low  $\ell$ .

### 5.5. Dipolar asymmetry

In previous sections, we have seen evidence for a break in isotropy related to the discontinuous distribution of power in hemispheres on the sky. Bennett et al. (2011) distinguishes between such an asymmetry and one where the CMB signal is modulated across the sky by a dipolar term. Studies of such a dipolar asymmetry have been motivated by the phenomenological proposal of Gordon et al. (2005) that the power asymmetry could be described in terms of a multiplicative dipole modulation model. In addition, relativistic Doppler boosting due to our motion with respect to the CMB rest frame is expected to induce a dipolar modulation aligned with the CMB dipole at the  $O(10^{-3})$  level; a statistically significant detection of this effect by *Planck* is presented by Planck Collaboration XXVII (2013).

#### 5.5.1. Power asymmetry

In their analysis of the 5-year *WMAP* data, (Hansen et al. 2009) specifically searched for the dipolar modulation of power on the sky. In particular, a simple test was performed in which the power spectrum on discs was computed and binned into independent blocks of 100 multipoles from  $\ell = 2$  to  $\ell = 600$ , then each block fitted for a dipolar asymmetry in the power distribution. The 6  $\ell$ -ranges considered showed evidence of a consistent dipole direction, yet, from a set of 10000 simulations, none showed a similarly strong asymmetry. A further extension of the analysis introduced a model selection procedure taking into account the statistical penalty for introducing an asymmetric model with additional parameters (direction of asymmetry, amplitude of asymmetry and asymmetric multipole ranges). Even in this case, the asymmetry was found to be highly significant for the whole range  $\ell = 2 - 600$ .

However, such a procedure is highly expensive in terms of CPU-time. Given the higher sensitivity and angular resolution of the *Planck* data, we have therefore elected to focus on the simpler disc-based test, thus allowing us to probe further into a previously unexplored  $\ell$ -range. This should at least in part answer any *a posteriori* criticisms of the study. Since the analysis is power-spectrum based, the half-ring data sets for the different CMB estimators are used. The approach is as follows:

1. The half-ring temperature maps are multiplied with an appropriate Galactic and point source mask.



2. The cross power spectrum between the two halves is estimated locally using the MASTER approach (Hivon et al. 2002) for 768 discs of diameter  $22.5^\circ$  degrees centered on the pixel centers of all the pixels of an  $N_{\text{side}} = 8$  HEALPix map.
3. We apply the same procedure to the set of 500 simulated maps of CMB and noise.
4. The 768 local spectra are binned into blocks of about 100 multipoles as in Hansen et al. (2009). There are not exactly 100 multipoles in each block, as the spectra have been initially estimated in 16-multipole blocks.
5. For each 100-multipole block and each disc, the mean power from simulations is subtracted and the result is divided by the standard deviation. Dividing the spectra by the local standard deviation avoids the problem that directions close to the Galaxy, where the Galactic mask increases the variance, can dominate the statistics due to large fluctuations.
6. Each 100-multipole block now has an associated map at  $N_{\text{side}} = 8$ , where each pixel corresponds to the normalised power spectrum estimated on the disc centered on that direction.
7. Spherical harmonic transforms are computed for each of the maps in order to obtain the dipoles and the dipole directions  $(\theta, \phi)$  of the power asymmetry for each 100-multipole block. The alignment of this direction between the different multipole blocks is then a measure of the power spectrum asymmetry. Despite the mask-induced correlations between adjacent multipoles, the power spectra estimated in 100-multipole blocks should be independent and the dipole directions of an isotropic field should be random.

In order to assess the significance of the asymmetry, one has to find out whether the distribution of dipole directions for the different scales are as random and independent as in the simulated maps. For this purpose, we define a dispersion angle,  $\theta_{\text{mean}}$ , which is the mean angle between all possible combinations of 100-multipole dipole directions up to a given  $\ell_{\text{max}}$ . We calculate  $\theta_{\text{mean}}(\ell_{\text{max}} = 1500)$  for the data and compare it to the simulations.

Table 22 presents a summary of the power asymmetry results from the *Planck* data processed by the four foreground cleaning methods — Commander-Ruler, NILC, SEVEM and SMICA — computed on the U73 mask. To illustrate the effect of the mask in the analysis, we also show the result obtained using the SMICA data with a smaller mask with  $f_{\text{sky}} = 88\%$  (the CS-SMICA89 mask which corresponds to the confidence mask for that method – see Planck Collaboration XII 2013). For comparison, we have also included the latest *WMAP* 9-year result computed with their KQ85 mask.

From Table 22 we see that the result from the mask with larger sky coverage, the SMICA data with the CS-SMICA89 mask, has the highest power asymmetry, the data dispersion angle of the first 15 100-multipole dipole directions being lower than all the 500 simulations. The significance decreases to about 99.2% confidence level, however, for the U73 mask with a smaller sky coverage, except for the case of Commander-Ruler, which has an even lower significance. Moreover, the dispersion angles among the first 15 100-multipole dipole directions for the four methods are consistent. The comparison between the simulations and the data dispersion angles up to  $\ell_{\text{max}} = 1500$  is shown in Fig. 26.

In Fig. 27 we show the dipole directions of the 15 initial 100-multipole bins for the SMICA map with the CS-SMICA89 mask, as well as the 6 first 100-multipole bins for *WMAP*9 data with the KQ85 mask (squares). We see that the direction of the first

**Table 22.** Summary of the power dipole directions on the sky, up to  $\ell_{\text{max}} = 1500$ , as determined from maps of the power spectrum estimated from 768  $22.5^\circ$  radius discs and averaged over  $\Delta\ell = 100$  bins. The significance of the power asymmetry, shown in the last column, is quantified by the fraction of simulations that have smaller clustering of the dipole directions than the data. For the *Planck* analysis we used the 500 FFP6 simulations, while for *WMAP* we used 10000 Gaussian simulations.

Method	Mask	(l,b) [°]	$\theta_{\text{mean}}^d$ [°]	Frac. $\theta_{\text{mean}}^{\text{sim}} < \theta_{\text{mean}}^d$
C-R	U73	(231,−5)	67.8	11/500
NILC	U73	(223,−1)	66.1	4/500
SEVEM	U73	(224,2)	66.6	4/500
SMICA	U73	(225,1)	66.2	4/500
<i>WMAP</i> 9	<i>WMAP</i> 9 KQ85	(226,−27)	33.2	27/10000
SMICA	CS-SMICA89	(224,0)	55.8	0/500

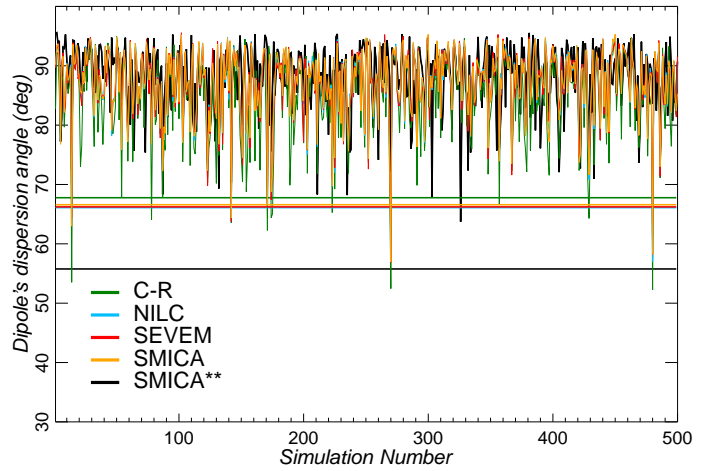


**Fig. 26.** Dispersion angles of the power spectra dipole directions, the mean of the differences of the dipole direction angles, up to  $\ell_{\text{max}} = 1500$ , of the 500 FFP6 simulations compared to the *Planck* data with different foreground cleaning methods. All analyses, except SMICA\*\*, are performed with the U73 mask. The SMICA\*\* case is for SMICA data with the CS-SMICA89 mask.

6 dipoles are similar to the directions found in the *WMAP* data. The preferred directions for *WMAP*9 and *Planck* over the range  $\ell = 2 - 600$  are indicated, together with the *Planck* direction for the total range  $\ell = 2 - 1500$ . Finally, the direction of the dipole modulation described in Sect. 5.5.2 is also included. Similar behaviour is seen for all of the *Planck* foreground cleaned maps and for the U73 mask, although the scatter between the dipole directions increases with increasing sky cut.

It should be apparent that the asymmetry direction from the largest to the smallest angular scales are in general tightly clustered around the same direction as found for *WMAP*. However, with the *Planck* data a second preferred direction is also seen which is aligned with the CMB dipole direction. This result is consistent with the findings of Planck Collaboration XXVII (2013), who reports a statistically significant detection of Doppler boosting aligned with the CMB dipole at small angular scales.

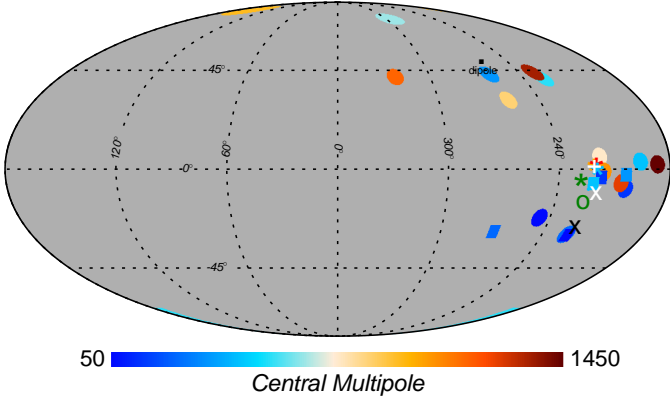


**Fig. 27.** Dipole directions for 100-multipole bins of the local power spectrum distribution from  $\ell = 2 - 1500$  in the SMICA map with the CS-SMICA89 mask applied. We also show the total direction for  $\ell_{\text{max}} = 600$  for WMAP9 (black X) and SMICA (white X) as well as for  $\ell_{\text{max}} = 1500$  for SMICA (white big +). The stars with different colors correspond to C-R (green), NILC (deepskyblue), SEVEM (red) and SMICA (orange) with the U73 mask. The best fit dipole modulation direction from Sect. 5.5.2 is indicated by the white open circle.

In Fig. 28 we show the  $C_\ell$  computed in discs of diameter  $90^\circ$  centered on the preferred asymmetry dipole direction for  $\ell = 2 - 1500$  as well as the opposite direction. We can clearly see that one spectrum lies systematically above the other over the full multipole range, but in particular for the lowest multipoles. Such an asymmetry is not seen at the same level of significance when the spectra are computed for discs centred on the cosmological dipole direction.

### 5.5.2. Dipole modulation

In Sect. 5.5.1 it was shown that the previously reported power asymmetry is visible at all multipoles probed by *Planck* with a fairly consistent preferred axis across angular scales. No explicit parametric model was assumed in the analysis. In this section, however, we revisit the phenomenological model due to Gordon et al. (2005) considering only large angular scales, who proposed that the power asymmetry could be described in terms of a multiplicative dipole modulation model of the form  $\mathbf{d} = (1 + A \mathbf{p} \cdot \mathbf{n}) \mathbf{s}_{\text{iso}} + \mathbf{n} \equiv \mathbf{M} \mathbf{s}_{\text{iso}} + \mathbf{n}$ , where  $A$  is the dipole amplitude,  $\mathbf{p}$  is the dipole direction,  $\mathbf{n}$  denotes instrumental noise, and  $\mathbf{s}_{\text{iso}}$  is an underlying isotropic CMB field. Both  $\mathbf{s}_{\text{iso}}$  and  $\mathbf{n}$  are assumed to be Gaussian random fields with covariance matrices  $\mathbf{S}$  and  $\mathbf{N}$ , respectively. Since  $\mathbf{s}_{\text{iso}}$  is assumed to be isotropic, its covariance may be fully specified by some angular power spectrum  $C_{\ell, \text{iso}}$ .

In the following we present the results from a direct likelihood analysis of this model, similar to those described by Eriksen et al. (2007a); Hoftuft et al. (2009) for the 3- and 5-year WMAP data, respectively. Since this method requires matrix inversions and determinant evaluations, the computational expense scales as  $O(N_{\text{pix}})$ , and it is therefore feasible only at low resolutions. Specifically, we consider maps downgraded to a HEALPix pixel resolution of  $N_{\text{pix}} = 32$ , smoothed to angular resolutions ranging from  $5$  to  $10^\circ$ , ensuring sufficient bandwidth limitation at this pixelization. All four *Planck* CMB solutions are included in the analysis; however, note that the Galactic plane is handled differently in the four approaches. Specifically, for

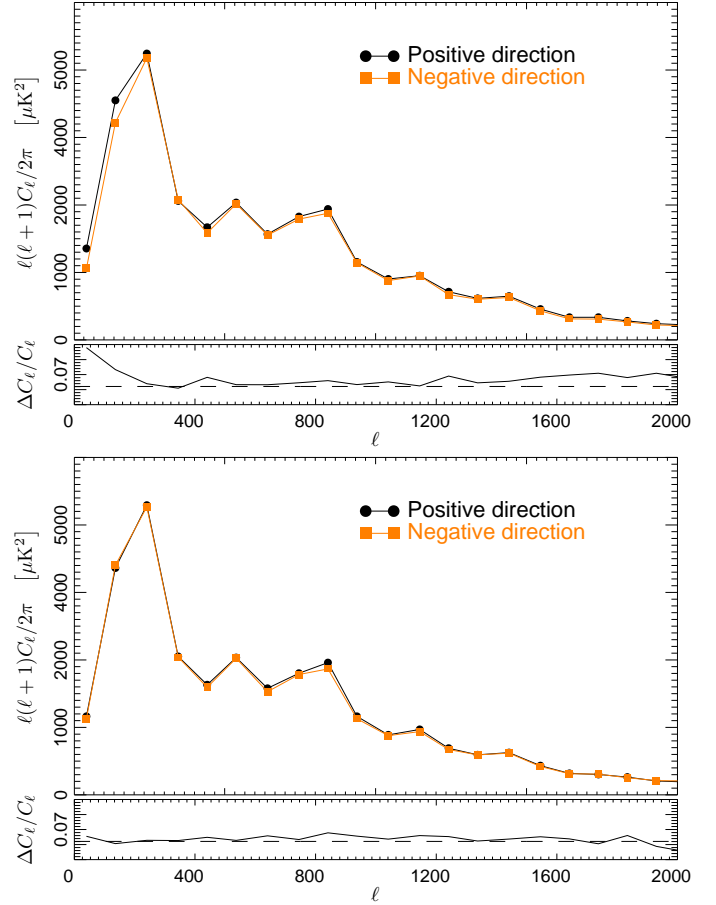


**Fig. 28.** *Top:* The power spectra calculated on discs with diameter  $90^\circ$  for the range  $\ell = 2 - 1500$  in the direction of maximal asymmetry and its opposite. *Bottom:* The equivalent plot for the direction defined by the cosmological dipole. The lower panels indicate the normalized difference of the spectra from opposing directions.

the Commander map the region inside the corresponding analysis mask has been replaced with a Gaussian constrained realization, eliminating the possibility of bright Galactic residuals to leak outside the mask during degradation (Planck Collaboration XV 2013); for SMICA and NILC a smaller region is replaced with a Wiener filter; while for SEVEM no special precautions are taken.

After degrading each map to the appropriate resolution, we add random uniform Gaussian noise of  $1 \mu\text{K}$  rms to each pixel to regularize the covariance matrix. All pixels inside the U73 mask are excluded, and we adopt the difference maps between the raw *Planck* LFI 30 GHz and HFI 353 GHz maps and the SMICA CMB solution as two foreground templates, tracing low- and high-frequency foregrounds, respectively. We marginalize over these Galactic foreground templates,  $\mathbf{f}$ , as well as four monopole and dipole templates, by adding corresponding term of the form  $\alpha \mathbf{f} \mathbf{f}^T$  to the total data covariance matrix, where  $\alpha$  is set to a numerically large value.

Before writing down the likelihood for  $A$  and  $\mathbf{p}$ , a choice has to be made for the power spectrum,  $C_{\ell, \text{iso}}$ . We follow Eriksen et al. (2007a), and adopt a simple two-parameter amplitude-tilt parameter model on the form  $C_{\ell, \text{iso}} = q (\ell/\ell_{\text{pivot}})^n C_{\ell, \text{fid}}$  for this purpose, where the fiducial spectrum,  $C_{\ell, \text{fid}}$ , is the best-fit *Planck* spectrum. The full model therefore includes five free parameters,

**Table 23.** Summary of dipole modulation likelihood results as a function of scale for all four *Planck* CMB solutions.

Data set	FWHM [°]	A	( <i>l</i> , <i>b</i> ) [°]	$\Delta \ln \mathcal{L}$	Significance
Commander	5	$0.078^{+0.020}_{-0.021}$	$(227, -15) \pm 19$	8.8	$3.5\sigma$
NILC	5	$0.069^{+0.020}_{-0.021}$	$(226, -16) \pm 22$	7.1	$3.0\sigma$
SEVEM	5	$0.066^{+0.021}_{-0.021}$	$(227, -16) \pm 24$	6.7	$2.9\sigma$
SMICA	5	$0.065^{+0.021}_{-0.021}$	$(226, -17) \pm 24$	6.6	$2.9\sigma$
WMAP5 ILC	4.5	$0.072 \pm 0.022$	$(224, -22) \pm 24$	7.3	$3.3\sigma$
Commander	6	$0.076^{+0.024}_{-0.025}$	$(223, -16) \pm 25$	6.4	$2.8\sigma$
NILC	6	$0.062^{+0.025}_{-0.026}$	$(223, -19) \pm 38$	4.7	$2.3\sigma$
SEVEM	6	$0.060^{+0.025}_{-0.026}$	$(225, -19) \pm 40$	4.6	$2.2\sigma$
SMICA	6	$0.058^{+0.025}_{-0.027}$	$(223, -21) \pm 43$	4.2	$2.1\sigma$
Commander	7	$0.062^{+0.028}_{-0.030}$	$(223, -8) \pm 45$	4.0	$2.0\sigma$
NILC	7	$0.055^{+0.029}_{-0.030}$	$(225, -10) \pm 53$	3.4	$1.7\sigma$
SEVEM	7	$0.055^{+0.029}_{-0.030}$	$(226, -10) \pm 54$	3.3	$1.7\sigma$
SMICA	7	$0.048^{+0.029}_{-0.029}$	$(226, -11) \pm 58$	2.8	$1.5\sigma$
Commander	8	$0.043^{+0.032}_{-0.029}$	$(218, -15) \pm 62$	2.1	$1.2\sigma$
NILC	8	$0.049^{+0.032}_{-0.031}$	$(223, -16) \pm 59$	2.5	$1.4\sigma$
SEVEM	8	$0.050^{+0.032}_{-0.031}$	$(223, -15) \pm 60$	2.5	$1.4\sigma$
SMICA	8	$0.041^{+0.032}_{-0.029}$	$(225, -16) \pm 63$	2.0	$1.1\sigma$
Commander	9	$0.068^{+0.035}_{-0.037}$	$(210, -24) \pm 52$	3.3	$1.7\sigma$
NILC	9	$0.076^{+0.035}_{-0.037}$	$(216, -25) \pm 45$	3.9	$1.9\sigma$
SEVEM	9	$0.078^{+0.035}_{-0.037}$	$(215, -24) \pm 43$	4.0	$2.0\sigma$
SMICA	9	$0.070^{+0.035}_{-0.037}$	$(216, -25) \pm 50$	3.4	$1.8\sigma$
WMAP3 ILC	9	0.114	$(225, -27)$	6.1	$2.8\sigma$
Commander	10	$0.092^{+0.037}_{-0.040}$	$(215, -29) \pm 38$	4.5	$2.2\sigma$
NILC	10	$0.098^{+0.037}_{-0.039}$	$(217, -29) \pm 33$	5.0	$2.3\sigma$
SEVEM	10	$0.103^{+0.037}_{-0.039}$	$(217, -28) \pm 30$	5.4	$2.5\sigma$
SMICA	10	$0.094^{+0.037}_{-0.040}$	$(218, -29) \pm 37$	4.6	$2.2\sigma$

namely three dipole parameters and two power spectrum parameters.

Taking advantage of the fact that both the signal and noise are assumed Gaussian, the exact likelihood may be written down in a convenient closed form,

$$\mathcal{L}(A, \mathbf{p}, q, n) \propto \frac{e^{-\frac{1}{2} \mathbf{d}^T (\mathbf{M}^T \mathbf{S} \mathbf{M} + \mathbf{N} + \alpha \sum_i \mathbf{f}_i \mathbf{f}_i^T)^{-1} \mathbf{d}}}{\sqrt{|\mathbf{M}^T \mathbf{S} \mathbf{M} + \mathbf{N} + \alpha \sum_i \mathbf{f}_i \mathbf{f}_i^T|}}. \quad (39)$$

This expression forms the basis of all calculations presented in the following.

Due to the high computational expense associated with these evaluations, we do not compute the full joint five-parameter model in this analysis, only conditionals of it. However, we iterate once in a Gibbs-sampling like approach, by maximizing each conditional to obtain an approximation to the full maximum-likelihood solution. That is, we first map out the dipole likelihood for the  $5^\circ$  FWHM case, fixing the power spectrum at the fiducial spectrum,  $\mathcal{L}(A, \mathbf{p}|q = 1, n = 0)$ , and locate the maximum-likelihood dipole parameters. Then we map out the corresponding power spectrum conditional,  $\mathcal{L}(q, n|A_{ml}, \mathbf{p}_{ml})$ . Finally, we update the dipole likelihood with these power spectrum parameters, and evaluate the final results. Note that the

power spectrum and dipole modulation parameters are only weakly correlated, and this procedure is therefore close to optimal. Further, the approach is also conservative, in the sense that it will always underestimate the significance of the dipole modulation model; the derived maximum-likelihood value will always lie slightly below the true maximum-likelihood point.

The results from these calculations are summarized in Table 23, listing results for all four *Planck* CMB maps at angular scales between  $5$  and  $10^\circ$  FWHM. For easy reference, we also list the results from the corresponding 3- and 5-year *WMAP* analyses (Eriksen et al. 2007a; Hoftuft et al. 2009). Note that the former was performed at a HEALPix resolution of  $N_{\text{side}} = 16$  and the latter at an angular resolution of  $4.5^\circ$  FWHM.

Fig. 30 shows marginals for  $A$ ,  $q$  and  $n$ , as derived from the Commander CMB solution for all smoothing scales. At least two interesting points can be seen here. First, while there is clearly significant scatter in the derived dipole modulation amplitude for different smoothing scales, as originally pointed out by Hanson & Lewis (2009), all curves appear to be consistent with a single value of  $A \sim 0.07$ . No other single value fits all scales equally well. Second, it is interesting to note that the low- $\ell$  power spectrum derived here is consistent, but not without some tension, with the fiducial spectrum,  $(q, n) = (1, 0)$ , around  $1.5 - 2\sigma$ . In



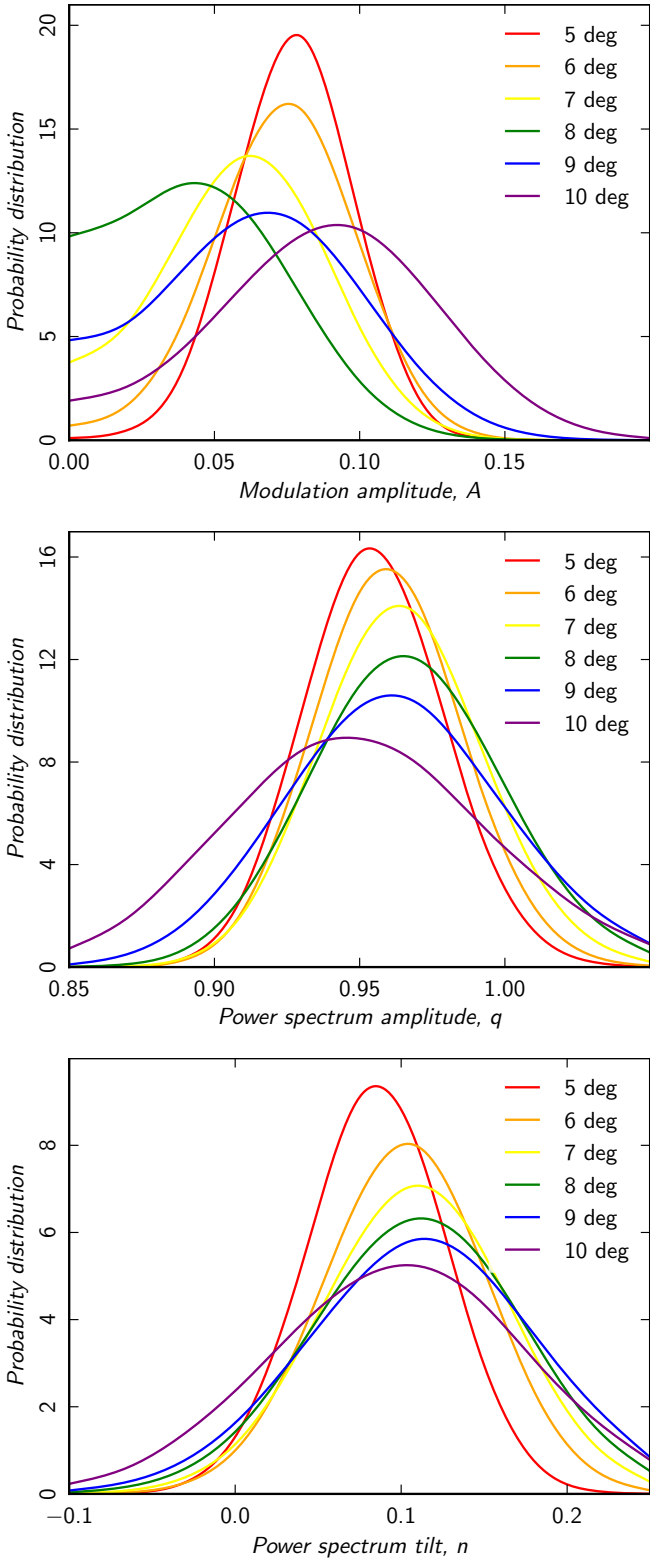


**Fig. 29.** Marginal dipole modulation amplitude (top), power spectrum amplitude (middle) and power spectrum tilt (bottom) probability distributions as a function of smoothing scale, shown for the Commander CMB solution.

particular, there appears to be a slight trend toward a steeper and positive spectral index as more weight is put on the larger scales, a result already noted by *COBE*-DMR. The same conclu-

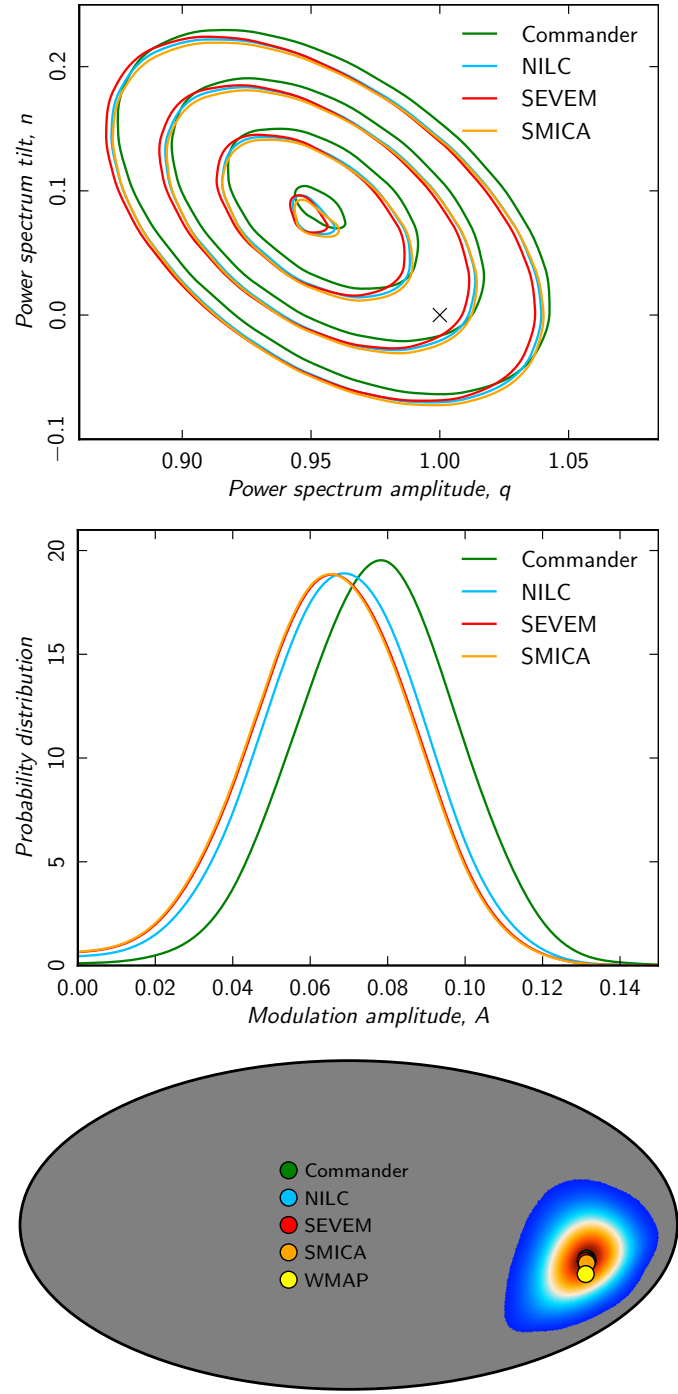


**Fig. 30.** Consistency between component separation algorithms as measured by the dipole modulation likelihood. The top panel shows the marginal power spectrum amplitude for the  $5^\circ$  smoothing scale, the middle panel shows dipole modulation amplitude, and the bottom panel shows the preferred dipole directions. The coloured area indicates the 95% confidence region for the Commander solution, while the dots shows the maximum-posterior directions for the other codes.

sion is reached using the low- $\ell$  *Planck* likelihood, as described in Planck Collaboration XV (2013).

In Fig. 30 we compare the results from all four CMB solutions for the  $5^\circ$  FWHM smoothing scale. Clearly the results are consistent despite the use of different algorithms and different treatments of the Galactic plane, demonstrating robustness with

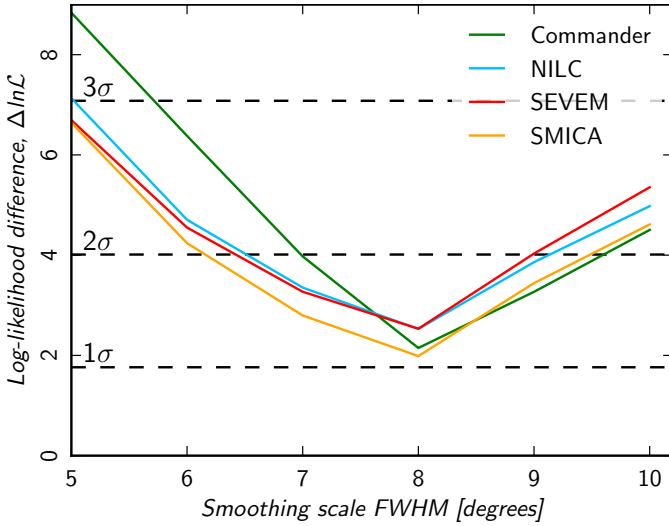


**Fig. 31.** Log-likelihood difference between the best-fit dipole modulation model and the fiducial isotropic model as a function of smoothing scale. Horizontal dashed lines indicate 1, 2 and  $3\sigma$  thresholds.

respect to the details of the analysis methods. Further, we also note that these results are consistent with those derived from the 5-year *WMAP* ILC map by Eriksen et al. (2007a), demonstrating robustness across experiments. On the other hand, it is notable that a higher dipole amplitude was found at  $9^\circ$  FWHM for the 3-year *WMAP* ILC map than is observed here, using a larger mask.

In Fig. 31 we show the log-likelihood difference between the derived maximum-likelihood point and the isotropic model,  $A = 0$ , as a function of smoothing scale. The power spectrum parameters are kept fixed at the best-fit values for both points, leaving three additional parameters for the dipole model. The dashed horizontal lines indicate the 1, 2 and  $3\sigma$  confidence regions for three degrees of freedom. As has been noted previously in the literature, these significances vary with smoothing scale. Taken at face value, the results presented here are suggestive but clearly not decisive, resulting in an unchanged situation with respect to earlier reports. This is of course not unexpected given that *WMAP* is already strongly cosmic variance limited at these angular scales.

The critical question is whether the trend seen at smaller angular scales in Fig. 31 continues, or if the apparent likelihood peak at  $5^\circ$  FWHM happens to be a local maximum. Hanson & Lewis (2009), and later Bennett et al. (2011), address this question through a computationally cheaper quadratic estimator, allowing them to extend a similar analysis to small scales. In doing so, they claim that the apparent likelihood peak at  $5^\circ$  is indeed a local maximum, and the evidence for the modulation model falls off when more data are included. In this respect, it should be noted that the dipole modulation model was originally proposed by Gordon et al. (2005) as a simple phenomenological characterization of the more general power asymmetry. In particular, it assumes that the modulation amplitude,  $A$ , is equally strong on all scales. From both the results shown in Sect. 5.5.1 and presented by Hanson & Lewis (2009); Bennett et al. (2011), this appears not to hold, as the fractional hemispherical power difference is clearly smaller at  $\ell > 300$  than at  $\ell < 100$ . On the other hand, the preferred directions derived from the current low- $\ell$  analysis is remarkably consistent with the high- $\ell$  direction derived in Sect. 5.5.1. A proper modulation model may therefore need additional spatial structure beyond the simple dipole pro-

posed by Gordon et al. (2005), as already suggested by Hoftuft et al. (2009) and Moss et al. (2011).

### 5.6. Generalized modulation

In this section, we study a generalization of the dipolar modulation field analysed in section 5.5.2 using the Bipolar Spherical Harmonic (BipoSH) formalism. For a statistically isotropic sky, the spherical harmonic space two-point correlation matrix is diagonal, and, given by the angular power spectrum  $C_\ell$ . The BipoSH representation provides a natural, mathematically complete, generalization of the angular power spectrum that captures statistical isotropy violations via coefficients that are a completely equivalent representation of the spherical harmonic correlation matrix,

$$A_{\ell_1 \ell_2}^{LM} = \sum_{m_1 m_2} \langle a_{\ell_1 m_1} a_{\ell_2 m_2} \rangle C_{\ell_1 m_1 \ell_2 m_2}^{LM}. \quad (40)$$

This relationship combines the off-diagonal spherical harmonic correlations into a bipolar multipole  $L$ ,  $M$  – analogous to the total angular momentum addition of states. The CMB angular power spectrum corresponds to the  $L = 0$  BipoSH coefficients  $C_\ell = (-1)^\ell A_{\ell \ell}^{00} \delta_{\ell \ell'} / \sqrt{2\ell + 1}$ .

A simple model that results in the violation of statistical isotropy arises from the modulation of the of the CMB sky,

$$T(\mathbf{n}) = T_0(\mathbf{n}) (1 + M(\mathbf{n})), \quad (41)$$

where  $T(\mathbf{n})$  represents the modulated CMB sky,  $T_0(\mathbf{n})$  is the underlying statistically isotropic random CMB sky and  $M(\mathbf{n})$  is a fixed, zero-mean, dimensionless, modulation field. The modulation signal, if any, is expected to be weak and allows quadratic terms in  $M$  to be neglected. The BipoSH coefficients for the modulated CMB field ( $L > 0$ ) are then given by the following expression,

$$A_{\ell_1 \ell_2}^{LM} = \bar{A}_{\ell_1 \ell_2}^{LM} + m_{LM} G_{\ell_1 \ell_2}^L, \quad (42)$$

$$G_{\ell_1 \ell_2}^L = \frac{C_{\ell_1} + C_{\ell_2}}{\sqrt{4\pi}} \frac{\Pi_{\ell_1} \Pi_{\ell_2}}{\Pi_L} C_{\ell_1 0 \ell_2 0}^{L0},$$

where  $\bar{A}_{\ell_1 \ell_2}^{LM}$  corresponds to the BipoSH coefficients of the unknown, but statistically isotropic, unmodulated CMB field,  $m_{LM}$  are the spherical harmonic coefficients of the modulating field ( $L > 0$ ),  $C_\ell$  is the best-fit CMB angular power spectrum and  $\Pi_\ell = \sqrt{2\ell + 1}$ . The statistically isotropic nature of the unmodulated CMB sky implies that the expectation values of  $\bar{A}_{\ell_1 \ell_2}^{LM}$  vanish for ( $L > 0$ ), leading to the estimator for the modulation field harmonics,

$$\hat{m}_{LM} = \sum_{\ell_1 \ell_2} w_{\ell_1 \ell_2}^L \frac{\hat{A}_{\ell_1 \ell_2}^{LM}}{G_{\ell_1 \ell_2}^L}. \quad (43)$$

denoted by the overhat (Hanson & Lewis 2009). The weights  $w_{\ell_1 \ell_2}^L$  for a minimum variance estimate for the modulation field correspond to

$$w_{\ell_1 \ell_2}^L = N \left( \frac{G_{\ell_1 \ell_2}^L}{\sigma_{A_{\ell_1 \ell_2}^{LM}}} \right)^2, \quad (44)$$

where  $N$  is a normalisation chosen such that  $\sum_{\ell_1 \ell_2} w_{\ell_1 \ell_2}^L = 1$ . The BipoSH representation further allows an estimate of the modulation field over specific angular scales by windowing regions in multipole space in the sum over multipoles  $\ell_1, \ell_2$  in eqn. 43.

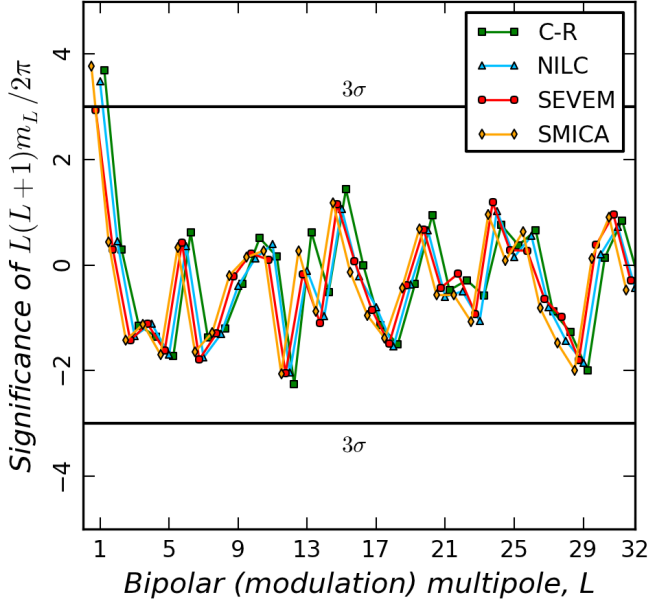


**Fig. 32.** The significance of the modulation power,  $L(L+1)m_L/2\pi$ , at bipolar multipoles  $L$ . The modulation spectra obtained from the four component separation maps (C-R, NILC, SEVEM and SMICA) are consistent with each other. Dipole ( $L=1$ ) modulation power is detected in all the spectra at a significance ranging from  $3.7$  to  $2.9\sigma$ . The solid black lines denote the  $3\sigma$  significance thresholds. There is no significant power detected at higher multipole of the modulation field  $1 < L \leq 32$ .

**Table 24.** This table lists the amplitude and direction of the dipole modulation in Galactic coordinates. The measured values of the dipole amplitude and direction are consistent for all maps. The corresponding dipole power for the SMICA map is seen at a detection significance of  $3.7\sigma$  as shown in Fig. 32.

Map	Dipole Amplitude A	$(l, b)$ [ $^\circ$ ] ( $\sigma_l = 15.4, \sigma_b = 15.1$ )
C-R . . . . .	$0.072^{+0.01}_{-0.01}$	(218.9, -21.4)
NILC . . . . .	$0.070^{+0.01}_{-0.01}$	(220.3, -20.2)
SEVEM . . . . .	$0.065^{+0.011}_{-0.011}$	(221.7, -21.4)
SMICA . . . . .	$0.073^{+0.01}_{-0.01}$	(217.5, -20.2)

This additional information could be very useful in identifying the origin of the statistical isotropy violation, which could be either cosmological or due to systematic artefacts (see Hajian & Souradeep 2003; Hajian & Souradeep 2006).

First, we limit our analysis to the four low resolution  $N_{\text{side}} = 32$  CMB maps used in Sect. 5.5.2 and reconstruct the modulation maps for each of them at the same low resolution. The U73 mask is applied to the reconstructed modulation maps before computing  $m_{LM}$ . The pseudo-power  $m_L$  is corrected for the mask applied to the modulation maps. Specifically for the case of dipole modulation, the pseudo-power  $m_L$  is related to the dipole amplitude by  $A = 1.5 \sqrt{m_1/\pi}$ .

A dipole modulation ( $L=1$ ) signal is detected at  $3\sigma$  significance in all the maps, as shown in Fig. 32. The amplitude and direction of the dipole modulation match those obtained via a likelihood analysis in Sect. 5.5.2. The BipoSH representation

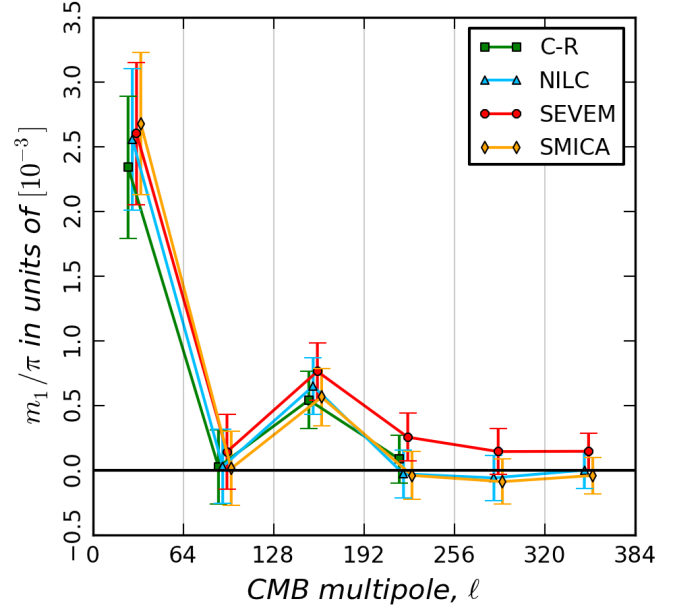


**Fig. 33.** The CMB multipole dependence of the BipoSH (modulation) power  $L(L+1)m_L/2\pi$  can be dissected into bins in  $\ell$ -space. This figure plots the measured dipole modulation ( $L=1$ ) power in CMB multipole bins. We establish that significant power in the dipole modulation is limited to  $\ell \in (2, 64)$  and does not extend to the higher CMB multipoles,  $\ell$ , considered. The vertical grid lines denote the CMB multipole  $\ell$ -bins.

of modulation confirms the dipole modulation signal found in the low-resolution map. Since this approach allows the reconstruction of any general small amplitude modulation field, the BipoSH representation places constraints on the power in the modulation field at all higher (bipolar) multipoles allowed by the resolution of the CMB maps.

We then extend the analysis to higher resolution using maps at  $N_{\text{side}} = 256$  for Commander and  $N_{\text{side}} = 2048$  for NILC, SEVEM and SMICA in order to study the above effect in more detail. We repeat the analysis on these higher resolution maps using the U73 mask. Contrary to our expectations based on a scale-independent (i.e., no  $\ell$ -dependence) model, the significance of the dipole does not increase in the high resolution maps. We then subdivide the  $\ell$ -range up to  $\ell_{\text{max}} = 384$  into uniform bins of size  $\Delta\ell = 64$ . As seen in Fig. 33, we recover the dipole modulation at over  $\sim 3\sigma$  significance only for the lowest bin  $\ell \in (2, 64)$ . This is consistent with the results in Sect. 5.5.2 and the BipoSH analysis on the corresponding low resolution maps shown in Fig. 32. However, the amplitude of the dipole is consistent with zero within  $3\sigma$  for all of the higher  $\ell$ -bins considered. This suggests that the simple modulation model in Eqn. 41 is inadequate and should minimally allow for the amplitude,  $A(\ell)$ , of the dipole to depend on CMB multipole,  $\ell$ . Although this may appear to be a more complex model, it does not necessarily lack motivation. It is readily conceivable that physical mechanisms that cause a dipolar modulation of the random CMB sky would be scale dependent and possibly significant only at low wavenumbers. More importantly, such a dipole modulation has also been noted in low resolution *WMAP* data (Eriksen et al. 2007a; Hoftuft et al. 2009). More recently, Bennett et al. (2011) also comment (without being quantitative) that the effect is present in the *WMAP* maps

but limited to low  $\ell$  and conclude that the  $\ell$  dependence rules out a simple modulation explanation. The fact that two independent experiments find this intriguing statistical isotropy violation points to a non-instrumental origin.

It is, of course, possible to extract the BipoSH coefficients  $A_{\ell_1 \ell_2}^{LM}$ , up to the maximum multipole  $\ell_{\max}$  allowed by the full resolution *Planck* maps at modest computational expense. This allows us to address a specific indication of statistical isotropy violation previously reported in the literature. Bennett et al. (2011) found nonzero BipoSH power spectra,  $A_{\ell\ell}^{20}$  and  $A_{\ell\ell+2}^{20}$  at very high statistical significance in the *WMAP* maps as determined in ecliptic coordinates, corresponding to a quadrupolar power asymmetry in the CMB sky. The BipoSH spectra peaked at  $\ell \sim 250$ , and the differences in the BipoSH signal determined from two different frequency bands indicated a non-cosmological origin. Furthermore, the azimuthal symmetry of this BipoSH signal in ecliptic coordinates suggested that it had its origin in some unaccounted-for systematic effect. The findings of Hanson et al. (2010); Joshi et al. (2012) strongly suggest that the signal arises due to an incomplete treatment of beam asymmetries in the data. Bennett et al. (2012) have subsequently noted that analysis of the *WMAP*9 beam-deconvolved maps no longer detects the signal.

We have computed the  $A_{\ell\ell}^{20}$  and  $A_{\ell\ell+2}^{20}$  in Ecliptic coordinates for the full resolution *Planck* CMB maps as shown in Fig. 34. The analysis yields no evidence for BipoSH coefficients that deviate significantly from zero. This provides conclusive observational evidence from independent CMB measurements that the *WMAP* result could have only arisen due to instrumental artefacts in that data set.

## 5.7. Parity asymmetry

### 5.7.1. Point-parity asymmetry

The CMB sky map may be considered as the sum of even and odd parity functions. Previously, an odd point-parity preference (hereafter parity asymmetry) was observed in the *WMAP* 3-, 5- and 7-year data releases (Land & Magueijo 2005b; Kim & Naselsky 2010a; Naselsky et al. 2012; Kim & Naselsky 2010b; Gruppuso et al. 2011). In this section we investigate the parity asymmetry for the *Planck* temperature anisotropy power spectra derived with a quadratic maximum likelihood (QML) estimator applied to the Commander-Ruler, NILC, SEVEM, and SMICA maps at  $N_{\text{side}} = 32$ , and with a pseudo- $C_\ell$  estimator at  $N_{\text{side}} = 64$ .

From the CMB anisotropy field defined on the sky,  $T(\mathbf{n})$ , we may construct symmetric and antisymmetric functions using the coordinate inversion  $\mathbf{n} \rightarrow -\mathbf{n}$ :

$$T^+(\mathbf{n}) = \frac{T(\mathbf{n}) + T(-\mathbf{n})}{2}, \quad T^-(\mathbf{n}) = \frac{T(\mathbf{n}) - T(-\mathbf{n})}{2}. \quad (45)$$

Therefore,  $T^+(\mathbf{n})$  and  $T^-(\mathbf{n})$  have even and odd parity, respectively. When combined with the parity property of spherical harmonics,  $Y_{\ell m}(\mathbf{n}) = (-1)^\ell Y_{\ell m}(-\mathbf{n})$ , we obtain:

$$\begin{aligned} T^+(\mathbf{n}) &= \sum_{\ell, m} a_{\ell m} Y_{\ell m}(\mathbf{n}) \Gamma^+(\ell), \\ T^-(\mathbf{n}) &= \sum_{\ell, m} a_{\ell m} Y_{\ell m}(\mathbf{n}) \Gamma^-(\ell), \end{aligned} \quad (46)$$

where  $n$  is an integer, and  $\Gamma^+(\ell) = \cos^2\left(\frac{\ell\pi}{2}\right)$ , and  $\Gamma^-(\ell) = \sin^2\left(\frac{\ell\pi}{2}\right)$ .

A significant power asymmetry between even and odd multipoles may thus be interpreted as a preference for a particular

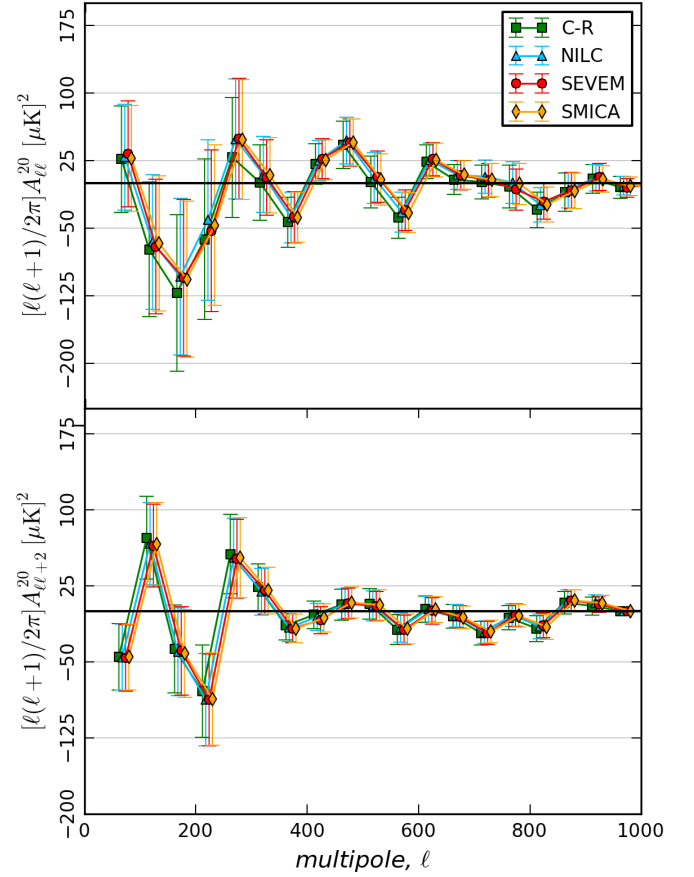


**Fig. 34.** The BipoSH power spectra  $A_{\ell\ell}^{20}$  and  $A_{\ell\ell+2}^{20}$  obtained from the four component separation maps (C-R, NILC, SEVEM & SMICA) are consistent with each other. Note that no significant ( $> 3\sigma$ ) detections are found. This independently establishes the fact that the quadrupolar BipoSH detections made by *WMAP* were due to *WMAP*-specific instrument systematics.

parity of the anisotropy pattern, connected to the parity asymmetry of the metric perturbations at scales above 1 – 4 Gpc (Kim & Naselsky 2010a). For investigation of the parity asymmetry we may consider the following quantities (Kim & Naselsky 2010a):

$$\begin{aligned} P^+(\ell) &= \sum_{n=2}^{\ell} \Gamma^+(n) \frac{n(n+1)}{2\pi} C_n, \\ P^-(\ell) &= \sum_{n=2}^{\ell} \Gamma^-(n) \frac{n(n+1)}{2\pi} C_n, \\ g(\ell) &= \frac{P^+(\ell)}{P^-(\ell)} \end{aligned} \quad (47)$$

where  $P^+$  and  $P^-$  are the sum of  $n(n+1)/2\pi C_n$  for even and odd multipoles respectively; the ratio  $P^+/P^-$  is associated with the degree of parity asymmetry, where a value of  $P^+/P^- < 1$  indicates odd-parity preference, and  $P^+/P^- > 1$  indicates even-parity preference.

Following (Kim & Naselsky 2010a), we will discuss the range of multipoles  $2 \leq \ell \leq 30$ , which belongs to the Sachs-Wolfe plateau of the TT power spectrum, where  $\ell(\ell+1)C_\ell \sim \text{const}$ . In order to make a rigorous assessment of the statistical significance of parity asymmetry at low  $\ell$ , we have compared



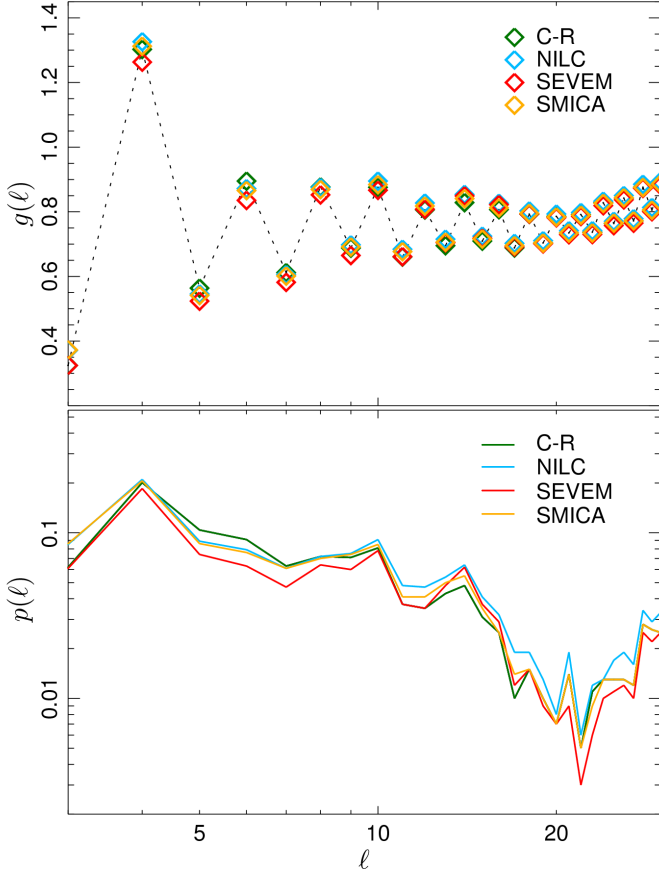


**Fig. 35.** Top panel: the parity estimator  $g(\ell)$  versus  $\ell$  for Commander-Ruler (black diamonds), NILC (red diamonds), SEVEM (blue diamonds) and SMICA (green diamonds). Bottom panel:  $p$ -value for C-R (black solid line), NILC (red line), SEVEM (blue line), and SMICA (green line).

$g(\ell)$  for the *Planck* power spectra with  $10^3$  simulated CMB maps based on the fiducial *Planck* cosmological model. We compute power spectra using a QML-estimator (Gruppiso et al. 2009) as applied to data at  $N_{\text{side}} = 32$  with the U73 mask applied. This yields practically identical power spectrum results for the same  $\ell$ -range determined with a pseudo- $C_\ell$  estimator applied to maps at  $N_{\text{side}} = 64$ .

In Fig.35 we show the  $g(\ell)$ -parameter for the *Planck* power spectra and the corresponding  $p$ -values. The  $p$ -value denotes the fraction of simulations in which the obtained value of  $P^+/P^-$  is as low as that observed in the data. Note that the results from the different *Planck* CMB maps yield consistent shapes for the  $g(\ell)$  and  $p(\ell)$ -parameters. The parity asymmetry at  $\ell = 22$  is most anomalous, with a corresponding  $p$ -value in the range  $0.002 - 0.004$ . Finally, the statistical significance of the parity asymmetry (i.e., low  $p$ -value) increases when we increase  $\ell_{\text{max}}$  up to 22-25. Therefore, the odd parity preference cannot simply be attributed to the low quadrupole power. It is plausible the low quadrupole power is not an isolated anomaly, but that it shares an origin with the odd parity preference (see for details (Kim & Naselsky 2010a; Naselsky et al. 2012; Kim & Naselsky 2010b)).

### 5.7.2. Mirror Parity

In this section we investigate the properties of the *Planck* temperature low-resolution maps under reflection with respect to a plane. This search for hidden mirror symmetries and anti-symmetries complements the tests for parity asymmetry, presented in Sect. 5.7.1. Starobinsky (1993) showed how a hidden mirror symmetry might be connected to the non-compact  $T^1$  topology, or to a compact  $T^3$  topology in which one topological scale is much less than the others. The CMB pattern would then exhibit a mirror symmetry with respect to the plane defined by the two large dimensions. Mirror symmetry has been searched for in the *COBE*-DMR data in de Oliveira-Costa et al. (1996), resulting in a lower limit for the scale of the compact dimension as 4 Gpc (see also Gurzadyan et al. 2007; Ben-David et al. 2012 for other more recent analysis). Finelli et al. (2012) analysed hidden mirror symmetry and anti-symmetry properties of the *WMAP* 7-year ILC temperature map, finding a preferred direction that could be considered anomalous at the 93 % confidence level with anti-symmetry properties. This direction lies close to the one defining the hemispherical asymmetry.

Following Finelli et al. (2012), we consider the following estimators:

$$S^\pm(\mathbf{n}_i) = \frac{1}{N_{\text{pix}}} \sum_{j=1}^{N_{\text{pix}}} \left[ \frac{1}{2} \left( \frac{\delta T}{T}(\mathbf{n}_j) \pm \frac{\delta T}{T}(\mathbf{n}_k) \right) \right]^2, \quad (48)$$

where the sum is meant over the observed pixels,  $N_{\text{pix}}$ ,  $\delta T/T(\mathbf{n}_j)$  is the CMB temperature anisotropy measured at the pixel pointed by the unit vector  $\mathbf{n}_j$ , and  $\mathbf{n}_k$  is the opposite direction of  $\mathbf{n}_j$  with respect to the plane defined by  $\mathbf{n}_i$ , i.e.

$$\mathbf{n}_k = \mathbf{n}_j - 2(\mathbf{n}_i \cdot \mathbf{n}_j)\mathbf{n}_i. \quad (49)$$

We compute the quantities  $S^\pm$  for each of the 3072 directions defined by HEALPix resolution  $N_{\text{side}} = 16$  map, by allowing the  $j$  and  $k$  indices to run over the unmasked pixels of the low resolution foreground cleaned maps. We perform the same analysis on 1000 simulated skies and store the minimum and maximum value for each of these.

The minimum value for the  $S^+$  estimator is reached for the plane defined by Galactic coordinates  $(\theta, \phi) = (104^\circ, 262^\circ)$ , with a significance of 0.8% (Commander-Ruler), 0.5% (NILC), 9.6% (SEVEM), and 1.2% (SMICA). The top panel of Fig. 36 shows the minimum value of  $S^+$  for each of the four methods and compared to the MC simulations computed for Commander-Ruler, which is considered to be representative.

The minimum value for the  $S^-$  estimator is found for a direction close to that associated with the cosmological dipole. It is not statistically significant for any of the CMB maps (see bottom panel of Fig.(36)).

The anomalous anti-symmetry direction found in the *Planck* CMB data is close to that found for the dipolar modulation in Sect. 5.5 suggesting some connection between them. The directions which minimize  $S^+$  and  $S^-$  for *Planck* are the same as those found for the *WMAP* 7-year ILC map in Finelli et al. (2012).

### 5.8. The Cold Spot

The Cold Spot was identified in the *WMAP* first year data (Vielva et al. 2004) through the estimation of the kurtosis of the Spherical Mexican Hat Wavelet (SMHW, e.g., Martínez-González et al. 2002) coefficients, and confirmed (Cruz et al. 2005) by analysing the area of the SMHW coefficients

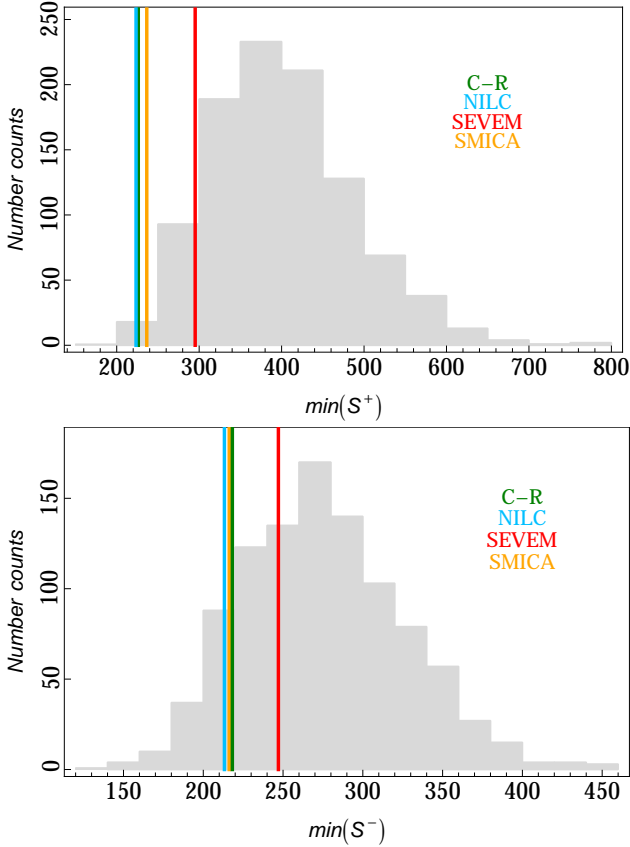


**Fig. 36.** Top panel: the  $S^+$  statistic. The vertical lines show the minimum value for the estimator as computed on low resolution C-R, NILC, SEVEM, and SMICA maps. The grey histogram shows the same quantity computed from 1000 simulated maps processed by C-R. Bottom panel: as above for  $S^-$ .

above/below a given threshold. Since its detection, the Cold Spot has been extensively studied and verified with a large battery of statistical probes (e.g., Mukherjee & Wang 2004; Cayón et al. 2005; McEwen et al. 2005; Cruz et al. 2007a; Räth et al. 2007b; Vielva et al. 2007; Pietrobon et al. 2008; Gurzadyan et al. 2009; Rossmanith et al. 2009b). A complete review of the Cold Spot can be found in Vielva (2010), including a discussion on possible explanations of its nature.

The analysis of the kurtosis of the SMHW coefficients has already been addressed in Sect. 4.5. We have checked that the kurtosis of the coefficients corresponding to the four *Planck* cleaned frequency maps is larger than the expected value obtained from simulations, with a modified upper tail probability of around 0.01. This is compatible with the value obtained from *WMAP*.

Nevertheless, the Cold Spot is more robustly described in terms of a morphological quantity: the area of the SMHW coefficients above/below a given threshold. At a given scale  $R$  and threshold  $\nu$ , the cold ( $A_R^{-\nu}$ ) and hot ( $A_R^{+\nu}$ ) areas of the SMHW coefficients are defined as:

$$\begin{aligned} A_R^{-\nu} &\equiv \#\{\omega_T(R, p) < -\nu\} \\ A_R^{+\nu} &\equiv \#\{\omega_T(R, p) < +\nu\} \end{aligned} \quad (50)$$

where  $\#$  represents the number operator, i.e., it indicates for how many pixels  $p$ , the specific condition defined between the braces is satisfied.

**Table 25.** Upper tail probability (UTP, in %) associated to the cold (left) and hot (right) areas. Results are given for a  $\nu > 4\sigma_R$  threshold and for the four *Planck* CMB maps. The three most significant scales associated to the Cold Spot are shown. Analysis performed on the exclusions masks associated with the U73 mask.

	Scale ( $R$ ) [']	C-R UTP (%)	NILC UTP (%)	SEVEM UTP (%)	SMICA UTP (%)
<i>cold area</i>	200	1.6	1.1	1.2	1.1
	250	0.3	0.3	0.3	0.3
	300	0.3	0.3	0.3	0.3
<i>hot area</i>	200	2.3	1.6	1.8	1.6
	250	2.7	2.2	2.4	2.2
	300	4.9	3.7	4.1	3.8

**Table 26.** Upper tail probability (in %) associated to the cold (left) and hot (right) areas. Results are given for a  $\nu > 4\sigma_R$  threshold and for the four *Planck* CMB maps. The three most significant scales associated to the Cold Spot are shown. Analysis performed on the exclusions masks associated with the G70 mask. N/A indicates that no area above that threshold was found on the data.

	Scale ( $R$ ) [']	C-R UTP (%)	NILC UTP (%)	SEVEM UTP (%)	SMICA UTP (%)
<i>cold area</i>	200	1.0	1.0	0.9	1.0
	250	0.3	0.3	0.3	0.3
	300	0.2	0.2	0.3	0.2
<i>hot area</i>	200	15.1	14.5	14.6	14.5
	250	N/A	N/A	N/A	N/A
	300	N/A	N/A	N/A	N/A

Table 25 summarises the results for the hot and cold areas determined for the four CMB maps analysed with the U73 mask (and its associated exclusions masks). The cold area is anomalous at scales between  $R = 200$  and  $R = 300'$ , similar to the sizes already highlighted with the kurtosis analysis. We see that the higher the threshold, the smaller the upper tail probability associated with the *Planck* CMB map. In particular, the cold area has a upper tail probability of 0.003 at  $\nu > 4\sigma_R$  and for  $R = 300'$ .

Notice that the most significant deviation comes from the cold area, although the hot area is marginally compatible. However, the cold area represents the most robust detection of an anomaly, since it is robust to the mask employed (see Tables 26 and 27).

The information provided in the previous Tables is also represented (for the  $R = 300'$  scale) in Fig. 37. In these nine panels we show the anomalous cold (in blue) and hot (in red) areas for thresholds  $\nu > 3.0\sigma_R$ ,  $\nu > 3.5\sigma_R$  and  $\nu > 4.0\sigma_R$  as determined from the SMICA map. For the two largest thresholds, the cold area corresponds to the Cold Spot, whereas the red area at  $3.0\sigma$  has already been identified in the *WMAP* data (e.g., Vielva et al. 2007) as an anomalous hot spot. From these analyses it is clear that the Cold Spot anomaly is present in both the *WMAP* and *Planck* data.

### 5.9. Interpretation of anomalies

The results presented here in Sect. 5 demonstrate that many features previously observed in the *WMAP* data are present also in

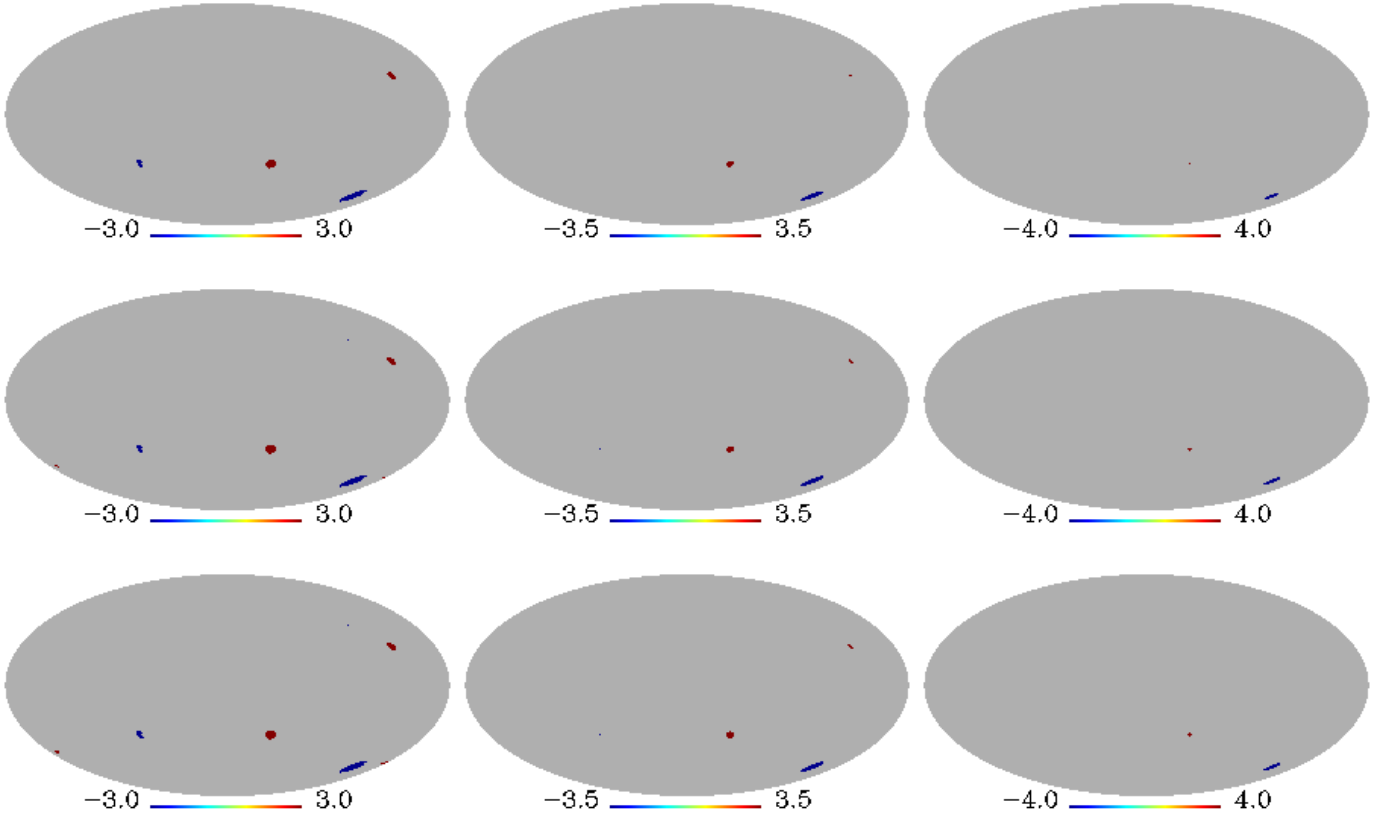


**Fig. 37.** SMHW coefficients at  $R = 300$  arc minutes, and thresholds of  $3.0\sigma$  (left),  $3.5\sigma$  (middle), and  $4.0\sigma$  (right). Results for the three masks considered in the analysis are shown: U73 mask (top), CG70 (middle) and CG60 (bottom).

**Table 27.** Upper tail probabilities (in %) associated with the cold (left) and hot (right) areas. Results are given for a  $\nu > 4\sigma_R$  threshold and for the four *Planck* CMB maps. The three most significant scales associated to the Cold Spot are shown. Analysis performed on the exclusions masks associated with the CG60 mask. N/A indicates that no area above that threshold was found on the data.

	Scale ( $R$ ) [']	C-R UTP (%)	NILC UTP (%)	SEVEM UTP (%)	SMICA UTP (%)
<i>cold area</i>	200	1.1	0.9	0.8	0.9
	250	0.1	0.1	0.1	0.1
	300	0.1	0.1	0.1	0.1
<i>hot area</i>	200	N/A	N/A	N/A	N/A
	250	N/A	N/A	N/A	N/A
	300	N/A	N/A	N/A	N/A

the *Planck* sky. This agreement between two independent experiments effectively rules out the possibility that their origin lies in systematic artefacts present in either data set. In particular, there is evidence for a violation of statistical isotropy at least on large angular scales in the context of the *Planck* fiducial sky model. Moreover, a dipolar power asymmetry may extend to scales corresponding to  $\ell \approx 1500$ , whilst fits to a model containing a dipole modulation field yield results in excess of  $3\sigma$  significance. In addition, there is evidence from such fits that the low- $\ell$  spectrum of the *Planck* data departs from the fiducial spectrum in both amplitude and slope. These results could have profound implica-

tions for cosmology. It is therefore pertinent to consider whether a model can be proposed to provide a common origin for the anomalies.

The microwave sky is manifestly non-Gaussian and anisotropic, with known contributions from Galactic astrophysical foregrounds, lensing of CMB anisotropies by the intervening matter distribution, and the ISW. However, the excellent performances of the component separation algorithms used here in rejecting diffuse foregrounds argues strongly against known Galactic emission as the source of the anomalies.

Schwarz et al. (2004), Copi et al. (2007), Maris et al. (2011) and Hansen et al. (2012) suggested that diffuse Solar System emission could contribute to the observed structure on large angular scales, although it is not expected that the classical Zodiacal Light Emission or Kuiper Belt objects are responsible. Planck Collaboration XIV (2013) presents the current *Planck* contribution to the modelling of the Zodiacal cloud.

Another possibility is that the anomalies have their origin in the local Universe. According to Francis & Peacock (2009), the removal of the ISW signal originating within the volume at  $z < 0.3$  from *WMAP* data reduces the significance of the apparent alignment between the CMB quadrupole and octopole and the Cold Spot. Efstathiou et al. (2010) have used the same correction to yield an increase in the structure of the two-point correlation function for angular separations less than  $60^\circ$ , that had been noted as apparently anomalous since the first *WMAP* data release. A future possibility is that *Planck* itself will be able to reconstruct the ISW signal and test its impact on issues related to

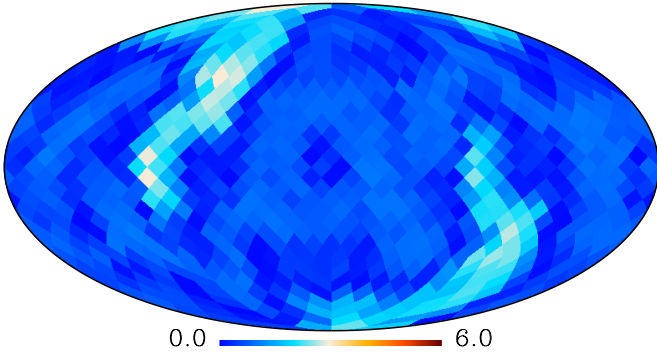


**Fig. 38.** Same as Fig. 24 but with the best fit Bianchi template subtracted from the SMICA map.

isotropy and non-Gaussianity. Planck Collaboration XIX (2013) presents maps of the effect based on the current data release.

Of more interest to us is that the anomalies are genuinely cosmological in origin. In that context, obvious candidate models include those with simply or multi-connected topology. In a companion paper (Planck Collaboration XXVI 2013), a subset of such models are considered and the signatures of their specific correlation structures on the sky are searched for. However, no detections are found, but rather the scale of topology is limited to be of order the diameter of the last-scattering surface or greater. More interestingly, they reconsider Bianchi VII<sub>h</sub> models that were previously demonstrated to show statistical correlation with the *WMAP* data (Jaffe et al. 2005, 2006; Bridges et al. 2007; McEwen et al. 2013), albeit with parameters inconsistent with standard cosmological parameters. In this new analysis, the Bianchi parameters are physically coupled to the cosmological ones, yielding no evidence for a Bianchi VII<sub>h</sub> cosmology. However, as before, when treated simply as a template for structure contained in the CMB sky, a best-fit pattern is found to be in good agreement with the old results. Previous analyses (Jaffe et al. 2005; Cayón et al. 2006; McEwen et al. 2006) have shown that when the CMB sky is corrected for such a template, many of the large-scale anomalies are no longer present at a statistically significant level. It is likely that such an effect will persist for Bianchi-corrected *Planck* data, and we have made an explicit test as to whether the best-fit Bianchi template can also explain the presence of phase correlations. We therefore repeated the surrogate analysis from Sect. 5.4 for the appropriately corrected SMICA map. Figure 38 presents the result for the corresponding significance map. It is clear that the signature for hemispherical asymmetry is drastically reduced, thereby rendering the signal formally statistically insignificant. Thus, the best-fit Bianchi model can also account for the asymmetries induced by higher order phase correlations. It should also be noted that subtracting the best-fit Bianchi template from the data, outside the U73 mask, explains the anomalous skewness and kurtosis values but not the variance, for which the corresponding lower tail probabilities are 0.008, 0.166, and 0.306, respectively. Given the lack of consistency of the physical parameters of the model with the *Planck* cosmological model, the results obtained using Bianchi-subtracted input maps might be considered moot, however, the morphology of the maps may provide insight into the type of underlying structures associated with the anomalies.

Although the Cold Spot is also rendered statistically insignificant by the Bianchi template, other possible explanations about its nature have been proposed, including the late evolution of

the large-scale structure (e.g., Inoue & Silk 2006, 2007), the Sunyaev-Zeldovich effect (e.g., Cruz et al. 2008), residual foregrounds (Cruz et al. 2006), gravitational lensing (Das & Spergel 2009), or a cosmic texture (e.g., Cruz et al. 2007b).

The presence of primordial magnetic fields (PMFs) due to either pre- or post-recombination mechanisms could also provide a physical basis for some of the anomalies discussed in this paper. Specifically, PMFs with coherence scales comparable to the present day horizon could result in Alfvén waves in the early Universe that generate specific signatures on the sky via the Doppler and integrated Sachs-Wolfe effects. In particular, a preferred angular direction in the CMB anisotropy can be induced (Durrer et al. 1998; Kim & Naselsky 2009) that leads to structure in the spherical harmonic mode correlation matrix (Kahniashvili et al. 2008). Appendix A presents a search for the predicted correlations between harmonic modes separated by  $\Delta\ell = 0, \pm 2$ , and  $\Delta m = 0, \pm 2$ , allowing constraints to be placed on the Alfvén wave amplitude. Further constraints on PMFs based on the power spectrum and bispectrum have been provided in Planck Collaboration XVI (2013) and Planck Collaboration XXIV (2013), respectively.

To conclude, when analysing a data set as complex and rich as that provided by *Planck*, some statistical outliers will be expected. However, it should be clear that the evidence for some of the large-angular scale anomalies is significant indeed, yet few physically compelling models have been proposed to account for them, and none so far that provide a common origin. The dipole modulation model that was analysed here was phenomenologically motivated, and is detected in the data at relatively high significance. Whether it can resolve the anomalous nature of other observed features remains to be evaluated.

## 6. Implications for $C_\ell$ and cosmological parameter estimation

The approach to  $C_\ell$  estimation, the construction of the *Planck* likelihood and subsequent inference of cosmological parameters are described in the accompanying papers Planck Collaboration XV (2013); Planck Collaboration XVI (2013). For these studies, specific assumptions are made about the isotropy and Gaussianity of the primordial fluctuations observed in the CMB. The latter in particular seems to be well-supported by the comprehensive set of tests applied to the *Planck* data in Sect. 4. The most significant discrepancies are seen in association with the Cold Spot (Sect. 5.8), which constitutes a localized region of sky of about  $10^\circ$  in size. Its impact on cosmological parameters is then likely to be relatively insignificant, and masking of the region could easily test this assertion.

It is well-known that the quadrupole and octopole have low-amplitudes relative to the best-fit cosmological power-spectrum. The contribution of those multipoles to cosmological parameter estimation is very small due to the associated cosmic variance on these scales, and thus the direct impact of their alignment (as discussed in Sect. 5.1) is also likely to be small. Remarkably, however, Planck Collaboration XV (2013) presents evidence that the low- $\ell$  multipole range from 2-30 is coherently low, and is not well accounted for by the standard  $\Lambda$ CDM model. Moreover, this conclusion is a consequence of the fact that the cosmological parameters are strongly influenced by the  $\ell = 1000$ –1500 range, previously inaccessible to *WMAP*. Consistent findings have been presented here in the form of the low-variance of the data in Sects. 4.1 and 5.2, although this is largely driven by the quadrupole and octopole alone.



The question therefore remains as to whether there is a deeper connection with the cosmological anomalies seen in both the *WMAP* and *Planck* data sets particularly on large angular scales. Indeed, the hemispherical asymmetry and dipolar power modulation discussed in Sects. 5.3 and 5.5 respectively could have a more important impact in that they directly address whether a broader class of cosmological models should be considered. Indeed, the low- $\ell$  signature seen in the data has previously been associated with missing power in a Universe with simply- or multiply-connected topology. However, there are specific morphological signatures of such topologies that have not been detected in the *Planck* data (Planck Collaboration XXVI 2013).

However, the phenomenologically motivated dipole modulation model due to Gordon et al. (2005) yields a significant fit to the data, as seen in Sects. 5.5.2 and 5.6. The former also shows some evidence for a departure from the *Planck* fiducial power spectrum in both amplitude and slope. Both of these analyses are in good agreement in terms of the direction of the dipolar modulation field with the model independent dipolar power modulation analysis of Sect. 5.5.1.

A qualitative exploration as to how these features are reflected in the low- $\ell$  power spectrum is provided in Fig. 39. Specifically, the plot presents the angular power spectra computed using a quadratic maximum-likelihood (QML) estimator (Paci et al. 2010, 2013) from the  $N_{\text{side}} = 16$  SMICA map after application of the U73 mask used in this paper. The *Planck* fiducial power spectrum is also shown for comparison. Clearly, there is a deficit of power as expected when no further partitioning of the sky is applied. However, further interesting properties of the data are revealed when spectra are computed for the two opposing hemispheres defined by the preferred direction in Sect. 5.5.1. In the positive direction, there is improved agreement between the derived spectrum and the *Planck* fiducial sky, but with an interesting oscillation between odd and even modes. For the negative direction, an overall suppression of power is again seen. It would be interesting to test the connection between these spectral features and the phase correlations detected in Sect. 5.4 or the evidence for parity violation presented in Sect. 5.7. The observations may, in part, reflect the presence of visually striking features noted by Bennett et al. (2011) — the four elongated cold fingers stretching from near the Galactic equator to the south Galactic pole and a prominent cold spot near the center of the map.

However, Fig. 28 and the corresponding analysis suggest that the asymmetry in power between hemispheres extends to much smaller angular scales. Whether such a property of the data would have implications for parameter estimation may yet need further exploration.

## 7. Conclusions

In this paper, we have tested the statistical isotropy and Gaussianity of the CMB using data from the *Planck* satellite. We have demonstrated that little evidence is seen for non-Gaussianity, although some deviations from isotropy are found.

Most of the tests performed in Sect. 4 showed an overall consistency with the null hypothesis, as represented by a set of realistic simulations based on a *Planck* fiducial sky model and including the secondary ISW-lensing effect (as detected for the first time with the *Planck* data, see Planck Collaboration XIX 2013). However, two important exceptions were seen. The variance of the CMB signal was found to be significantly lower than expected, with the anomalously low signal seemingly localized

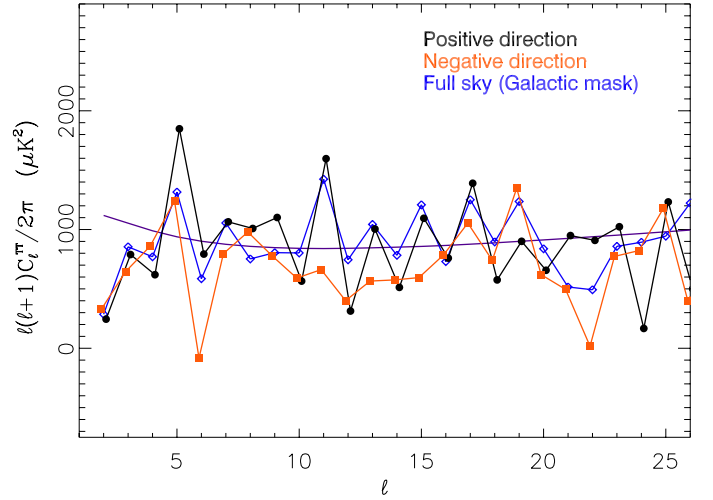


**Fig. 39.** Angular power spectrum at large angular scales computed on opposing hemispheres defined by the maximal asymmetry.

in the northern ecliptic hemisphere (Sect. 4.1). This result was also confirmed with the low variance of the wavelet coefficients that was seen on scales above a few degrees (see Sect. 4.5). Moreover, a significant deviation from Gaussianity was found in the form of a positive kurtosis of the wavelet coefficients.

These results correspond to statistical features on large angular scales where numerous anomalies were previously observed in the *WMAP* data. In Sect. 5, we revisited these in the light of the *Planck* data and found results in excellent agreement with those for *WMAP*. In particular, the most significant anomalies, namely the quadrupole-octopole alignment (Sect. 5.1), hemispherical asymmetry (Sect. 5.3), phase correlations (Sect. 5.4), dipolar power modulation (Sect. 5.5), generalized power modulation (Sect. 5.6), parity asymmetry (Sect. 5.7) and the Cold Spot (Sect. 5.8) have been confirmed with the *Planck* data. Attempts to explain the observed features in terms of systematic artefacts, local astrophysical sources of emission, or structure in the local Universe have not been successful. It is clear that these anomalies represent real features of the CMB sky.

However, it is difficult to make a detailed interpretation of the anomalies in the absence of theoretical models, in particular with regard to the role of a posteriori choices. Nevertheless, *Planck* does offer new possibilities to check the a posteriori claims in this context as a consequence of its superior multipole content that cannot easily be probed by *WMAP*. This is particularly relevant for the power asymmetry studies — Sect. 5.5.1 found that the same direction was preferred at  $\ell > 600$  as for  $\ell < 50$ , which should mitigate in part such criticisms.

Phenomenological models have been suggested to account for the observations. The dipolar power modulation approach due to Gordon et al. (2005) was explicitly tested in Sect. 5.5.2 and found to represent a good fit to the large scale asymmetry, corresponding to a detection at about  $3\sigma$  significance. This result was confirmed by the more generalized modulation study in Sect. 5.6, which also ruled out the presence of modulation fields of higher order. Alternatively, a Bianchi template fit to the data performed in Planck Collaboration XXVI (2013) can provide a good fit to the hemispherical asymmetry, the Cold Spot and the phase correlations, but corresponds to values of the cosmological parameters incompatible with those derived in

Planck Collaboration XVI (2013). Clearly, these do not provide complete and satisfactory explanations for the observations, and more physically motivated models should be sought.

This may also be indicated by the cosmological parameter studies presented in Planck Collaboration XV (2013); Planck Collaboration XVI (2013). Here, it was demonstrated that while the power-spectrum determined from the *Planck* temperature data is extremely consistent with a basic 6-parameter  $\Lambda$ CDM model, the low- $\ell$  multipoles ( $\ell \leq 30$ ) deviate from the best-fit model although at a significance that does not appear to exceed  $2.7\sigma$ . However, this is precisely the regime where many of the anomalies presented in this paper seem to manifest themselves, and where qualitatively interesting differences are observed in the power-spectra for two hemispheres defined by the preferred direction for the dipolar power modulation.

Finally, it is expected that the polarization data that will become available with the 2014 data release should provide valuable information on the nature of the CMB anomalies. Then, the presence, or even absence, of a specific signature in the data should help to elucidate the physical mechanism that is causing the anomaly (see Vielva et al. 2011, Frommert & Enßlin 2010 and Dvorkin et al. 2008 for examples related to the Cold Spot, mode alignment, and dipolar modulation, respectively). In particular, a deviation of isotropy present at recombination should be reflected in both the temperature and polarization data with a correlated signal. It may be that the statistical anomalies currently described in this paper are a hint of more profound physical phenomena that are yet to be revealed.

*Acknowledgements.* The development of Planck has been supported by: ESA; CNES and CNRS/INSU-IN2P3-INP (France); ASI, CNR, and INAF (Italy); NASA and DoE (USA); STFC and UKSA (UK); CSIC, MICINN, JA and RES (Spain); Tekes, AoF and CSC (Finland); DLR and MPG (Germany); CSA (Canada); DTU Space (Denmark); SER/SSO (Switzerland); RCN (Norway); SFI (Ireland); FCT/MCTES (Portugal); and PRACE (EU). A description of the Planck Collaboration and a list of its members, including the technical or scientific activities in which they have been involved, can be found at [http://www.sciops.esa.int/index.php?project=planck&page=Planck\\_Collaboration](http://www.sciops.esa.int/index.php?project=planck&page=Planck_Collaboration). We acknowledge the use of resources from the Norwegian national super computing facilities NOTUR. The modal and KSW bispectrum estimator analysis was performed on the COSMOS supercomputer, part of the STFC DiRAC HPC Facility. We further acknowledge the computer resources and technical assistance provided by the Spanish Supercomputing Network nodes at Universidad de Cantabria and Universidad Politécnica de Madrid as well as by the Advanced Computing and e-Science team at IFCA.

## References

- Ben-David, A., Kovetz, E. D., & Itzhaki, N. 2012, *Astrophys.J.*, 748, 39
- Bennett, C. L., Hill, R. S., Hinshaw, G., et al. 2011, *ApJS*, 192, 17
- Bennett, C. L., Larson, D., Weiland, J. L., et al. 2012, *ArXiv e-prints*
- Bielewicz, P., Eriksen, H. K., Banday, A. J., Górski, K. M., & Lilje, P. B. 2005, *ApJ*, 635, 750
- Bielewicz, P., Górski, K. M., & Banday, A. J. 2004, *MNRAS*, 355, 1283
- Bielewicz, P. & Riazuelo, A. 2009, *MNRAS*, 396, 609
- Bielewicz, P., Wandelt, B. D., & Banday, A. J. 2013, *MNRAS*, 429, 1376
- Bridges, M., McEwen, J. D., Lasenby, A. N., & Hobson, M. P. 2007, *MNRAS*, 377, 1473
- Cayón, L., Banday, A. J., Jaffe, T., et al. 2006, *MNRAS*, 369, 598
- Cayón, L., Jin, J., & Treaster, A. 2005, *MNRAS*, 362, 826
- Copi, C. J., Huterer, D., Schwarz, D. J., & Starkman, G. D. 2007, *Phys.Rev.D*, 75, 023507
- Copi, C. J., Huterer, D., & Starkman, G. D. 2004, *Phys. Rev. D*, 70, 043515
- Cruz, M., Cayón, L., Martínez-González, E., Vielva, P., & Jin, J. 2007a, *ApJ*, 655, 11
- Cruz, M., Martínez-González, E., Vielva, P., & Cayón, L. 2005, *MNRAS*, 356, 29
- Cruz, M., Martínez-González, E., Vielva, P., et al. 2008, *MNRAS*, 390, 913
- Cruz, M., Tucci, M., Martínez-González, E., & Vielva, P. 2006, *MNRAS*, 369, 57
- Cruz, M., Turok, N., Vielva, P., Martínez-González, E., & Hobson, M. 2007b, *Science*, 318, 1612
- Cruz, M., Vielva, P., Martínez-González, E., & Barreiro, R. B. 2011, *MNRAS*, 412, 2383
- Curto, A., Aumont, J., Macías-Pérez, J. F., et al. 2007, *A&A*, 474, 23
- Curto, A., Macías-Pérez, J. F., Martínez-González, E., et al. 2008, *A&A*, 486, 383
- Curto, A., Martínez-González, E., & Barreiro, R. B. 2009a, *ApJ*, 706, 399
- Curto, A., Martínez-González, E., & Barreiro, R. B. 2010, in *Highlights of Spanish Astrophysics V*, ed. J. M. Diego, L. J. Goicoechea, J. I. González-Serrano, & J. Gorgas, 277–+
- Curto, A., Martínez-González, E., & Barreiro, R. B. 2011a, *MNRAS*, 412, 1038
- Curto, A., Martínez-González, E., Barreiro, R. B., & Hobson, M. P. 2011b, *MNRAS*, 417, 488
- Curto, A., Martínez-González, E., Mukherjee, P., et al. 2009b, *MNRAS*, 393, 615
- Das, S. & Spergel, D. N. 2009, *Phys. Rev. D*, 79, 043007
- de Oliveira-Costa, A., Smoot, G. F., & Starobinsky, A. A. 1996, *Astrophys.J.*, 468, 457
- de Oliveira-Costa, A., Tegmark, M., Zaldarriaga, M., & Hamilton, A. 2004, *Phys.Rev.D*, 69, 063516
- De Troia, G., Ade, P. A. R., Bock, J. J., et al. 2007, *ApJ*, 670, L73
- Ducout, A., Bouchet, F. R., Colombi, S., Pogossyan, D., & Prunet, S. 2012, *MNRAS*, 423
- Durrer, R., Kahniashvili, T., & Yates, A. 1998, *Phys. Rev. D*, 58, 123004
- Dvorkin, C., Peiris, H. V., & Hu, W. 2008, *Phys. Rev. D*, 77, 063008
- Efstathiou, G. 2004, *MNRAS*, 348, 885
- Efstathiou, G., Ma, Y.-Z., & Hanson, D. 2010, *MNRAS*, 407, 2530
- Elsner, F. & Wandelt, B. D. 2013, *A&A*, 549, A111
- Eriksen, H. K., Banday, A. J., Górski, K. M., Hansen, F. K., & Lilje, P. B. 2007a, *ApJ*, 660, L81
- Eriksen, H. K., Banday, A. J., Górski, K. M., & Lilje, P. B. 2005, *ApJ*, 622, 58
- Eriksen, H. K., Hansen, F. K., Banday, A. J., Górski, K. M., & Lilje, P. B. 2004a, *ApJ*, 605, 14
- Eriksen, H. K., Huey, G., Saha, R., et al. 2007b, *ApJ*, 656, 641
- Eriksen, H. K., Lilje, P. B., Banday, A. J., & Górski, K. M. 2004b, *ApJS*, 151, 1
- Eriksen, H. K., Novikov, D. I., Lilje, P. B., Banday, A. J., & Górski, K. M. 2004c, *ApJ*, 612, 64
- Fergusson, J., Liguori, M., & Shellard, E. 2010a, *Phys.Rev.*, D82, 023502
- Fergusson, J., Liguori, M., & Shellard, E. 2010b
- Finelli, F., Gruppuso, A., Paci, F., & Starobinsky, A. 2012, *JCAP*, 1207, 049
- Fixsen, D. J. 2009, *ApJ*, 707, 916
- Francis, C. L. & Peacock, J. A. 2009, *MNRAS*, 406, 14
- Frommert, M. & Enßlin, T. A. 2010, *MNRAS*, 403, 1739
- Gordon, C., Hu, W., Huterer, D., & Crawford, T. 2005, *Phys.Rev.D*, 72, 103002
- Górski, K. M., Hivon, E., Banday, A. J., et al. 2005, *ApJ*, 622, 759
- Gott, J. R. I., Park, C., Juskiewicz, R., et al. 1990, *ApJ*, 352, 1
- Gruppuso, A., de Rosa, A., Cabella, P., et al. 2009, *MNRAS*, 400, 463
- Gruppuso, A., Finelli, F., Natoli, P., et al. 2011, *MNRAS*, 411, 1445
- Gurzadyan, V., Starobinsky, A., Kashin, A., Khachatryan, H., & Yegorian, G. 2007, *Mod.Phys.Lett.*, A22, 2955
- Gurzadyan, V. G., Allahverdyan, A. E., Ghahramanyan, T., et al. 2009, *A&A*, 497, 343
- Hajian, A. & Souradeep, T. 2003, *ApJ*, 597, L5

- Hajian, A. & Souradeep, T. 2006, *Phys. Rev. D*, 74, 123521
- Hansen, F. K., Banday, A. J., & Górski, K. M. 2004, *MNRAS*, 354, 641
- Hansen, F. K., Banday, A. J., Górski, K. M., Eriksen, H. K., & Lilje, P. B. 2009, *ApJ*, 704, 1448
- Hansen, M., Kim, J., Frejse, A. M., et al. 2012, *J. Cosmology Astropart. Phys.*, 10, 59
- Hanson, D. & Lewis, A. 2009, *Phys. Rev. D*, 80:063004, 2009
- Hanson, D., Lewis, A., & Challinor, A. 2010, *Phys. Rev. D*, 81, 103003
- Hikage, C., Matsubara, T., Coles, P., et al. 2008, *MNRAS*, 389, 1439
- Hivon, E., Górski, K. M., Netterfield, C. B., et al. 2002, *ApJ*, 567, 2
- Hoftuft, J., Eriksen, H. K., Banday, A. J., et al. 2009, *Astrophys. J.*, 699:985-989, 2009
- Inoue, K. T. & Silk, J. 2006, *ApJ*, 648, 23
- Inoue, K. T. & Silk, J. 2007, *ApJ*, 664, 650
- Jaffe, T. R., Banday, A. J., Eriksen, H. K., Górski, K. M., & Hansen, F. K. 2005, *ApJ*, 629, L1
- Jaffe, T. R., Hervik, S., Banday, A. J., & Górski, K. M. 2006, *ApJ*, 644, 701
- Joshi, N., Das, S., Rotti, A., Mitra, S., & Souradeep, T. 2012, *ArXiv e-prints*
- Kahnashvili, T., Lavrelashvili, G., & Ratna, B. 2008, *Phys. Rev. D*, 78, 063012
- Kim, J. & Naselsky, P. 2009, *J. Cosmology Astropart. Phys.*, 7, 41
- Kim, J. & Naselsky, P. 2010a, *ApJ*, 714, L265
- Kim, J. & Naselsky, P. 2010b, *Phys. Rev. D*, 82, 063002
- Komatsu, E., Dunkley, J., Nolte, M. R., et al. 2009, *ApJS*, 180, 330
- Komatsu, E., Kogut, A., Nolte, M. R., et al. 2003, *ApJS*, 148, 119
- Kronberg, P. P. 2009, in *IAU Symposium*, Vol. 259, *IAU Symposium*, 499–508
- Land, K. & Magueijo, J. 2005a, *Physical Review Letters*, 95, 071301
- Land, K. & Magueijo, J. 2005b, *Phys. Rev. D*, 72, 101302
- Lewis, A. & Bridle, S. 2002, *Phys. Rev. D*, 66, 103511
- Maris, M., Burigana, C., Gruppuso, A., Finelli, F., & Diego, J. M. 2011, *MNRAS*, 415, 2546
- Martínez-González, E., Gallegos, J. E., Argüeso, F., Cayón, L., & Sanz, J. L. 2002, *MNRAS*, 336, 22
- Matsubara, T. 2010, *Phys. Rev. D*, 81, 083505
- McEwen, J. D., Hobson, M. P., Lasenby, A. N., & Mortlock, D. J. 2005, *MNRAS*, 359, 1583
- McEwen, J. D., Hobson, M. P., Lasenby, A. N., & Mortlock, D. J. 2006, *MNRAS*, 369, 1858
- McEwen, J. D., Jossset, T., Feeney, S. M., Peiris, H. V., & Lasenby, A. N. 2013, *ArXiv e-prints*
- Mecke, K. R., Buchert, T., & Wagner, H. 1994, *A&A*, 288, 697
- Minkowski, H. 1903, *Mathematische Ann.*, 57, 447
- Mitra, S., Rocha, G., Górski, K. M., et al. 2011, *ApJS*, 193, 5
- Modest, H. I., Räth, C., Banday, A. J., et al. 2013, *MNRAS*, 428, 551
- Monteserín, C., Barreiro, R. B., Vielva, P., et al. 2008, *MNRAS*, 387, 209
- Moss, A., Scott, D., Zibin, J. P., & Battye, R. 2011, *Phys. Rev. D*, 84, 023014
- Mukherjee, P. & Wang, Y. 2004, *ApJ*, 613, 51
- Naselsky, P., Zhao, W., Kim, J., & Chen, S. 2012, *ApJ*, 749, 31
- Paci, F., Gruppuso, A., Finelli, F., et al. 2010, *MNRAS*, 407, 399
- Paci, F., Gruppuso, A., Finelli, F., et al. 2013, *ArXiv e-prints*
- Park, C.-G. 2004, *MNRAS*, 349, 313
- Pietrobon, D., Amblard, A., Balbi, A., et al. 2008, *Phys. Rev. D*, 78, 103504
- Planck Collaboration ES. 2013, *The Explanatory Supplement to the Planck 2013 results (ESA)*
- Planck Collaboration I. 2013, Submitted to *A&A*
- Planck Collaboration II. 2013, Submitted to *A&A*
- Planck Collaboration P09A. 2013, *A&A*
- Planck Collaboration VI. 2013, Submitted to *A&A*
- Planck Collaboration XII. 2013, Submitted to *A&A*
- Planck Collaboration XIV. 2013, Submitted to *A&A*
- Planck Collaboration XIX. 2013, Submitted to *A&A*
- Planck Collaboration XV. 2013, Submitted to *A&A*
- Planck Collaboration XVI. 2013, Submitted to *A&A*
- Planck Collaboration XVII. 2013, Submitted to *A&A*
- Planck Collaboration XXIV. 2013, Submitted to *A&A*
- Planck Collaboration XXV. 2013, Submitted to *A&A*
- Planck Collaboration XXVI. 2013, Submitted to *A&A*
- Planck Collaboration XXVII. 2013, Submitted to *A&A*
- Räth, C., Banday, A. J., Rossmanith, G., et al. 2011, *MNRAS*, 415, 2205
- Räth, C., Morfill, G. E., Rossmanith, G., Banday, A. J., & Górski, K. M. 2009, *Physical Review Letters*, 102, 131301
- Räth, C., Schuecker, P., & Banday, A. J. 2007a, *MNRAS*, 380, 466
- Räth, C., Schuecker, P., & Banday, A. J. 2007b, *MNRAS*, 380, 466
- Rossmanith, G., Modest, H., Räth, C., et al. 2012, *Phys. Rev. D*, 86, 083005
- Rossmanith, G., Räth, C., Banday, A. J., & Morfill, G. 2009a, *MNRAS*, 399, 1921
- Rossmanith, G., Räth, C., Banday, A. J., & Morfill, G. 2009b, *MNRAS*, 399, 1921
- Schmalzing, J. & Gorski, K. M. 1998, *MNRAS*, 297, 355
- Schwarz, D. J., Starkman, G. D., Huterer, D., & Copi, C. J. 2004, *Physical Review Letters*, 93, 221301
- Spergel, D. N., Bean, R., Doré, O., et al. 2007, *ApJS*, 170, 377
- Spergel, D. N., Verde, L., Peiris, H. V., et al. 2003, *ApJS*, 148, 175
- Starobinsky, A. A. 1993, *JETP Lett.*, 57, 622
- Tegmark, M., de Oliveira-Costa, A., & Hamilton, A. 2003, *Phys. Rev. D*, 68, 123523
- Vanmarcke, E. 1983, in *Random Fields*, by Erik Vanmarcke, pp. 372. ISBN 0-262-72045-0. Cambridge, Massachusetts, USA: The MIT Press, March 1983. (Paper), ed. Vanmarcke, E.
- Vielva, P. 2010, *Advances in Astronomy*, 2010
- Vielva, P., Martínez-González, E., Barreiro, R. B., Sanz, J. L., & Cayón, L. 2004, *ApJ*, 609, 22
- Vielva, P., Martínez-González, E., Cruz, M., Barreiro, R. B., & Tucci, M. 2011, *MNRAS*, 410, 33
- Vielva, P., Wiaux, Y., Martínez-González, E., & Vanderghenst, P. 2007, *MNRAS*, 381, 932
- Wiaux, Y., Vielva, P., Barreiro, R. B., Martínez-González, E., & Vanderghenst, P. 2008, *MNRAS*, 385, 939

## Appendix A: Constraints on Alfvén waves

Observations of synchrotron emission and Faraday rotation provide increasing evidence that large-scale astrophysical systems in the Universe are pervaded by magnetic fields. These huge systems include Ly- $\alpha$  forests and intercluster regions (see Kronberg 2009, for a review). Both pre- and post-recombination mechanisms could result in a background of nano-gauss fields that might be detectable in large-scale structures or the CMB, although at present no imprints of these Primordial Magnetic Fields (PMFs) have been detected therein.

Here, we report our findings based on an analysis of the *Planck* data to search for the predicted signature of statistical anisotropy due to PMFs. Specifically, PMFs with coherence scales comparable to the present day horizon may induce and sustain Alfvén waves in the early Universe that can leave observable imprints on the CMB via the Doppler and integrated Sachs-Wolfe effects. In particular, this results in a preferred angular direction in the CMB anisotropy, therefore breaking statistical isotropy (Durrer et al. 1998, Kim & Naselsky 2009).

Durrer et al. (1998) showed that cosmological Alfvén waves generate a fractional CMB anisotropy for a Fourier mode  $\mathbf{k}$ :

$$\frac{\delta T}{T_0}(\hat{\mathbf{n}}, \mathbf{k}) \approx \mathbf{n} \cdot \boldsymbol{\Omega}(\mathbf{k}, \eta_{\text{last}}) = \mathbf{n} \cdot \boldsymbol{\Omega}_0 v_A k \eta_{\text{last}} \mathbf{B} \cdot \mathbf{k} \quad (\text{A.1})$$

where  $\hat{\mathbf{n}}$  denotes sky direction,  $\mathbf{B}$  is a unit vector in the direction of the coherent PMF,  $\boldsymbol{\Omega}(\mathbf{k}, \eta_{\text{last}})$  is the Gauge invariant linear combination associated with vector perturbations,  $\eta_{\text{last}}$  denotes the conformal time at the moment of baryon-photon decoupling, and  $T_0$  is the CMB monopole temperature 2.7255 K (Fixsen 2009). Durrer et al. (1998) assumed that the vector perturbations are initially created by some random stochastic PMF and have the following statistical properties over an ensemble of universes:

$$\langle \Omega_0^i(\mathbf{k}) \Omega_0^j(\mathbf{k}) \rangle = (\delta_{ij} - \hat{k}_i \hat{k}_j) P(k). \quad (\text{A.2})$$

Here,  $P(k)$  is the power spectrum assumed to follow a simple power law:

$$P(k) = A_v \left( \frac{k}{k_0} \right)^{n_v}, \quad (\text{A.3})$$

where  $k_0$  is a pivot wavenumber set to 0.05/Mpc in this analysis. The Alfvén wave velocity is given by (Durrer et al. 1998):

$$v_A = \frac{B}{2 \sqrt{\pi(\rho_r + p_r)}} \approx 4 \times 10^{-4} \frac{B}{10^{-9} \text{Gauss}}, \quad (\text{A.4})$$

where  $\rho_r$  and  $p_r$  are the density and the pressure of photons, and the speed of light  $c$  is set to 1.

Kahniashvili et al. (2008) showed that the presence of Alfvén waves in the early Universe leads to specific correlations of the CMB in harmonic space:

$$\langle a_{\ell m}^* a_{\ell m} \rangle = C_\ell + \frac{\ell(\ell+1)}{(2\ell-1)(2\ell+3)} \{(\ell^2 + \ell - 3) \cos^2 \theta_B + \ell(\ell+1) - (3 \cos^2 \theta_B - 1)m^2 \left[ 1 - \frac{3}{\ell(\ell+1)} \right] \} I_d^{\ell, \ell},$$

$$\langle a_{\ell, m \pm 1}^* a_{\ell, m} \rangle = -\sin 2\theta_B \exp[\pm i\phi_B] \frac{\ell^2 + \ell - 3}{(2\ell-1)(2\ell+3)} \left( m \pm \frac{1}{2} \right) \times \sqrt{(\ell \mp m)(\ell \pm m + 1)} I_d^{\ell, \ell},$$

$$\langle a_{\ell, m \pm 2}^* a_{\ell, m} \rangle = -\frac{1}{2} \sin^2 \theta_B \exp[\pm i2\phi_B] \frac{\ell^2 + \ell - 3}{(2\ell-1)(2\ell+3)} \times \sqrt{(\ell \mp m)(\ell \mp m - 1)(\ell \pm m + 1)(\ell \pm m + 2)} I_d^{\ell, \ell},$$

$$\langle a_{\ell+2, m}^* a_{\ell, m} \rangle = -(3 \cos^2 \theta_B - 1) \frac{(\ell+3)\ell}{2(2\ell+3) \sqrt{(2\ell+1)(2\ell+5)}} \times \sqrt{((\ell+1)^2 - m^2)((\ell+2)^2 - m^2)} I_d^{\ell, \ell+2},$$

$$\langle a_{\ell-2, m}^* a_{\ell, m} \rangle = -(3 \cos^2 \theta_B - 1) \frac{(\ell+1)(\ell-2)}{2(2\ell-1) \sqrt{(2\ell-3)(2\ell+1)}} \times \sqrt{((\ell-1)^2 - m^2)(\ell^2 - m^2)} I_d^{\ell, \ell-2},$$

$$\langle a_{\ell+2, m \pm 1}^* a_{\ell, m} \rangle = \sin 2\theta_B \exp[\pm i\phi_B] \frac{(\ell+3)\ell}{2(2\ell+3) \sqrt{(2\ell+1)(2\ell+5)}} \times \sqrt{((\ell+1)^2 - m^2)(\ell \pm m + 2)(\ell \pm m + 3)} I_d^{\ell, \ell+2},$$

$$\langle a_{\ell-2, m \pm 1}^* a_{\ell, m} \rangle = -\sin 2\theta_B \exp[\pm i\phi_B] \frac{(\ell+1)(\ell-2)}{2(2\ell-1) \sqrt{(2\ell-3)(2\ell+1)}} \times \sqrt{(\ell^2 - m^2)(\ell \mp m - 1)(\ell \mp m - 2)} I_d^{\ell, \ell-2},$$

$$\langle a_{\ell+2, m \pm 2}^* a_{\ell, m} \rangle = -\frac{1}{2} \sin^2 \theta_B \exp[\pm i2\phi_B] \frac{(\ell+3)\ell}{2(2\ell+3) \sqrt{(2\ell+1)(2\ell+5)}} \times \sqrt{((\ell \pm m + 1)(\ell \pm m + 2)(\ell \pm m + 3)(\ell \pm m + 4))} I_d^{\ell, \ell+2},$$

$$\langle a_{\ell-2, m \pm 2}^* a_{\ell, m} \rangle = -\frac{1}{2} \sin^2 \theta_B \exp[\pm i2\phi_B] \frac{(\ell+1)(\ell-2)}{2(2\ell-1) \sqrt{(2\ell-3)(2\ell+1)}} \times \sqrt{((\ell \mp m - 3)(\ell \mp m - 2)(\ell \mp m - 1)(\ell \mp m))} I_d^{\ell, \ell-2},$$

where  $C_\ell$  is the power spectrum in the absence of Alfvén waves,  $\theta_B$  and  $\phi_B$  are the spherical angles of a PMF direction  $\mathbf{B}$ . Here,

$I_d^{\ell, \ell'}$  is given by:

$$\begin{aligned} I_d^{\ell, \ell'} &= \frac{2T_0^2}{\pi} \int d \ln k k^3 A_v \left( \frac{k}{k_0} \right)^{n_v} \\ &\times \exp \left( -2 \frac{k^2}{k_D^2} \right) v_A^2 \left( \frac{\eta_{\text{last}}}{\eta_0} \right)^2 j_\ell(k\eta_0) j_{\ell'}(k\eta_0) \\ &= \frac{2T_0^2}{\pi} \left( \frac{\eta_{\text{last}}}{\eta_0} \right)^2 A_v v_A^2 k_0^3 \\ &\times \int d \ln k \left( \frac{k}{k_0} \right)^{n_v+3} \exp \left( -2 \frac{k^2}{k_D^2} \right) j_\ell(k\eta_0) j_{\ell'}(k\eta_0), \end{aligned}$$

where  $\eta_0$  is the present conformal time, and  $k_D$  denotes the comoving wavenumber of the dissipation scale, due to photon viscosity and given by approximately  $10/\eta_{\text{last}}$  (Durrer et al. 1998). The damping effect becomes significant on multipoles  $\ell \gtrsim 500$  (Durrer et al. 1998). As shown above, Alfvén waves in the early Universe produce correlations between harmonic modes separated by  $\Delta\ell = 0, \pm 2$ , and  $\Delta m = 0, \pm 2$ . Investigating these imprints, we may impose a constraint on the Alfvén waves. In the weak Alfvén wave limit, the CMB data likelihood can be expanded as follows:

$$\mathcal{L} \approx \mathcal{L}|_{A_v v_A^2=0} + \left. \frac{\partial \mathcal{L}}{\partial (A_v v_A^2)} \right|_{A_v v_A^2=0} A_v v_A^2 + \frac{1}{2} \left. \frac{\partial^2 \mathcal{L}}{\partial (A_v v_A^2)^2} \right|_{A_v v_A^2=0} (A_v v_A^2)^2 + \mathcal{O}((A_v v_A^2)^3). \quad (\text{A.5})$$

Since all correlations produced by Alfvén waves are proportional to  $A_v v_A^2$ , the first term in Eq. A.5 is simply equal to the likelihood of the standard cosmological model. The first and second derivative of the likelihood are obtained by:

$$\frac{\partial \mathcal{L}}{\partial \lambda} = \mathcal{H} - \langle \mathcal{H} \rangle, \quad \frac{\partial^2 \mathcal{L}}{\partial \lambda^2} = -\langle \mathcal{H}^2 \rangle + \langle \mathcal{H} \rangle \langle \mathcal{H} \rangle, \quad (\text{A.6})$$

where

$$\mathcal{H} = \frac{1}{2} [\mathbf{C}^{-1} \mathbf{a}]^\dagger \frac{\partial \mathcal{C}}{\partial \lambda} [\mathbf{C}^{-1} \mathbf{a}], \quad (\text{A.7})$$

$\mathbf{a}$  is the data vector, consisting of the spherical harmonic coefficients,  $a_{\ell m}$ , of the CMB anisotropy data, and  $\mathbf{C}$  is their covariance matrix.

In our analysis, we consider the four foreground cleaned CMB maps *Commander-Ruler*, *NILC*, *SEVEM*, and *SMICA* and apply the common mask. We assume the fiducial *Planck* cosmological model, and use MC simulations to estimate the ensemble average values for signal and noise, as required in Eq. A.6. The quantity  $\mathbf{C}^{-1} \mathbf{a}$  from Eq. A.7 was then determined by the messenger field method (Elsner & Wandelt 2013). The *CosmoMC* package (Lewis & Bridle 2002) is then used as a generic sampler in order to obtain the posterior probability for the Alfvén wave parameters  $\{A_v v_A^2, n_v, \theta_B, \phi_B\}$ .

In Table A.1, we show the upper bounds on the Alfvén wave amplitude  $A_v v_A^2$  at various confidence levels, after marginalizing over the spectral index  $n_v$  and the direction  $\theta_B, \phi_B$ . From the analysis of the *Planck* data, we impose an upper bound on the Alfvén wave amplitude that is tighter than that from the *WMAP* data by more than one order of magnitude.

<sup>1</sup> APC, AstroParticule et Cosmologie, Université Paris Diderot, CNRS/IN2P3, CEA/Irfu, Observatoire de Paris, Sorbonne Paris Cité, 10, rue Alice Domon et Léonie Duquet, 75205 Paris Cedex

**Table A.1.** *Planck* constraints on the Alfvén wave amplitude  $A_v v_A^2$ .

Confidence Level	68%	95%	99.7%
C-R . . . . .	$< 0.48 \times 10^{-9}$	$< 1.01 \times 10^{-9}$	$< 1.57 \times 10^{-9}$
NILC . . . . .	$< 0.49 \times 10^{-9}$	$< 1.00 \times 10^{-9}$	$< 1.56 \times 10^{-9}$
SEVEM . . . . .	$< 0.54 \times 10^{-9}$	$< 1.13 \times 10^{-9}$	$< 1.73 \times 10^{-9}$
SMICA . . . . .	$< 0.47 \times 10^{-9}$	$< 0.87 \times 10^{-9}$	$< 1.29 \times 10^{-9}$

13, France

<sup>2</sup> Aalto University Metsähovi Radio Observatory, Metsähovintie 114, FIN-02540 Kylmäla, Finland

<sup>3</sup> African Institute for Mathematical Sciences, 6-8 Melrose Road, Muizenberg, Cape Town, South Africa

<sup>4</sup> Agenzia Spaziale Italiana Science Data Center, c/o ESRIN, via Galileo Galilei, Frascati, Italy

<sup>5</sup> Agenzia Spaziale Italiana, Viale Liegi 26, Roma, Italy

<sup>6</sup> Astrophysics Group, Cavendish Laboratory, University of Cambridge, J J Thomson Avenue, Cambridge CB3 0HE, U.K.

<sup>7</sup> Astrophysics & Cosmology Research Unit, School of Mathematics, Statistics & Computer Science, University of KwaZulu-Natal, Westville Campus, Private Bag X54001, Durban 4000, South Africa

<sup>8</sup> CITA, University of Toronto, 60 St. George St., Toronto, ON M5S 3H8, Canada

<sup>9</sup> CNRS, IRAP, 9 Av. colonel Roche, BP 44346, F-31028 Toulouse cedex 4, France

<sup>10</sup> California Institute of Technology, Pasadena, California, U.S.A.

<sup>11</sup> Centre for Theoretical Cosmology, DAMTP, University of Cambridge, Wilberforce Road, Cambridge CB3 0WA U.K.

<sup>12</sup> Centro de Estudios de Física del Cosmos de Aragón (CEFCA), Plaza San Juan, 1, planta 2, E-44001, Teruel, Spain

<sup>13</sup> Computational Cosmology Center, Lawrence Berkeley National Laboratory, Berkeley, California, U.S.A.

<sup>14</sup> Consejo Superior de Investigaciones Científicas (CSIC), Madrid, Spain

<sup>15</sup> DSM/Irfu/SPP, CEA-Saclay, F-91191 Gif-sur-Yvette Cedex, France

<sup>16</sup> DTU Space, National Space Institute, Technical University of Denmark, Elektrovej 327, DK-2800 Kgs. Lyngby, Denmark

<sup>17</sup> Département de Physique Théorique, Université de Genève, 24, Quai E. Ansermet, 1211 Genève 4, Switzerland

<sup>18</sup> Departamento de Física Fundamental, Facultad de Ciencias, Universidad de Salamanca, 37008 Salamanca, Spain

<sup>19</sup> Departamento de Física, Universidad de Oviedo, Avda. Calvo Sotelo s/n, Oviedo, Spain

<sup>20</sup> Departamento de Matemáticas, Estadística y Computación, Universidad de Cantabria, Avda. de los Castros s/n, Santander,

Spain

<sup>21</sup> Department of Astronomy and Astrophysics, University of Toronto, 50 Saint George Street, Toronto, Ontario, Canada

<sup>22</sup> Department of Astrophysics/IMAPP, Radboud University Nijmegen, P.O. Box 9010, 6500 GL Nijmegen, The Netherlands

<sup>23</sup> Department of Electrical Engineering and Computer Sciences, University of California, Berkeley, California, U.S.A.

<sup>24</sup> Department of Physics & Astronomy, University of British Columbia, 6224 Agricultural Road, Vancouver, British Columbia, Canada

<sup>25</sup> Department of Physics and Astronomy, Dana and David Dornsife College of Letter, Arts and Sciences, University of Southern



- California, Los Angeles, CA 90089, U.S.A.
- <sup>26</sup> Department of Physics and Astronomy, University College London, London WC1E 6BT, U.K.
- <sup>27</sup> Department of Physics, Gustaf H  llstr  min katu 2a, University of Helsinki, Helsinki, Finland
- <sup>28</sup> Department of Physics, Princeton University, Princeton, New Jersey, U.S.A.
- <sup>29</sup> Department of Physics, University of Alberta, 11322-89 Avenue, Edmonton, Alberta, T6G 2G7, Canada
- <sup>30</sup> Department of Physics, University of California, Berkeley, California, U.S.A.
- <sup>31</sup> Department of Physics, University of California, One Shields Avenue, Davis, California, U.S.A.
- <sup>32</sup> Department of Physics, University of California, Santa Barbara, California, U.S.A.
- <sup>33</sup> Department of Physics, University of Illinois at Urbana-Champaign, 1110 West Green Street, Urbana, Illinois, U.S.A.
- <sup>34</sup> Dipartimento di Fisica e Astronomia G. Galilei, Universit   degli Studi di Padova, via Marzolo 8, 35131 Padova, Italy
- <sup>35</sup> Dipartimento di Fisica e Scienze della Terra, Universit   di Ferrara, Via Saragat 1, 44122 Ferrara, Italy
- <sup>36</sup> Dipartimento di Fisica, Universit   La Sapienza, P. le A. Moro 2, Roma, Italy
- <sup>37</sup> Dipartimento di Fisica, Universit   degli Studi di Milano, Via Celoria, 16, Milano, Italy
- <sup>38</sup> Dipartimento di Fisica, Universit   degli Studi di Trieste, via A. Valerio 2, Trieste, Italy
- <sup>39</sup> Dipartimento di Fisica, Universit   di Roma Tor Vergata, Via della Ricerca Scientifica, 1, Roma, Italy
- <sup>40</sup> Dipartimento di Matematica, Universit   di Roma Tor Vergata, Via della Ricerca Scientifica, 1, Roma, Italy
- <sup>41</sup> Discovery Center, Niels Bohr Institute, Blegdamsvej 17, Copenhagen, Denmark
- <sup>42</sup> Dpto. Astrof  sica, Universidad de La Laguna (ULL), E-38206 La Laguna, Tenerife, Spain
- <sup>43</sup> European Space Agency, ESAC, Planck Science Office, Camino bajo del Castillo, s/n, Urbanizaci  n Villafranca del Castillo, Villanueva de la Ca  ada, Madrid, Spain
- <sup>44</sup> European Space Agency, ESTEC, Keplerlaan 1, 2201 AZ Noordwijk, The Netherlands
- <sup>45</sup> Helsinki Institute of Physics, Gustaf H  llstr  min katu 2, University of Helsinki, Helsinki, Finland
- <sup>46</sup> INAF - Osservatorio Astronomico di Padova, Vicolo dell'Osservatorio 5, Padova, Italy
- <sup>47</sup> INAF - Osservatorio Astronomico di Roma, via di Frascati 33, Monte Porzio Catone, Italy
- <sup>48</sup> INAF - Osservatorio Astronomico di Trieste, Via G.B. Tiepolo 11, Trieste, Italy
- <sup>49</sup> INAF/IASF Bologna, Via Gobetti 101, Bologna, Italy
- <sup>50</sup> INAF/IASF Milano, Via E. Bassini 15, Milano, Italy
- <sup>51</sup> INFN, Sezione di Bologna, Via Irnerio 46, I-40126, Bologna, Italy
- <sup>52</sup> INFN, Sezione di Roma 1, Universit   di Roma Sapienza, Piazzale Aldo Moro 2, 00185, Roma, Italy
- <sup>53</sup> IPAG: Institut de Plan  tologie et d'Astrophysique de Grenoble, Universit   Joseph Fourier, Grenoble 1 / CNRS-INSU, UMR 5274,

- Grenoble, F-38041, France
- cedex, France
- <sup>54</sup> ISDC Data Centre for Astrophysics, University of Geneva, ch. d'Ecogia 16, Versoix, Switzerland
- <sup>55</sup> IUCAA, Post Bag 4, Ganeshkhind, Pune University Campus, Pune 411 007, India
- <sup>56</sup> Imperial College London, Astrophysics group, Blackett Laboratory, Prince Consort Road, London, SW7 2AZ, U.K.
- <sup>57</sup> Infrared Processing and Analysis Center, California Institute of Technology, Pasadena, CA 91125, U.S.A.
- <sup>58</sup> Institut Néel, CNRS, Université Joseph Fourier Grenoble I, 25 rue des Martyrs, Grenoble, France
- <sup>59</sup> Institut Universitaire de France, 103, bd Saint-Michel, 75005, Paris, France
- <sup>60</sup> Institut d'Astrophysique Spatiale, CNRS (UMR8617) Université Paris-Sud 11, Bâtiment 121, Orsay, France
- <sup>61</sup> Institut d'Astrophysique de Paris, CNRS (UMR7095), 98 bis Boulevard Arago, F-75014, Paris, France
- <sup>62</sup> Institute for Space Sciences, Bucharest-Magurale, Romania
- <sup>63</sup> Institute of Astronomy and Astrophysics, Academia Sinica, Taipei, Taiwan
- <sup>64</sup> Institute of Astronomy, University of Cambridge, Madingley Road, Cambridge CB3 0HA, U.K.
- <sup>65</sup> Institute of Theoretical Astrophysics, University of Oslo, Blindern, Oslo, Norway
- <sup>66</sup> Instituto de Astrofísica de Canarias, C/Vía Láctea s/n, La Laguna, Tenerife, Spain
- <sup>67</sup> Instituto de Física de Cantabria (CSIC-Universidad de Cantabria), Avda. de los Castros s/n, Santander, Spain
- <sup>68</sup> Jet Propulsion Laboratory, California Institute of Technology, 4800 Oak Grove Drive, Pasadena, California, U.S.A.
- <sup>69</sup> Jodrell Bank Centre for Astrophysics, Alan Turing Building, School of Physics and Astronomy, The University of Manchester, Oxford Road, Manchester, M13 9PL, U.K.
- <sup>70</sup> Kavli Institute for Cosmology Cambridge, Madingley Road, Cambridge, CB3 0HA, U.K.
- <sup>71</sup> LAL, Université Paris-Sud, CNRS/IN2P3, Orsay, France
- <sup>72</sup> LERMA, CNRS, Observatoire de Paris, 61 Avenue de l'Observatoire, Paris, France
- <sup>73</sup> Laboratoire AIM, IRFU/Service d'Astrophysique - CEA/DSM - CNRS - Université Paris Diderot, Bât. 709, CEA-Saclay, F-91191 Gif-sur-Yvette Cedex, France
- <sup>74</sup> Laboratoire Traitement et Communication de l'Information, CNRS (UMR 5141) and Télécom ParisTech, 46 rue Barrault F-75634 Paris Cedex 13, France
- <sup>75</sup> Laboratoire de Physique Subatomique et de Cosmologie, Université Joseph Fourier Grenoble I, CNRS/IN2P3, Institut National Polytechnique de Grenoble, 53 rue des Martyrs, 38026 Grenoble
- <sup>76</sup> Laboratoire de Physique Théorique, Université Paris-Sud 11 & CNRS, Bâtiment 210, 91405 Orsay, France
- <sup>77</sup> Lawrence Berkeley National Laboratory, Berkeley, California, U.S.A.
- <sup>78</sup> Max-Planck-Institut für Astrophysik, Karl-Schwarzschild-Str. 1, 85741 Garching, Germany
- <sup>79</sup> Max-Planck-Institut für Extraterrestrische Physik, Giessenbachstraße, 85748 Garching, Germany
- <sup>80</sup> McGill Physics, Ernest Rutherford Physics Building, McGill University, 3600 rue University, Montréal, QC, H3A 2T8, Canada
- <sup>81</sup> MilliLab, VTT Technical Research Centre of Finland, Tietotie 3, Espoo, Finland
- <sup>82</sup> Niels Bohr Institute, Blegdamsvej 17, Copenhagen, Denmark
- <sup>83</sup> Observational Cosmology, Mail Stop 367-17, California Institute of Technology, Pasadena, CA, 91125, U.S.A.
- <sup>84</sup> Optical Science Laboratory, University College London, Gower Street, London, U.K.
- <sup>85</sup> SB-ITP-LPPC, EPFL, CH-1015, Lausanne, Switzerland
- <sup>86</sup> SISSA, Astrophysics Sector, via Bonomea 265, 34136, Trieste, Italy
- <sup>87</sup> School of Physics and Astronomy, Cardiff University, Queens Buildings, The Parade, Cardiff, CF24 3AA, U.K.
- <sup>88</sup> School of Physics and Astronomy, University of Nottingham, Nottingham NG7 2RD, U.K.
- <sup>89</sup> Space Sciences Laboratory, University of California, Berkeley, California, U.S.A.
- <sup>90</sup> Special Astrophysical Observatory, Russian Academy of Sciences, Nizhnij Arkhyz, Zelenchukskiy region, Karachai-Cherkessian Republic, 369167, Russia
- <sup>91</sup> Stanford University, Dept of Physics, Varian Physics Bldg, 382 Via Pueblo Mall, Stanford, California, U.S.A.
- <sup>92</sup> Sub-Department of Astrophysics, University of Oxford, Keble Road, Oxford OX1 3RH, U.K.
- <sup>93</sup> Theory Division, PH-TH, CERN, CH-1211, Geneva 23, Switzerland
- <sup>94</sup> UPMC Univ Paris 06, UMR7095, 98 bis Boulevard Arago, F-75014, Paris, France
- <sup>95</sup> Université de Toulouse, UPS-OMP, IRAP, F-31028 Toulouse cedex 4, France
- <sup>96</sup> University of Granada, Departamento de Física Teórica y del Cosmos, Facultad de Ciencias, Granada, Spain
- <sup>97</sup> University of Miami, Knight Physics Building, 1320 Campo Sano Dr., Coral Gables, Florida, U.S.A.
- <sup>98</sup> Warsaw University Observatory, Aleje Ujazdowskie 4, 00-478 Warszawa, Poland